Kent Academic Repository

Yolland, Lawrence (2014) *Extreme Shock Pressures: Recovery and Detection of Microfossils.* **Master of Science by Research (MScRes) thesis, University of Kent,.**

Downloaded from

The version of record is available from

This document version

DOI for this version

Licence for this version

Additional information

Versions of research works

Versions of Record

Author Accepted Manuscripts

Enquiries

Extreme Shock Pressures: Recovery and Detection of Microfossils.

-And-

A Novel Liquid Core Sabot Design.

by

Lawrence Yolland

Submitted for the degree of Master of Science

at the University of Kent

2014

CUI SERVIRE REGNARE EST

ABSTRACT.

In this thesis an experimental method is utilised to test the viability and suitability of algal microfossils in the context of simulating the shock phase of lithopanspermia. Previously, the lunar surface has been suggested as a potential receptacle and store for ejected terrestrial material following a large impact on Earth. This has led to the moon being labelled in the literature as Earth's attic.

A two stage light-gas gun is used in a series of low velocity and hypervelocity impacts. These shot range from 0.388 to 5.11 km s^{-1}. These impact velocities experimentally map to computer simulations of ejecta originating from Earth and impacting the lunar surface. Here microfossils are loaded into a sabot and frozen. They are then fired using the light-gas gun at pre-defined velocities at a water bag target. Following the impact the water is filtered and the filtrate analysed under a scanning electron microscope.

This thesis finds a shock pressure related size effect in terms of a number of size metrics. Peak shock pressure is calculated using the Planar Impact Approximation. With this, the maximum shock pressure induced by an impact was calculated to be 13.3 GPa. Microfossil fragments were recovered following each shot but intact examples became rarer as the shot velocity was ramped up.

This study also provides a solution to a methodological problem arising from evacuation of a light-gas gun, and the consequential evaporation of liquids within a sabot. Thus a projectile design that can contain liquid at low pressure is made available here.

ACKNOWLEDGEMENTS.

CONTENTS.

CHAPTER ONE:

INTRODUCTION.

This chapter is aimed at providing an introduction to the thesis. It will specifically focus on historical context and contemporary scientific developments that this work has relevance to.

1.1. Background

The early 20th century saw the release of Svante Arrhenius' book 'Worlds in the Making: The Evolution of the Universe' [1]. Within his topically diverse discussion resides the concept of panspermia, the hypothesis that describes life moving through interplanetary space [1] [2]. Arrhenius begins the chapter entitled 'Life through the Universe', by illustrating the cultural and historical importance of deliberating upon our origins and provides the biological worldview of his time. Arrhenius acknowledged how evolution by natural selection, had reached universal acceptance. Whilst the diversity of life on Earth now had a naturalistic explanation, the origins of terrestrial life were unexplained, as it is today [3] [4]. It is important to note that panspermia is not a replacement for abiogenesis [5], but a deliberation on the transfer of life throughout space and of the potential consequential seeding of life on other planetary bodies [2].

Arrhenius claimed to not share the optimism of the eminent British scientist Lord Kelvin who in an 1871 address to the British Association in Edinburgh, stated that whilst melting is a predictable fate of much of the substances involved in a space collision some debris must also be "shot forth in all directions" [6]. Kelvin continued with the postulation that if an impact were to occur on a body with living material, some of that would be scattered and ejected into space [6].

Arrhenius rejected this hypothesis on two grounds; the first being that he felt it was implausible for organisms to be robust enough to actually survive such a

violent impact. The second point of contention surrounded his observations that the compositional profile of meteorites were very different to the substrates upon which terrene organisms reside, and that the occurrence of such impacts is very rare [1]. These concerns will be addressed within this chapter. As a result Arrhenius postulated that perhaps due to the small nature of some organisms that solar radiation pressure could push them out into space, traversing interstellar space and onto other planets to seed them. This hypothesis is known today as radiopanspermia.

The core issue today with this hypothesis is the capacity of unshielded organisms to survive the hostility of interplanetary space. Terrestrial life is protected by the atmosphere from this harsh environment [7]. Ultraviolet (UV) radiation originating from the upper photosphere, chromosphere and corona of the sun is particular damaging, especially UVB and UVC (the latter is efficiently blocked by the Earth's atmosphere [8]) [9]. The efficacy of UVC at killing bacterial spores is ≥300 fold greater than that of UVB and UVA [9]. UV radiation is absorbed readily by biological macromolecules such as proteins, lipids and nucleic acids and alongside its high energy, UV exposure is highly lethal to exposed microorganisms [9].

Exposure to galactic cosmic rays are also detrimental to the propagation of microorganisms. These consist of high energy protons (90%), α particles (9%) and all other elements (1%) coming in from outside the solar system. They are able to interact with microbes at higher intensities, and for longer duration, than they would be traditionally exposed to on their planet of origin [10]. Biological damage as a result of radiation is proportional to the amount of energy deposited into a specimen [8]. However efficient repair mechanisms should also be noted in a number of species of microorganisms such as the gram positive sporulating *Bacillus subtilis.*

A contemporary version of panspermia exists and enlists the assistance of large impacts from meteorites; this is known as lithopanspermia [11]. This hypothesis assumes that life is extant on one of the planetary bodies [5]. In this scenario material is ejected from a crater post-impact at high velocity; in

some instances these velocities can exceed the impacted body's escape velocity.

Escape velocity can be expressed as follows:

$$v_e = \sqrt{\frac{2GM}{r}} \qquad (1)$$

where v_e and M are the escape velocity and mass of the impacted planetary body, r is the radius from the centre of gravity and G is the universal gravitational constant.

Volcanic ejection has been considered a source of material ejected from planets but dismissed because of an apparent inability to induce planetary escape velocity in the ejected material [11]. The transfer of material can be thought of as a stepwise series of hypothetical considerations as seen in figure 1; where the Earth and a secondary solar system body are given as examples of this scenario.
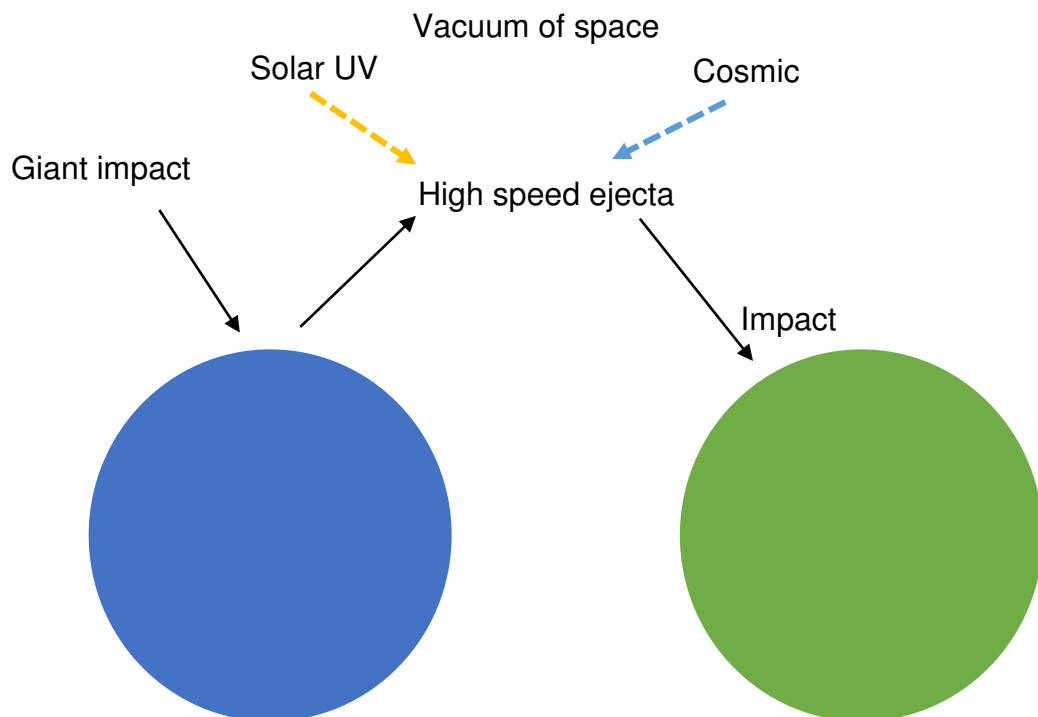
Figure 1: A schematic that illustrates the process of lithopanspermia, whereby material is ejected from a parent body travels through interplanetary space and impacts a secondary body. *Adapted from Burchell, 2010* [15].

In this model, samples must, firstly, escape their planet of origin, most reasonably as ejecta following a large impact. Secondly, survival in interplanetary space is paramount, and lastly the samples must impact or otherwise captured by a secondary body and land on this body surviving the shock pressures that this entails. Some researchers consider it highly probable that this has happened already [12]. Of course ejected fragments are exposed to the same solar UV and cosmic rays previously discussed, and so when speaking of fragments capable of acting as a viable vector of biological material, the implication is that they are large enough to provide sufficient shielding against the radiation exposure during their transit. A thorough but highly speculative attempt at calculating the probability of this process occurring, and delivering viable biological material can be seen in Clark, (2001) [13].

Equation (2) gives a formulation of these factors considered by Clark.

$$P_{AB} = (P_{biz})(P_{ee})(P_{sl})(P_{ss})(P_{se})(P_{rel})(P_{st})(P_{sp})(P_{efg})(P_{sc}) \tag{2}$$

In equation (2), the term P_{AB} refers to successful deposition on a planet B after a hypervelocity impact occurring on planet A. This is based on an overall estimate of the probability of P_{AB} derived from the product of the probabilities of several individual steps. The various terms of this formulation are described in table 1.

This formulation is limited in its utility and will not provide an explicit value of P_{AB}. It was noted by Clark that a number of these would have probabilities that are orders of magnitude less than 1. Two terms in the equation that are examples of extremely low probability, are P_{sp} and P_{sc}. These describe the probability of an ejected organism surviving potential predators (P_{sp}) and the probability of successfully competing with an indigenous population (P_{sc}), on the secondary planetary body, B. These are speculative due to the lack of known extra-terrestrial biospheres, and more importantly, a limited knowledge of how such biospheres may arise. As such, these two components will remain as terms that appeal to analogy (i.e. terrestrial biodiversity studies). Within Earth's biosphere, predation, parasitisation, and the impact of invasive species are highly important factors.

Clark concluded that the overall probability would be extremely low and that P_{AB} is not accurately calculable at present. Clark did however assert that evaluations of P_{AB} should be weighed against the large quantity of impacts during the early solar system on every planet and the potential for those planets to have been, however transiently, habitable.

Table 1: Terms in equation (2) which attempt to calculate the probability of successful transfer of life from one body (A) to another (B). *Adapted from Clark, 2001* [13].

P_{biz} = Probability that an impact occurs in a biologically inhabited region

P_{rel} = If the organism is encased in rock, this is the probability that it'll be released

P_{ee} = Probability of ejection onto an ejection velocity

P_{st} = Probability that B is non-toxic

P_{sl} = Probability that an organisms survives launch

P_{sp} = Probability that the organism survives potential predators on B

P_{ss} = Probability of survival in space

P_{efg} = Probability of reaching a favourable growth environment

P_{se} = Probability that an organism survives an impact onto B

P_{sc} = Probability that an organism from A can compete successfully with the indigenous population.

1.2. Extra-terrestrial meteorites.

It is now known that material has been ejected from the lunar and Martian surface following large impacts, and has subsequently impacted on Earth as meteorites. The presence of this material from other large Solar System bodies has led to a resurgence of interest in panspermia in the form of lithopanspermia [14]. This raises the question of whether terrestrial meteorites in turn could be found on other solar system bodies. Since we know life exists on Earth the consideration of whether any biological contaminants could be present amongst this ejecta, is then a matter of great interest. It is also important to note that transmission need not be limited to living organisms either; the transfer of fossilised material, as well as any other biomarker that happens to be ejected could occur. This then needs to be shielded in interplanetary space and withstand the impact with a second solar system body [15].

We first consider lunar meteorites. These are rocks that were ejected from the lunar surface due to a meteorite impact, and are then captured by the gravitational field of Earth (the aforementioned secondary body) [16] [17]. A frequently updated source that identifies and catalogues this material is the Lunar Meteorite Database of The Meteoritical Society's Meteoritical Bulletin. As of the 28th July 2014, 171 lunar meteorites have been logged here and published in the Bulletin [18]. They have been found in a number of locations including the cold desert of Antarctica (e.g. the meteorite Yamato 791197) and hot deserts in North West Africa (e.g. the meteorite North West Africa 482) [17]. These lunar meteorites consist of basaltic, feldsparic and mingled (basaltic and feldsparic) samples [19]. While these samples originate from unknown depths and loci on the moon, they provide a more representative sample of lunar geology compared to the Luna and Apollo missions, as a result of the random sampling of impact ejection; especially important as only 5% of the lunar crust has been selectively sampled during human led missions [20] [21] [22]. The highly varied composition of the samples identified, promote a wide distribution of origins and thus highlights the geological benefits of these meteorites [17].

There are approximately 150 Martian meteorites that have been categorised [23]. The unique atmospheric composition of Mars and the presence of similar gaseous components within these meteorites provides a strong line of evidence that these meteorites originated from Mars [24]. This set of meteorites are denoted SNC due to specific petrological characteristics. The 'S' in SNC refers to Shergottites, comprised of basalt from quickly cooled lavas and peridotites originating from slow cooled magma within large magma bodies. The 'N' represents the Nakhlites such as clinopyroxenite and finally the 'C' represents the Chassigny class.

The evidence for the concept of Martian origin depends heavily on the gases trapped within the rocks. In the Shergottites, (meteorites such as EET79001) there is a noble gas profile consisting of examples such as ^{132}Xe, ^{129}Xe and ^{36}Ar as well as other gases such as N_2 and O_2. This shows an abundance that significantly resembles (verging on unity) with the known Martian atmosphere recorded from the Viking mission [25]. The mode of action by which the gases get trapped and concentrated in the substrate involve shock melting after a large impact, which in this case occurred on the surface of Mars [25]. With exchange of Martian meteorites and lunar meteorites with the Earth, it would appear to be reasonable to conclude that terrestrial meteorites could also be found upon other bodies within the solar system. There are important differences between the planets that must be considered when looking at the viability of this ejection model. For instance the Earth has a much denser atmosphere than Mars, which acts to restrict ejecta from leaving. Earth's mass is also greater than Mars and hence has a greater escape velocity. However Mileikowsky in [10], concluded that it could be possible.

1.3. Modelling interplanetary transfer.

The evidence of extra-terrestrial meteorites found on Earth stimulated new investigations into realistic mechanisms of panspermia. Spall ejection theory is the key mechanism in lithopanspermia; here an impact induces a pressure gradient below the planetary surface. The surface material near the impact is accelerated away from the impact area, and the ejected material is only lightly shocked, relatively speaking [11]. This is vital for the persistence of biological

material, as organisms within the rock at the impact point would be killed as a result of the heat from the shock introduced by the impact [26]. That it is surface material that is ejected in this model is also important, as it is considered to be the section of the Earth's crust that is the most biologically active [26].

The direct transfer of terrestrial material has been shown to be a reasonable topic of discussion by utilising modelling programs that can simulate many particles ejected from the Earth's surface after a large impact. Armstrong's paper published in *Earth, Moon, and Planets* provides such a simulation, finding the impact speeds and impact distribution of particles ejected from the Earth's surface impacting onto the Moon [27]. This paper and others like it, aid in future lunar exploration missions by providing a map for the prime locations of terrestrial meteorites. The Moon provides an ideal retainer for meteorites ejected from the Earth's surface as well as from the surface of Venus and Mars. [27] This is a result of the lack of an atmosphere combined with more stable geology than the Earth [27] [15]. This has led to the labelling of the lunar surface as Earth's 'attic' [28] and as a 'witness plate' to the environmental occurrences of near-Earth space [29]. Armstrong's paper utilised nine simulations at varying Earth-Moon distances. The Earth-Moon distance has changed over time due to lunar recession, this phenomena is acknowledged in this paper by using values for this distance of $21R_\oplus$ to $61R_\oplus$ (with $R_\oplus$ representing the radius of the Earth). The impact angle and velocity vector for each collision was computed. Of the 1.4×10^6 particles simulated, 4678 interacted with the lunar surface. This meant that enough data was available to construct a map that highlights meteorite impacts on the Moon with respect to their incoming velocities, see figures 2 and 3.

These distribution maps and other data provided by Armstrong yield some interesting results. For example, impact speeds ranged from 0.1 to 5 km s^{-1} and the impacts with the greatest vertical impact speed are found on the Moon's leading edge [27].

Figure 2: A map showing the distribution of meteorites on the lunar surface after simulating particles (terrestrial ejecta) travelling to the moon. This image represents the near side lunar surface and clearly shows a high density of polar impacts. Impact speeds are indicated by the size of the dot, see the lower left of the image for a scale [27].

Also the distribution of impacts is far from uniform [27]. Overall this establishes that on the lunar surface there would be a wide distribution of terrestrial meteorites. Which, given the stability of the environment can be considered, a repository of historical ejecta across its surface. The angle of impact was also expounded as an important factor, given that oblique impacts experience lower peak pressures than direct impacts. For example, Crawford et al., note

that an impact arriving with an angle of 45° would experience a peak pressure of 70% that of a vertical impact [30]. As part of [27], the distribution of impact angles was found; 50% of the ejecta impacted at less than 20° from the horizontal [27]. This further enhances the possibility of finding viable biomarkers and also provides an opportunity to investigate the status of early earth [30]. These markers may include indicative terrestrial isotopic ratios, organic carbon and even microfossils [30].
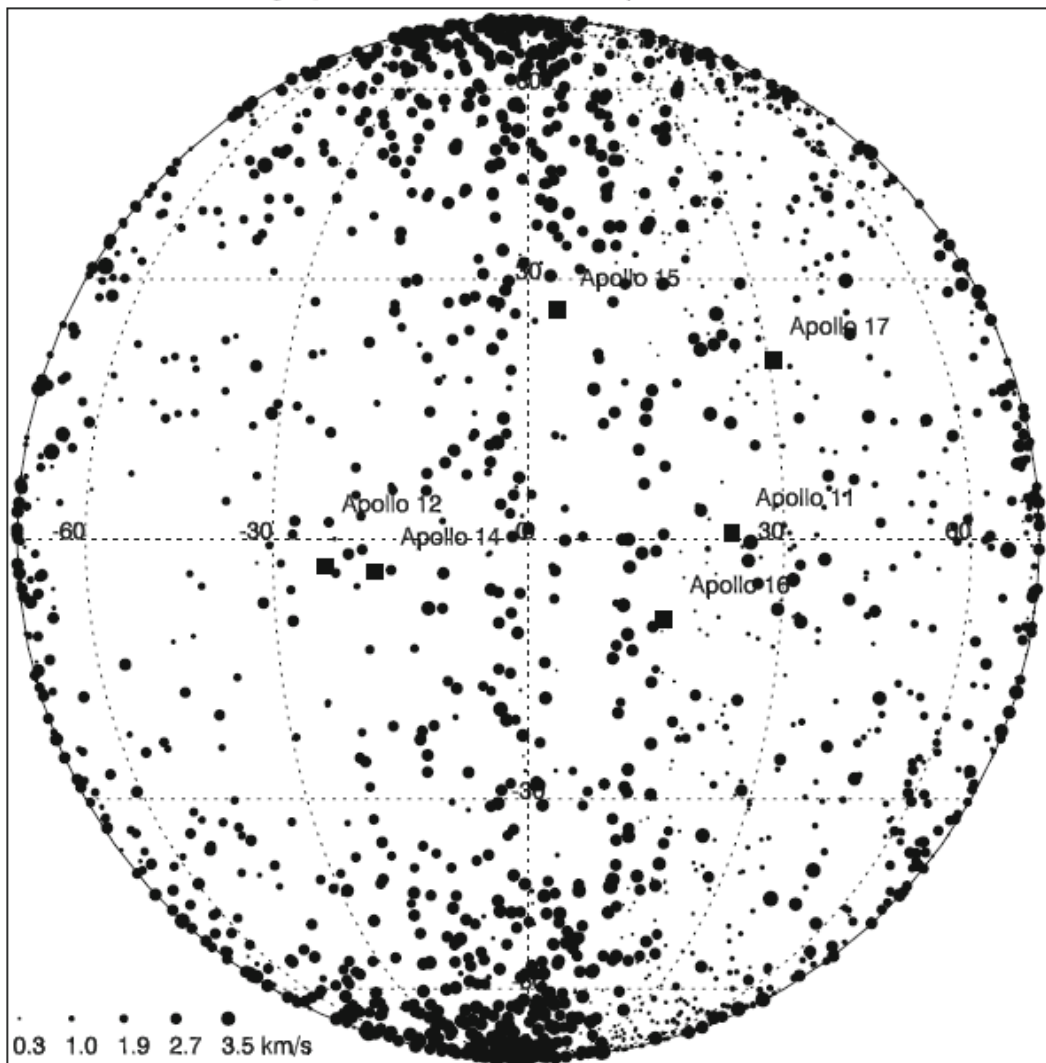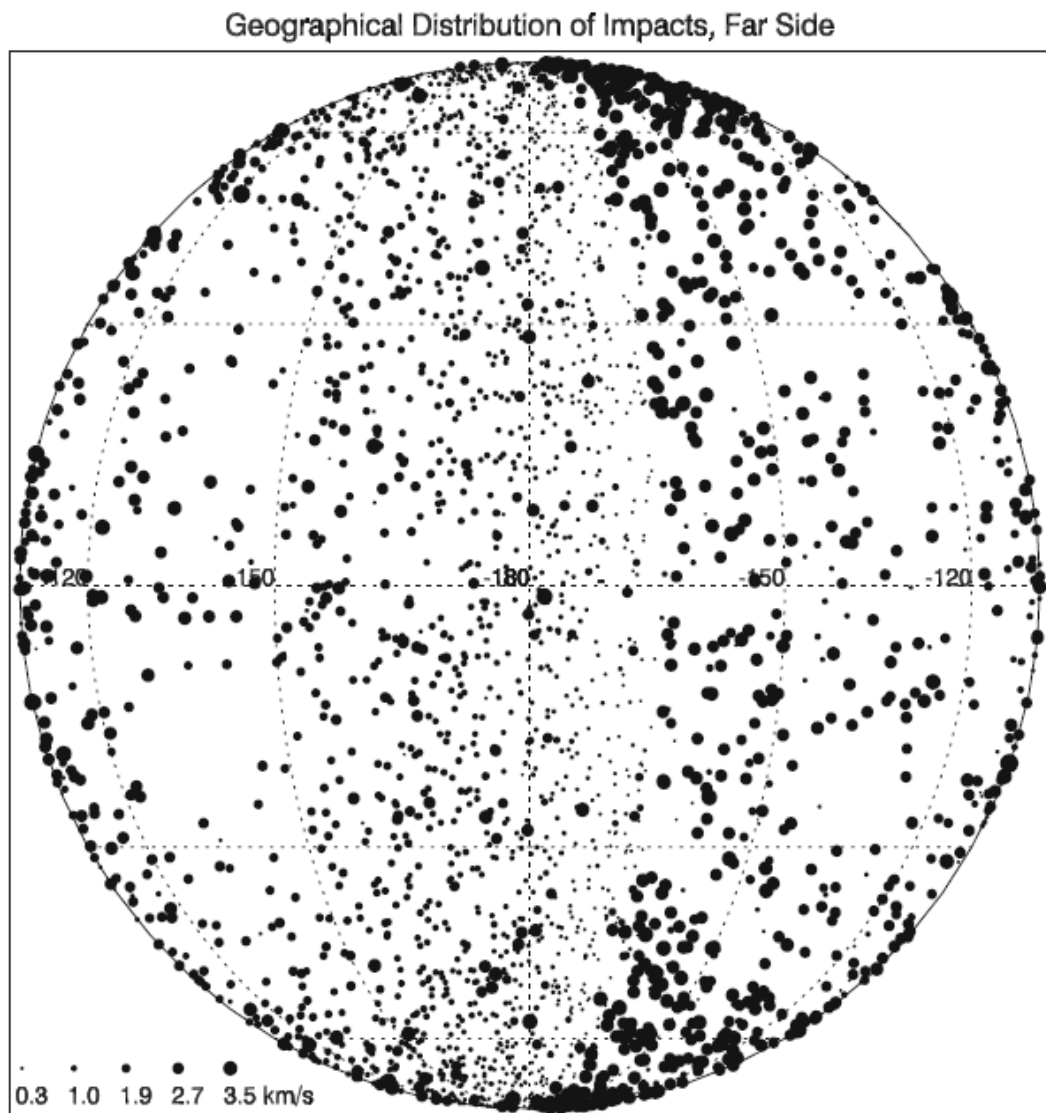

Figure 3: A map showing the distribution of meteorites on the lunar surface after simulating particles (terrestrial ejecta). This image represents the far side lunar surface and contains a high number of impacts at a velocity <1.0 km s^{-1}. Impact speeds are indicated by the size of the dot, see the lower left of the image for a scale [27].

Looking further than the Moon, another paper that attempts to simulate terrene ejecta was published by Reyes-Ruiz et al. [31]. This paper considers particles that would be influenced by the gravitational fields of the component bodies of the solar system. Whilst the particles were programmed to interact with the massive bodies of the system, the author's removed the capacity for inter-particle interaction [31]. This paper showed the relationship between the ejection velocity and the probability of interacting with those massive bodies. The escape velocity of the Earth is approximately 11.2 km s^{-1} and low ejection velocities were calculated; this led to the findings that a ~1% difference between the escape velocity and ejecta velocity (11.22 km s^{-1}) results in a proclivity towards particles remaining in Earth's orbit and 5% actually returned to the surface [31]. Fewer particles returned to Earth as the ejecta velocity increased. One issue seen in the simulation was that while increasing the velocity of ejecta increased the distances travelled of the ejected material, there was also a diminished capacity to strike the other solar system bodies. Whilst particles were interacting with Mars and the lunar surface in minute proportions, the calculated particles would "stream past" them due to their small masses [31]. The author's place emphasis on the ability for terrene ejecta to travel to bodies that are tentatively associated with life sustaining environments, these include: Mars, the Jovian satellites Europa and Ganymede, and the Saturnian moons Titan and Enceladus [31].

This concept of material ejected from the Earth's surface reaching the moons of Jupiter and Saturn, etc., is also supported by simulations carried out by Worth et al., although they also found this to be a rare occurrence [32]. In this study the author's show that rocks ejected from Mars and Earth can interact with all of the solar system's terrestrial planets. They utilised a random distribution of particles placed at 2×10^{11} cm from Earth and at 1×10^{11} cm from Mars. Also included was the orbital velocity of the planet that the particles originated from, as well as a velocity vector that represented ejection from the parent body. This radial velocity was randomly assigned with values ranging from 1 to 3 times that of the escape velocity. The author's estimated that over a period of 3.8 Gyr (i.e. since the end of the late heavy bombardment), 2×10^8 meteoroids have been ejected from Earth into interplanetary space and 8×10^8

from Mars. The reason for the greater levels of ejecta from the Martian surface is due to the lesser relative surface gravity to Earth. Earth's surface gravity is significantly stronger and thus an impact will eject less material. A corollary to this is that large numbers of viable fragments can be ejected from the Martian surface as a result of smaller impacts [32]. This comparison between planets is important as it has been shown that very high speed impacts eject far more material than smaller impacts [33]. A 100 km impact crater ejects approximately 7000 times more material at a velocity greater than or equal to the Martian escape velocity than a crater that is just 10 km across [33]. Nevertheless combined with the results of Reyes-Ruiz et al. this does suggest that a small, but finite, number of Earth rocks could have reached other Solar System bodies.

1.4. Biological Studies and Space.

Given that rocks from planets can be ejected and impact other Solar System bodies, it is interesting to ask whether any bio-load could survive. Survival of organisms under space conditions has been tested in a variety of ways. For example, de la Torre et al. [34] showed that organisms can survive and remain viable after exposure to the environment of space. Lithopanspermia/BIOPAN-6 was an experiment that involved the microbial symbionts, lichen, and exposed them to the vacuum of space, cosmic radiation and solar radiation at a number of electromagnetic wavelengths ($\lambda > 110$ nm, $\lambda > 200$ nm, $\lambda > 290$ nm, $\lambda > 400$nm) [34].

BIOPAN (see figure 4) is a facility that provides short term exposure in space. It consists of two experimental sections and opens at 180° once in low Earth orbit [35] (an altitude of ~300 km [34]) (see figure 4). It is associated with the Russian FOTON class of robotic satellites and is launched utilising a Soyuz rocket. In this instance the FOTON M3 was utilised with the BIOPAN-6 mission. Previous FOTON missions have had varied success, with FOTON M1 exploding during launch in 2002, FOTON M2 however did succeed in 2005 [36] [37].

Temperature is measured on Biopan using an AD590 sensor, whilst radiation is measured using a thermoluminescence detector. Pressure and ultraviolet (UV) radiation is also monitored [34]. The experimental modules on BIOPAN hold samples and electromagnetic radiation filters specific to the experimental protocol. For instance the inorganic salt, MgF_2 is transparent to all wavelengths of electromagnetic radiation above λ110 nm [34]. Synthetic quartz provided transmission of λ>200 nm which acts to simulate the Martian UV and visible light exposure [34]. The modules contained 32 wells (13 mm in width and 9 mm in height) that can contain the samples. In order to provide a control, terrestrial visible and UV radiation levels were filtered (λ>290 nm) [34]. There was also a filter that prevented transmission of all solar UV radiation (λ>400 nm) [34]. Dark samples were also included, these were not exposed to any electromagnetic radiation [34].
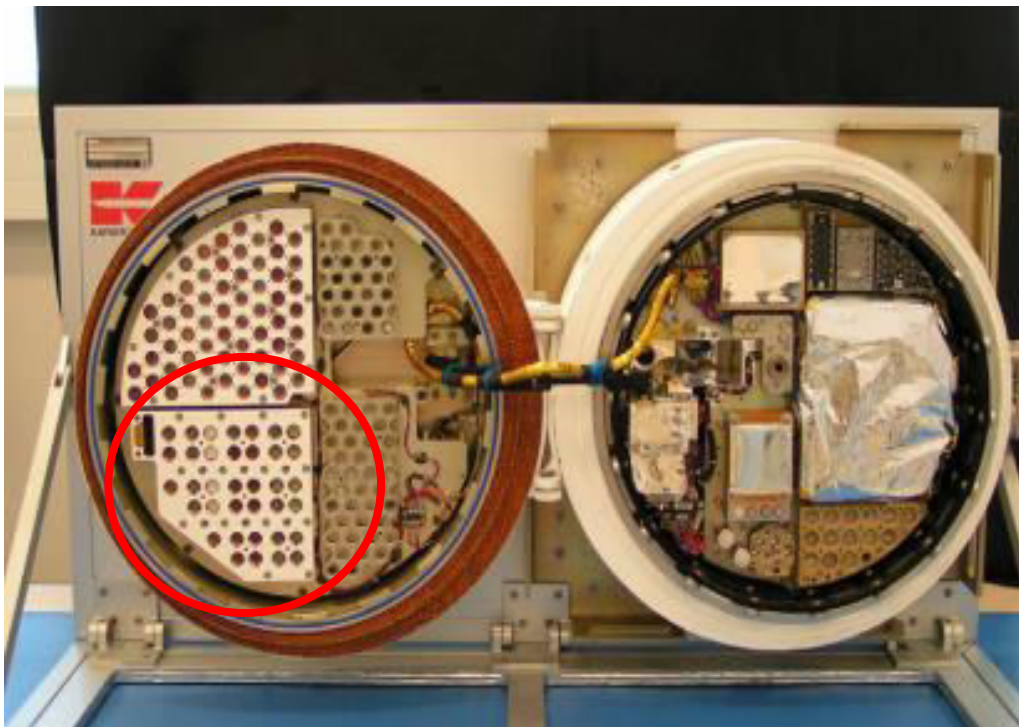

Figure 4: Image of Biopan-6 facility in an open configuration. Circled is a bank of 36 wells to which biological samples can be stored, and the associated temperature sensor and radiation detector. *From* [34].

The purpose of Lithopanspermia/BIOPAN-6 was to identify the effects of the space environment, in the context of the physicochemical and biological properties of the samples post flight. That is, the samples were exposed to space then the experiment returned to Earth for analysis. The organisms used were *Rhizocarpon geographicum*, *Xanthoria elegans* and *Apicilla fruticulosa* [34]. Samples of *R geographicum* were modified to test the effects of removing the protective cortical layer, which was extracted manually via scalpel. Also discussed in [34] was the Lithopanspermia/STONE experiment that tested the viability of organisms associated with the outer shell of the FOTON satellite after re-entry [34]. Entry into the atmosphere is a violent phenomenon and the results of this Lithopanspermia/STONE would not only yield consequences to the lithopanspermia hypothesis but also to microbiological sterilisation of spacecraft that enter other planetary atmospheres.

The results of both Lithopanspermia/BIOPAN-6 and STONE were interesting. STONE established that, at least in this experiment, organisms did not survive re-entry, this was presumed to be a result of the intense heat. However the author's note that the rock substrate may not have been thick enough to protect the biological sample. It was also proposed that an unforeseen phenomena occurred, wherein super-hot gases, a consequence of ablation, had permeated the void between the sample and holder had induced violent local heating [34]. This was supported by post flight evidence that showed how the surface not exposed to the atmosphere had melted [34], as a consequence further experimentation should be carried out.

The results of BIOPAN-6 were also informative, albeit perhaps more fruitful. This experiment concluded that photosystem II activity recovered fully after exposure to the vacuum of space [34]. There was also a negligible decrease in photosystem II activity when exposed to solar electromagnetic radiation, although *X. elegans* exposed to λ>400 nm, had a 20% reduction in activity [34]. Photosystem II is a pigment-protein complex found within the thylakoid membrane of photosynthesising organisms involved in the light dependent reactions (in series with photosystem I). Interestingly the sample of *R. geographicum* that had had their protective cortex removed did have a significant reduction in photosystem II when exposed to λ>110nm, >290nm

and to λ>400nm [34]. The author's reasoned that incomplete removal of the cortex led to variable photosystem II activity. As a result it would be prudent to retest with complete removal to verify the protective capacity of the cortex against the gamut of solar electromagnetic radiation [34]. Also observed was that exposure to λ>400 nm was the most deleterious across the species in the context of photosystem II activity [34].

When compared to the 'dark' samples, those that were exposed to solar radiation had reduced viability; and the 'dark' samples in turn had reduced viability relative to the ground controls on Earth [34]. The viability of the organisms was established with confocal laser scanning microscopy and the FUN-1 stain [34]. FUN-1 is a fluorescent probe that is able to passively diffuse into the cytoplasm of a number of cell types (living and dead but not mammalian [38]) and stain it green. This dye is then processed by the cell and this leads to the formation of red cylindrical intravacuolar structures [38]. As a consequence the conversion of the green fluorescent dye to red is an indicator of metabolic activity and thus cell vitality; dead cells still fluoresce with a diffuse green colour [38]. *R. geographicum* had a considerable reduction in viability when compared with ground controls, with a viability value of (52.3 ± 9.9)% against 92% of the controls [34]. This occurred in all instances of electromagnetic radiation (λ>110nm). *X. elegans* also saw a reduction in viability, where the ground control samples had a vitality value of 95%, and sun exposed *X. elegans* had values ranging from 67% to 75% through the range of electromagnetic λ tested [34]. Important when discussing FUN-1 staining is that this can be used to differentiate between damaged and undamaged cells, of either the phycobiont or the mycobiont. The findings were that *R. geographicum* had a greater amount of damage to the mycobiont cells, whereas *X. elegans* indicated larger degrees of damage to the phycobiont [34]. The pressure differential between low Earth orbit and interplanetary space is significant; the value for the vacuum of interplanetary space is approximately at 10^{-14} Pa, whereas low Earth orbit is in a range between 10^{-7} and 10^{-4} Pa [36]. This means that while survivability in space has been shown in the Lithopanspermia/BIOPAN-6 experiment, it's important to note that the intense

environment of interplanetary space has not been induced upon biological samples.

In another type of experiment, a Martian analogue field site was identified in Antarctica and the granite associated lichen that inhabited microniches were extracted [39]. These microniches are composed of fissures and cracks and they provide protection against general weathering and UV irradiation. As has previously been described, protection against UV is vital in the context of astrobiology when considering microbiological persistence in space. Samples of the organism were then introduced to a system that replicated the approximated surface conditions on Mars. The organism that was exposed in this experimental protocol [39] was *Pleopsidium chlorophanum*, one of nine species belonging to the genus *Pleopsidium* [40]. The German Aerospace Centre's (DLR) Institute of Planetary Research in Berlin was responsible for the study and the protocol was run within the Mars Simulation Facility (MSF). This facility has a climate chamber with a volume of 240,000 cm^3 (that in turn contains an experimental compartment that can be independently controlled). As well as UV exposure, the modulation of atmospheric pressures (average of 800 Pa) play a large role in this project [39].

Inside the MSF were six samples, three of which were exposed directly to Martian surface radiation supplied by a xenon lamp [39]. The second triplet was protected in a Mars-like niche condition, indirectly irradiated (scattered and reflected radiation from the xenon lamp), directly affected by the gas pipe that provided a simulated Martian atmosphere and exposed to doses of UVB radiation from a light-emitting diode (LED) on a diurnal cycle [39]. The cycle followed the diurnal solar cycle on Mars using values of 16 hours of irradiative activity and 8 hours of inactivity. The gas pipe simulated the Martian gaseous atmosphere, whereby 95% of the constituents was CO_2, and the remaining 5% was made up of N_2 and O_2 (4% and 1% respectively) [39]. Further adding to the simulation was the inclusion of an appropriate Martian mineralogical profile within the regolith that the samples were to be embedded [39]. This consisted of gabbro, olivine, quartz, haematite, goethite and gypsum; with gabbro and gypsum conferring the most significant proportions in weight percent (32 wt% and 30 wt% respectively) [39].

The results of this study show that the high cumulative radiation dose (6344 kJ m^{-2}) that replicated a month's worth of occupying an unprotected loci on Mars, reduced the activity of photosynthesis of the lichen samples [39]. In fact the drop in yield was so significant that the author's brought into doubt the concept that these specimens were effectively photosynthesising at all [39]. However the protected samples with a cumulative dose of 269 kJ m^{-2} adapted rapidly, to the extent that these samples had an increase in photosynthetic activity of 17% over the measured Antarctic samples in situ [39]. FUN-1 staining was again used to test the cell vitality of the organisms [39]. The results show that fungal cells did perish, but that when in closer proximity to the phycobiont the survivability was enhanced; this was presumably due to a local phenomenon of O_2 production by the algal cell that promoted a survival gradient [39]. Those fungal cells that were outside the sphere of photosynthetic influence would perish due to the high CO_2 atmosphere whereas those fungal cells close to the algae could absorb O_2. This is because this fungi is an aerobe heterotroph, meaning that it requires free O_2 to survive (as well as being unable to fix carbon itself).

The relevance of this paper to future extra-terrestrial expeditions should not be underestimated; it has now been established that a Martian-like environment can induce adaptation in a terrestrial organism and thus potential contaminants should be screened for thoroughly. It is also important to note that survival in protected loci such as microniches increases and thus the search for indigenous biological samples could be targeted to these areas.

1.5. Surviving acceleration and impacts.

As well as overcoming the harsh environment of space, organisms must also be able to survive the induced acceleration as spalled material and the impact that deposits them onto a new body. This type of survival is not a trivial matter as the substrate undergoes significant shock pressures [15]. Experimental studies have dealt with this both in the context of organisms (e.g. *B. subtilis* [41]), biological material (e.g. seeds [42]) and of organic molecules (e.g. amino acids [43]). A number of methods have been engineered to achieve

hypervelocity impacts which have been informally described as having velocities exceeding 2 or 3 km s^{-1} [44].

The importance of extreme acceleration and jerk (a change in acceleration) was considered minimal as a key lethality factor in the lithopanspermia hypothesis by Mastrapa et al [45]. They used a tabletop centrifuge device which was run at 100,000 rpm which correlates with an acceleration of 4.27x10^6 m s^{-2}. The *B. subtilis* spores persisted after exposure to high acceleration, however due to the 2 minutes it took to reach the maximum centrifugal acceleration, this test was limited in the context of jerk [45]. The jerk component was accounted for in a series of ballistics experiments involving *Deinococcus radiodurans* cells and *B. subtilis* spores were loading into lead pellets and fired into plasticene via a compressed air pellet rifle. In the ballistic experiments *B. subtilis* was exposed to an acceleration (average) of 4.5x10^6 m s^{-2} and jerk (average) of 1.5x10^{11} m s^{-3}, this experiment also showed persistence of the organisms [45].

In order to expose microbial communities to intense shock pressures, Stöffler et al. sandwiched viable microorganisms between two gabbro plates which act as Martian rock analogues which are then exposed to shock pressures as a result of a high explosive [41]. The organisms used were *B. subtilis* spores, *X. elegans* and the cyanobacteria *Chroococcidiopsis*. The microbes experienced shock pressures from 5 GPa to 50 GPa. At 50 GPa, *B. subtilis*' survival rates dropped below the capacity to detect them and so the upper limit established for survival of this organism was 42 GPa, where survival was reduced to 10^{-4} [41]. This exceeds prior attempts of exposing *B. subtilis* to high GPa when it is associated with a geological substrate; in prior tests 32 GPa was discussed alongside the corresponding shock temperature of 390°C [46]. *X. elegans* showed structural preservation at 10 GPa but at 42 GPa they were mostly destroyed although a number of ascospores which are the propagule component of the mycobiont did survive [47] [41]. Survival in *X. elegans* was determined by the previously described vitality stain. *Chroococcidiopsis* exhibited the lowest survival whereby no survivors were detected beyond 10 GPa [41].

In 2001 Burchell et al. showed that by using a two-stage light gas gun [44] (whose properties will be further discussed in chapter two), the robust, gram-positive bacterium *Rhodococcus erythropolis* could be fired into Glucose Yeast Extract medium and recovered [48]. The velocities experienced by *R. erythropolis* was 5.0 ± 0.1 km s^{-1}. Yeast has also been fired using this mechanism, in this case *Saccharomyces cerevisiae* [49]. In this study a noticeable decrease in survival probability related to an increase in shock pressure; there was approximately 50% survival at low velocities (1 km s^{-1}) compared to the approximately 10^{-3}% survival probability at 7.4 km s^{-1} [49].

Other options of testing this impact component of lithopanspermia involve examining directly the capacity of bacterial spores to survive spallation. *B. subtilis* spores were utilised in conjunction with the vertical gun range at the NASA Ames Research Centre [50] the setup can be seen in figure 5.
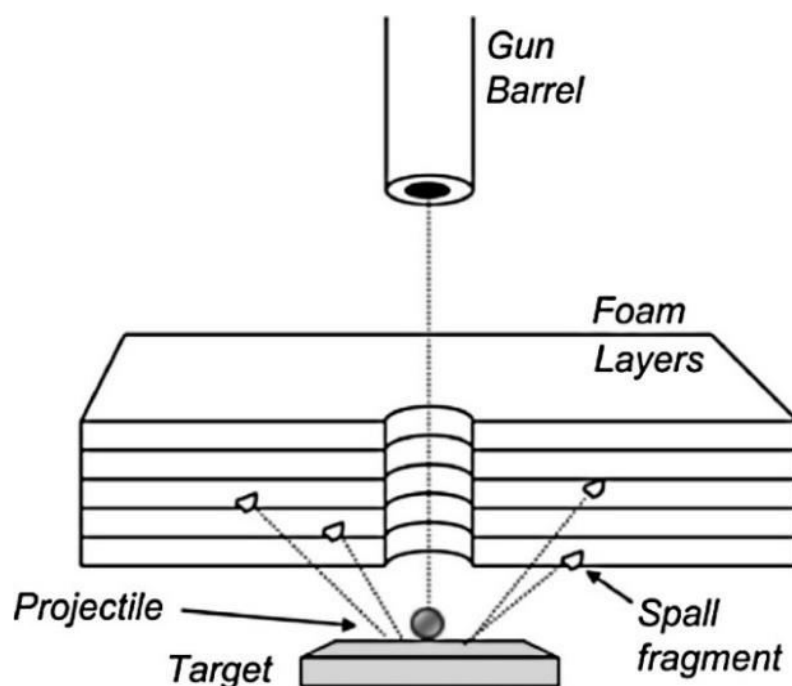

Figure 5: This schematic illustrates how fragments that are ejected from a perpendicular impact are embedded within the foam recovery layers. *From Fajardo-Cavazos et al* [50]

In the experiments at NASA Ames, a gun barrel guides a projectile into a perpendicular impact with a doped (8×10^9 total spores) granite target and the spall fragments were collected in a layered polyurethane foam recovery plate. The process of embedding in the foam produced spall tracks; within these tracks spores were recovered. In one spall track (#4) 507 colonies were obtained [50]. The velocity of the impact was 5.4 km s^{-1} which is in line with other hypervelocity impact studies, with a calculated peak shock pressure in the impact of 57.1 GPa [50].

The evidence base for spallation and survival of bacteria is also supported by earlier literature whereby a target consisting of a frozen suspension containing high concentrations of *R. erythropolis* ($10^9 - 10^{10}$ cells/mL) was fired at using a 1mm aluminium sphere at velocities of 4.90 - 5.36 km s^{-1} [5]. Here ejecta from the impact was retained in 5 chambers with different angular ranges, from 0-25° to 75-85° and the findings showed culturable samples of *R. erythropolis* in each chamber [5]. The authors did note an issue with the low pressure that the target chamber that induced the ice target to sublimate away; in a controlled trial this process was found to transfer bacterial samples. While the numbers transferred were small (1-5% of the samples obtained from firing of the gun into doped ice targets). Accordingly this issue was ameliorated by sandwiching the doped ice layer between two 5mm layers of sterile water and then frozen. This then allowed for sublimation but prevented bacterial transfer. A second shot programme was carried out with the modified ice target and the original results were confirmed; spalled ice fragments do carry *R. erythropolis* in all angles tested and can be recovered successfully [5].

1.6. Summary.

This chapter has provided context within which this project will sit. It has been shown that biological materials can survive shocks in the GPa range, and impact speeds of 1-5 km s^{-1}. They can also survive conditions found in low Earth orbit and on Mars.

In the rest of this thesis we focus on a particular problem not previously considered in experiments. Namely can microfossils 'survive' high velocity impacts and the shock pressures that such impacts induce? The velocity of the projectiles will match experimentally the impact speeds seen in [27] (1 - 5 km s^{-1}), i.e. they are in the range applicable to impacts on the moon of terrestrial ejecta. A new method is also developed to enable the firing of samples at high speeds which contain liquid water. Both investigations will increase the range of materials that can be considered in future studies.

CHAPTER TWO:

METHODOLOGY.

Within this chapter the equipment used during these projects will be described and the experimental protocols will also be detailed. Particular focus has been given to the two-stage light-gas gun at the University of Kent, which the high velocity projects were based around. Other specialist equipment includes a Hitachi Scanning Electron Microscope. There are two projects described herein:

1. Survival of Fossils Under Extreme Shocks Induced by Hypervelocity Impacts
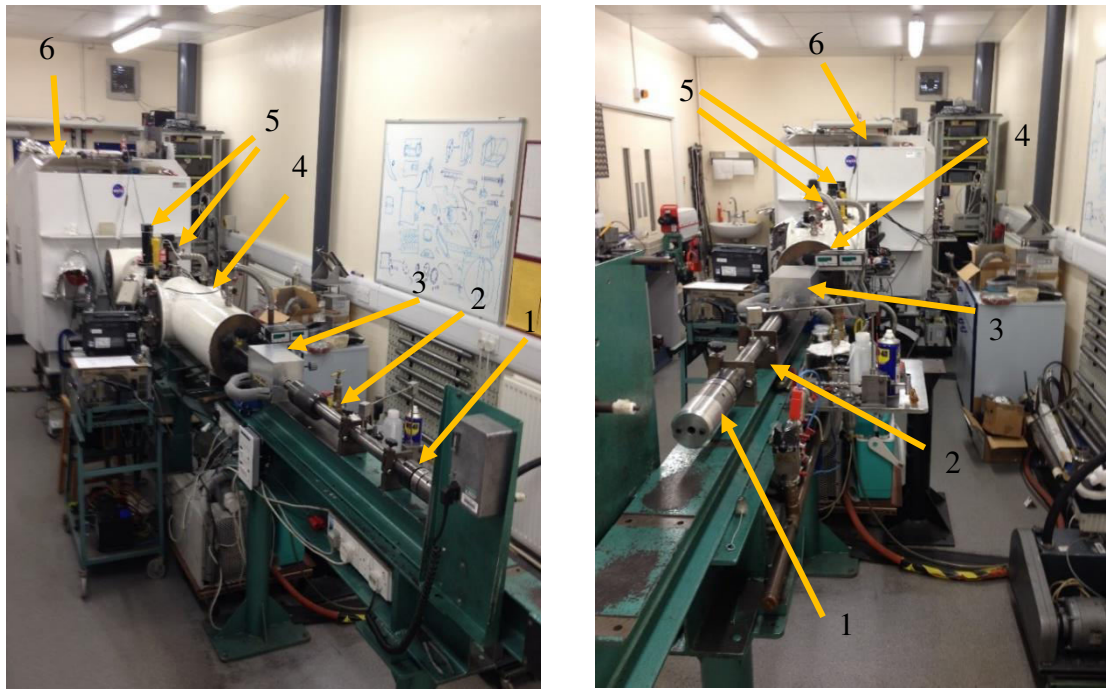2. Liquid core sabot design

2.1. Two-stage light-gas gun.

Figure 6: Two images of the light-gas gun at the University of Kent impact laboratory. Key gun components have been labelled. 1) Powder chamber 2) Pump tube 3) Launch tube 4) Blast tank 5) Two light curtains associated with photodiodes 6) Target chamber.

High velocity impacts were achieved in these projects by the use of a light-gas gun propelling projectiles into select targets [44]. Figure 6 shows the major components of the light-gas gun:

2.1.1 Mechanics and components of the gun.

Propulsion in the gun is initiated by the burning of gun powder within a powder chamber. The gun powder cartridge is filled within the laboratory and is engaged by a firing pin. The ignition mechanism is a pendulum that is held in place via a switch. This switch is in turn controlled from outside the gun room for safety. Once the switch is pressed, the pendulum is released and swings down to strike the firing pin, which in turn ignites the gunpowder cartridge.

Controlled variation in the final speed is provided by altering the amount of powder and the powder's burning speed. This explosive charge accelerates a piston along the pump tube; this tube has previously been evacuated of air and then refilled with a chosen low relative molecular mass gas which is compressed by the piston (figure 7).
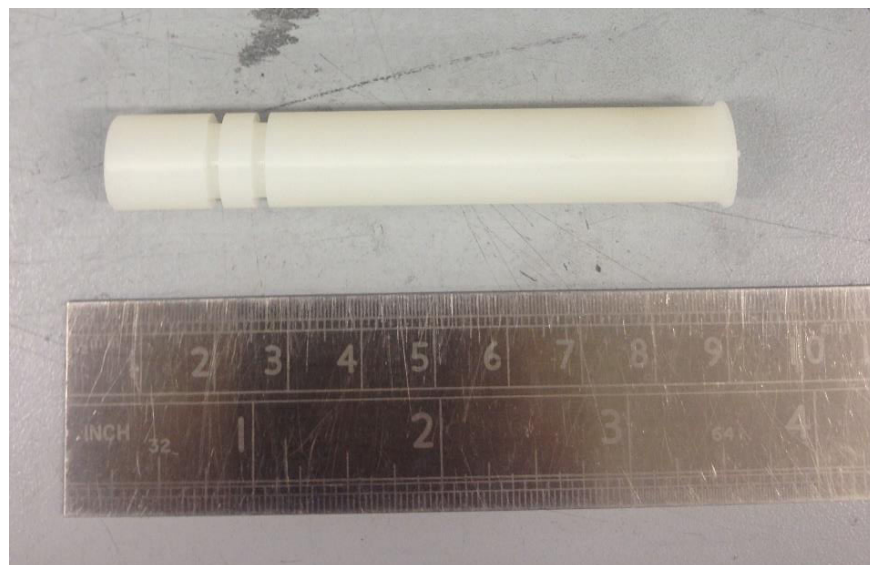

Figure 7: Image showing a nylon piston that is forced along the pump tube and compresses a low molecular weight gas. The left hand side of the piston shows two grooves, within which the 'O' rings sit. The piston is 82 mm in length and 12.7 mm in diameter.

Gases used in the pump tube include hydrogen, helium and nitrogen. These gases are pre-pressurised within the pump tube, to give extra control over final velocity. Low pressure gas will lead to a higher velocity and the inverse is true of high gas pressures. The pistons are sized to allow for a snug fit within. The gas tight seal within the pump tube is provided by rubber 'O' rings fitted onto the piston (the grooves that the 'O' rings are set into on the piston can be seen in figure 7.

While the rear of the pump tube is sealed by the piston, the opposite end is sealed with a burst disk. This is a thin circular cap of aluminium which will rupture when the pump tube reaches a critical gas pressure. The burst disk can be weakened by introducing score marks to allow for a lower pressure rupture. The gas escapes due to the ruptured diaphragm and the projectile is consequently accelerated [44]. See figure 8 for an image of an aluminium burst disc. The tolerances and sizes of each component are paramount for performance.

Figure 8: Image showing two aluminium burst discs. The disc is broken once a desired pressure is realised within the pump tube. The discs are 12.7 mm in diameter and 0.5 mm thick.

Immediately after the burst disc is a sabot, mounted in the launch tube. The sabot is a casing that allows for projectiles to be fired that do not fit efficiently within the barrel (launch tube). The sabot provides a tight seal around the items to be fired and the barrel itself, preventing gas from escaping around it. The sabot and its contents are then forced along the barrel into the blast tank as a result of expanding gas following the rupturing of the burst disk. In some experiments the sabot after - being forced out of the launch tube and into the blast tank – will be discarded. This uses a 'split' sabot, which has interlocking teeth that can 'unlock' mid-flight and allow for the items previously encased to continue towards impact. The unlocking occurs when the 'split' sabot exits the narrow launch tube into the wider blast tank and is no longer internally confined. However a solid sabot (figure 9) was used in the experiments here, meaning that there is no discarding of the sabot during flight.
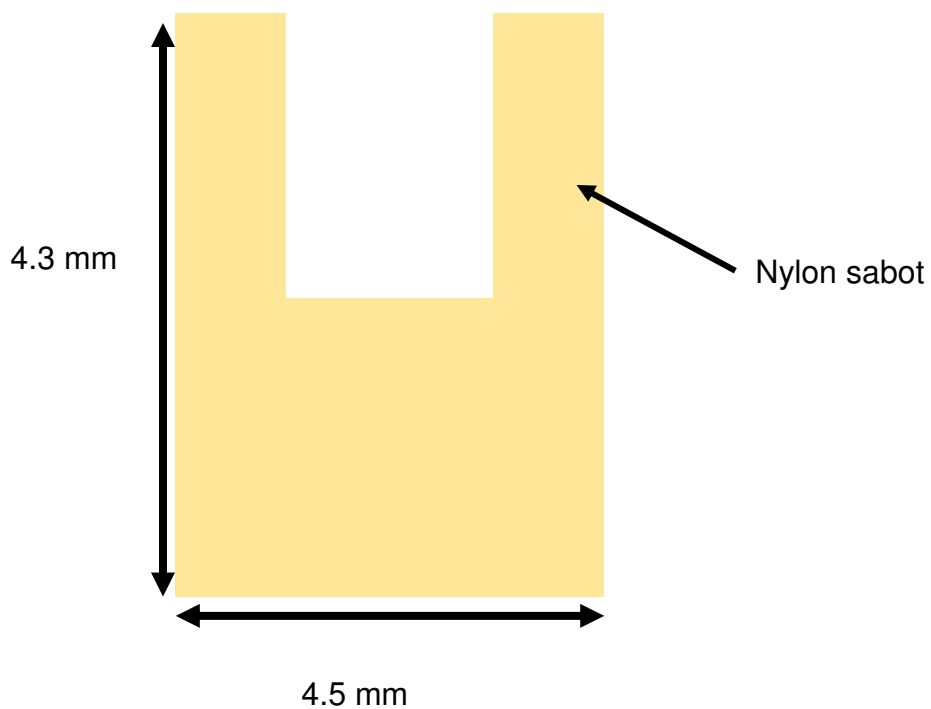
Figure 9: Cross-sectional illustration of a cylindrical nylon sabot with a central well (2.5 mm in diameter and 2.5 mm in depth) where the projectile sits is also featured. The sabot in this figure is positioned vertically but is positioned horizontally within the gun.

In the blast tank is a metal plate with a central hole positioned in line with the launch tube. This captures the parts of the 'split' sabot as they separate and travel off axis. The projectile (or here a solid sabot) passes uninterrupted through the central hole. The blast tank is evacuated to a low pressure to stop slowing of the sabot in flight. Once the solid sabot has left the blast tank it crosses two light curtains which are across the direction of flight (figure 10), and which consist of a pair of lasers that sit at a known distance from one another ((499 ± 1) mm). These are targeted at photodiodes; the reason for their use is that when a projectile passes through a curtain the signal intensity from the photodiode will be diminished as a result of the laser beam being
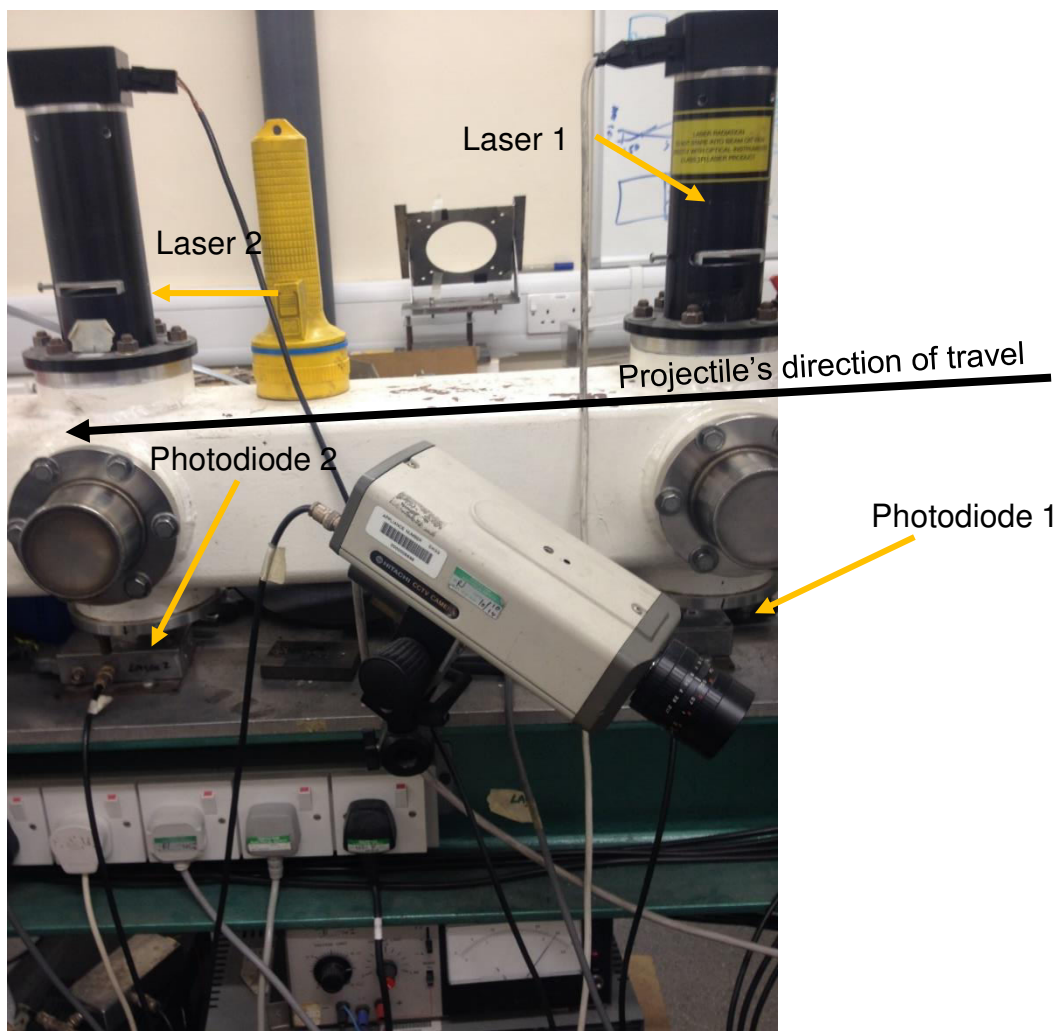

Figure 10: This illustrates the placement of the two light curtains that allow for a calculation of the velocity of the projectile. For clarity the direction of travel is also shown.

obscured. The first curtain will be blocked before the second most distant laser.

An oscilloscope displays a read-out of the signal amplitude of both individual photodiode and the time delay between the distortion event in the first laser and the second distortion event in the farthest laser can be shown by overlaying the two signals from the photodiode. Because the distance between the lasers is known and now the time-delay between each signal distortion event is also known the velocity of the projectile can be calculated. This calculation is typically accurate to better than 1% Confirmation of sabot passage through the light curtains is supplied via a CCTV camera connected to a monitor outside of the gun lab (figure 11) which is used by the operator to check the gun when the lab is evacuated pre-shot.
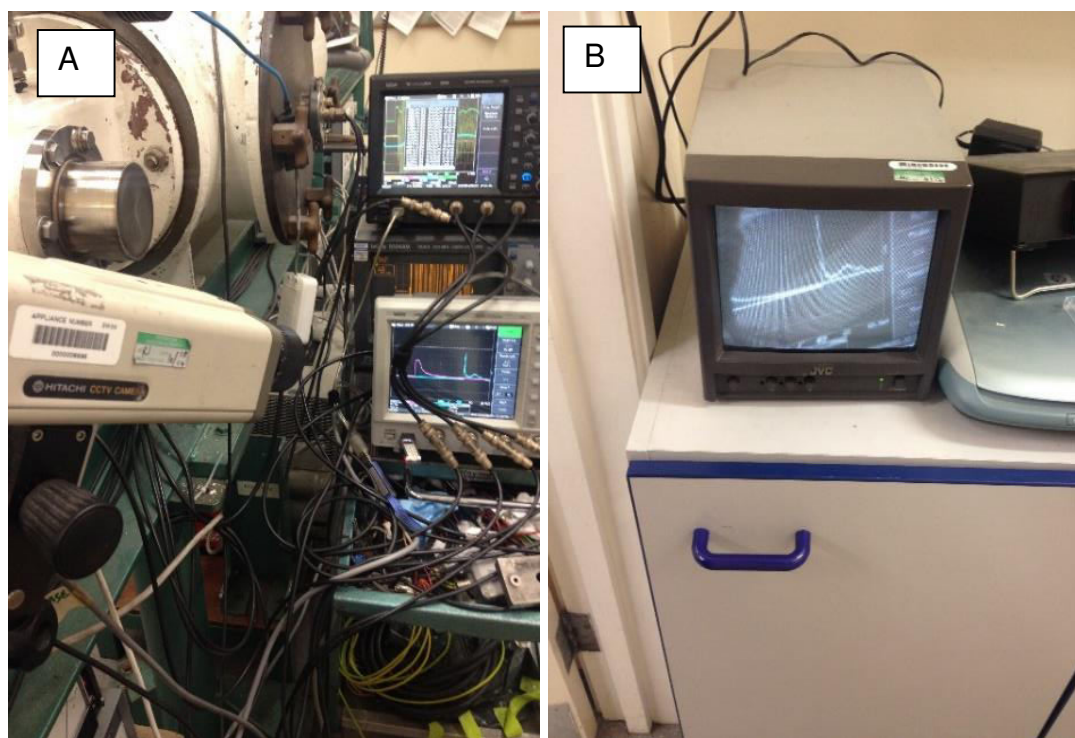

Figure 11: Image (A) shows the oscilloscope and the CCTV camera that provides for external monitoring. Image (B) shows the monitor through which a completed shot can be verified from outside the gun room.
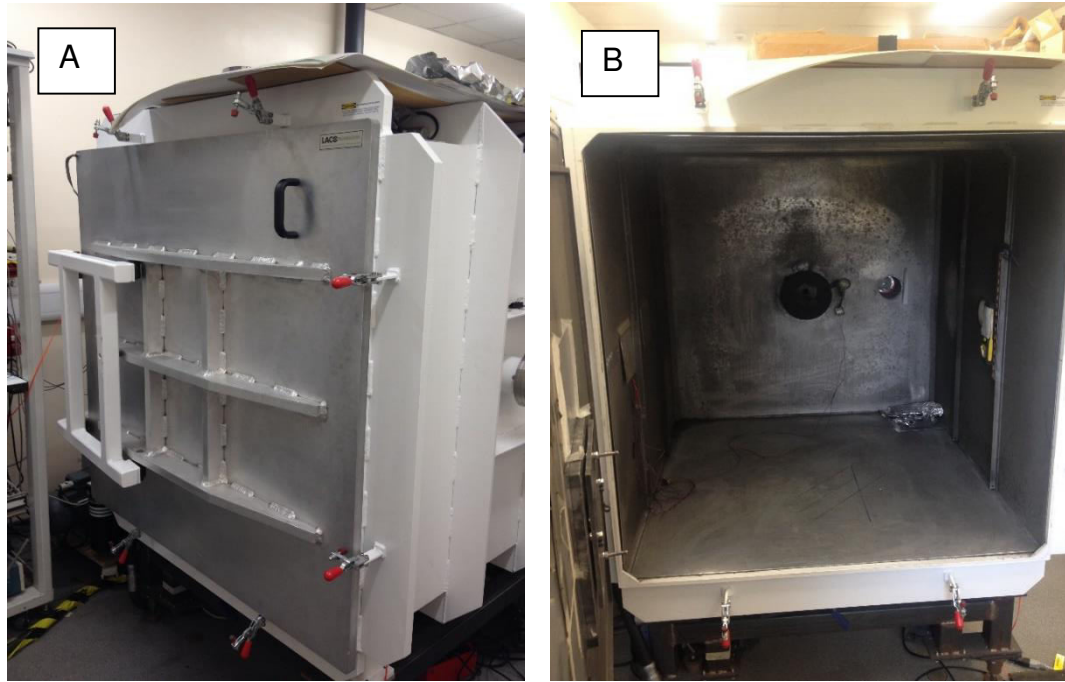
Figure 12: Two images of the target chamber. It has an internal volume of 1.2 m^3. Image A shows the blast chamber door in a closed position. Image B is looking into the blast chamber with the door open.

The last stage of projectile flight prior to impact is the entry into the target chamber. This is a 1.2 m^3 chamber and is again evacuated to approximately 0.5 mbar. The chamber has two circular windows which can be used to view impacts by setting up a camera (high speed and DSLR cameras have been used). Externally controlled lighting is also fitted to allow easier visualisation of impacts. See figures 12 and 13 for images of the target chamber.

Situated within the target chamber is the target itself, this can be mounted to the rear wall of the chamber (the door) or on a standalone positioning system (figure 13). To insure that the projectile hits its mark, the target is aligned by use of a laser that is positioned at the pump tube end of the gun, passes along the launch tube, through the blast tank and should line up with cross hairs which have been temporarily attached to the target.

After a shot the pressure in the pump tube is released using the vent valve and high pressure valve, allowing any remaining gas to vent out. The chamber vents are now opened so that a desired pressure is reached. Once the

chamber pressure nears the ambient pressure (identifiable by the sound of air that is rushing in slowing) a Nilfisk vacuum cleaner is turned on. This cleaner is fitted with a High Efficiency Particulate Air (HEPA) filter. The flush valve (a valve connected between the vacuum chamber and cleaner) is opened. The air flow is increased for approximately 10 minutes which allows for cleaning of any matter produced from an impact on the blast tank exit aperture and the target. The flush valve and vent valve is now closed and the cleaner turned off. The cleaner is vented out via the fume cupboard and through the building's fume extraction system.
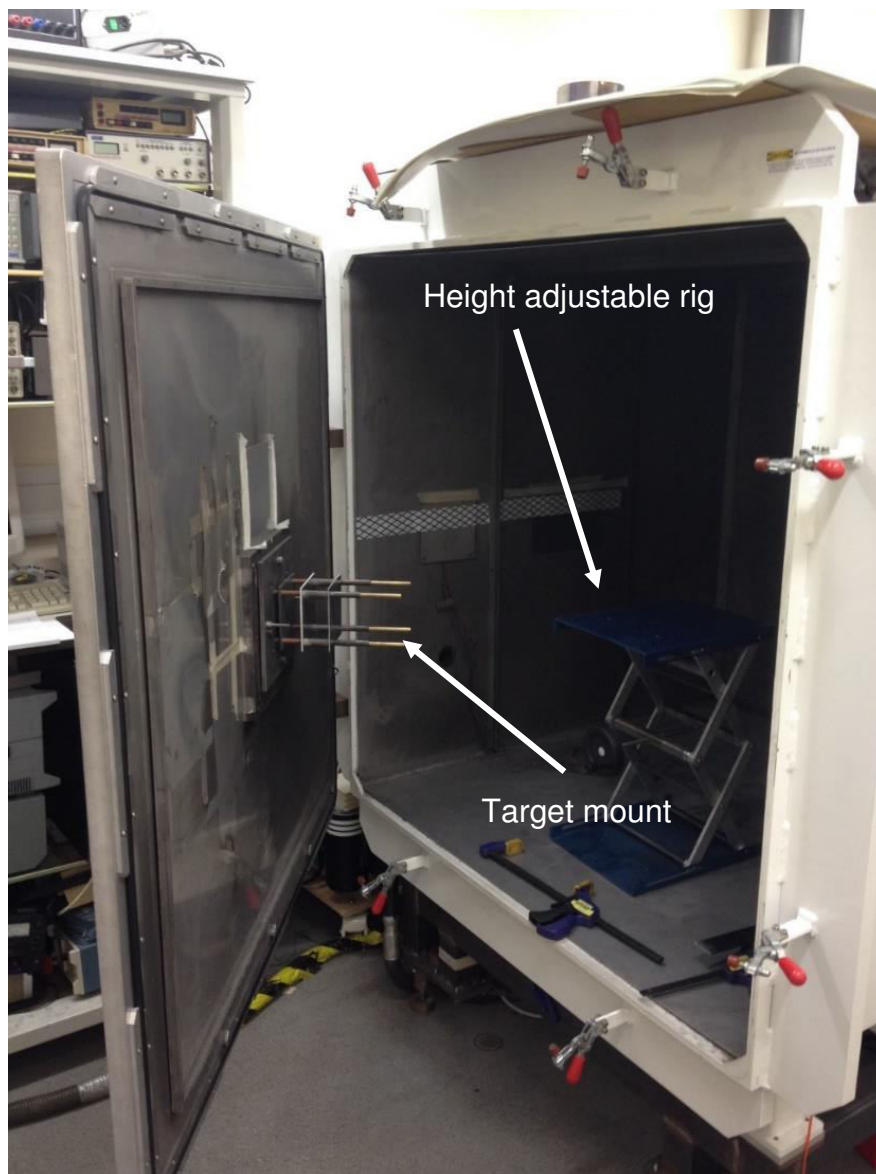

Figure 13: Two images of the target chamber. With a height adjustable rig and the target mounts associated with the door.

2.2. Project one: Survival of Fossils Under Extreme Shocks Induced by Hypervelocity Impacts.

Here we describe the experimental methods particular to this project. The fossils used were derived from diatoms, as such we shall begin with a descriptive introduction of them.

2.2.1. Diatoms.

Diatoms are phytoplankton; that is to say they are unicellular phototrophic organisms that can be found in oceanic and freshwater environments and even in damp soils. Diatoms have the capacity to develop a complex internal structure consisting of amorphous, hydrated silicon dioxide (silica) [51]. This internal structure is also known as a frustule. It is comprised of two valves or theca (these two units give rise to the diatom's name). One valve is larger than the other; analogous to a petri dish. When a diatom divides in its vegetative phase it produces two daughter cells (asexual binary fission) the parent valves are conserved, and a smaller valve (hypotheca) is synthesised for both individual daughter cells within each half of the parent's conserved frustule (epitheca). The consequence of this type of replication is that one daughter cell per generation will be reduced in size and thus a decrease in the mean size of the diatom population will be observed. Prevention of further size regression across the population occurs via sexual reproduction once the cells have hit an approximate size minima of 30 – 40% of the species maximum size [52]. The frustule is a very tough material that is synthesised following absorption of environmental silica using specialised silica transport proteins. They can largely be split into two morphological categories; the centric and pennate, which feature radial and bilateral symmetry [53]. Diatoms have an evolutionary lineage that stretches back hundreds of millions of years. Centric diatom fossils have been dated to approximately 180 million years [54]. The silica structure is species specific and is replicated with high fidelity through subsequent generations. This distinguishing feature allows for taxonomists to identify a particular diatom species despite the high number of distinct species (10^5-10^6) [51]. The diatomaceous frustules used here were sourced from diatomaceous soil.

2.2.2. Diatomaceous Soil.

This is a sedimentary rock comprised of the deposited silica skeletons of diatoms. This substrate has had many uses for instance; the patent for dynamite uses diatomaceous soil to absorb and stabilise nitro-glycerine; as a pool filter; and as an insecticide. The soil used here was sieved so that the size of the particles did not exceed 180 μm. Initial tests suggested that this size selection yielded a greater volume of intact fossils pre-shot. Figure 14 shows the diatomaceous soil container and the soil itself.

Figure 14: Diatomaceous soil is readily available. The container (left) and the soil itself (right) are shown.

2.2.3. Modifications to the gun.

The experimental protocol requires the use of a rigid plug of diatomaceous soil frozen in water which simulates fossils trapped in rock. To achieve this the sabot containing the soil was frozen. Due to the frozen nature of the sabot and contained materials the launch tube also had to be kept at a low temperature. This was achieved by cooling the barrel (pre-shot) in a freezer (stored in a chest freezer at -120°C). When the shot was to be attempted, the barrel was placed in the gun inside an insulated box. This kept the sabot cold enough so that it was still frozen when the gun was fired. Figure 15 is a schematic of the gun with modifications for this experimental programme.
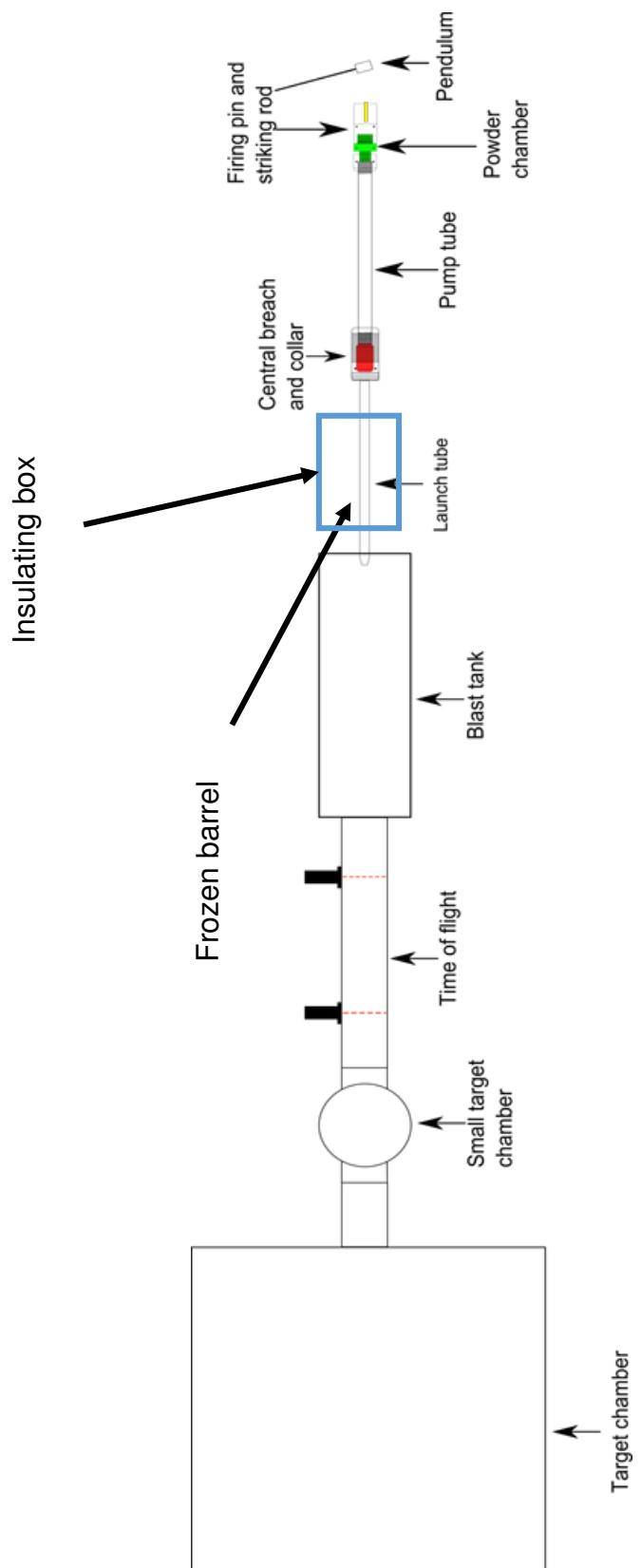
Figure 15: Schematic of the light gas with the frozen barrel configuration highlighted.

The scheme to fire frozen sabots was developed just prior to the initiation of this project. The process of freezing sabots enables new avenues of research such as this one.

2.2.4. Target.

This consists of; a modular structure comprised of a base plate, target holder and splash box; the target itself that the projectile will impact; and a height adjustable mount and stabilising weight. The target includes two plastic bags that were filled with 150 ml of reverse osmosis water in each bag. See figure 16 for images of the bags used in this experimental set up. These were placed upon a capture tray to contain the impact splash and this sat on an adjustable platform in order to set the height of the target within the target chamber. The platform with the target in it stands on the floor of the target chamber and is positioned so that the target centre is in the projectile's line of flight.
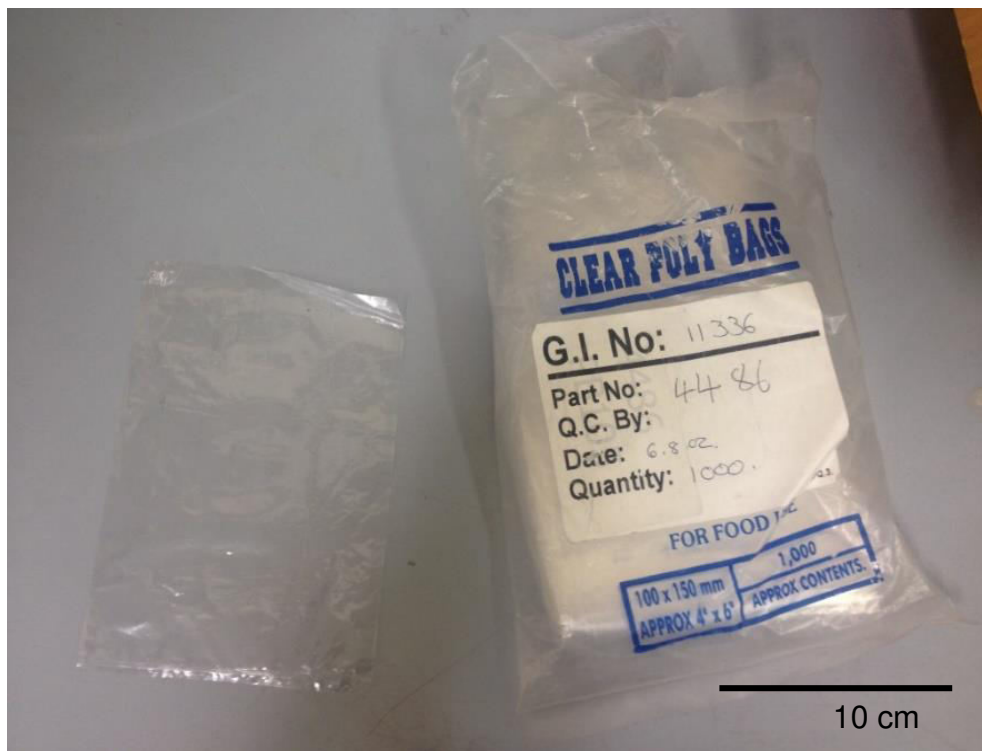
Figure 16: Images showing one example of the plastic bag used for the target. This is filled with 150 ml of reverse osmosis water and two bags are used in the experiments.

2.2.5. Target Holder

The target holder sits atop the base plate. It has three components, a fixed structure, a protective steel back plate and an adjustable structure that features an aperture to allow for the projectile to impact the target. Refer to figure 17 for a labelled image of the target holder.

Figure 17: Image showing the components of the target holder including the base plate. A face-on view is shown here. The frame has been bent as a result of prior impacts.

The metal in the target holder in figure 17 has been bent and distorted by use. The horizontal metal ribs which hold the front of the water target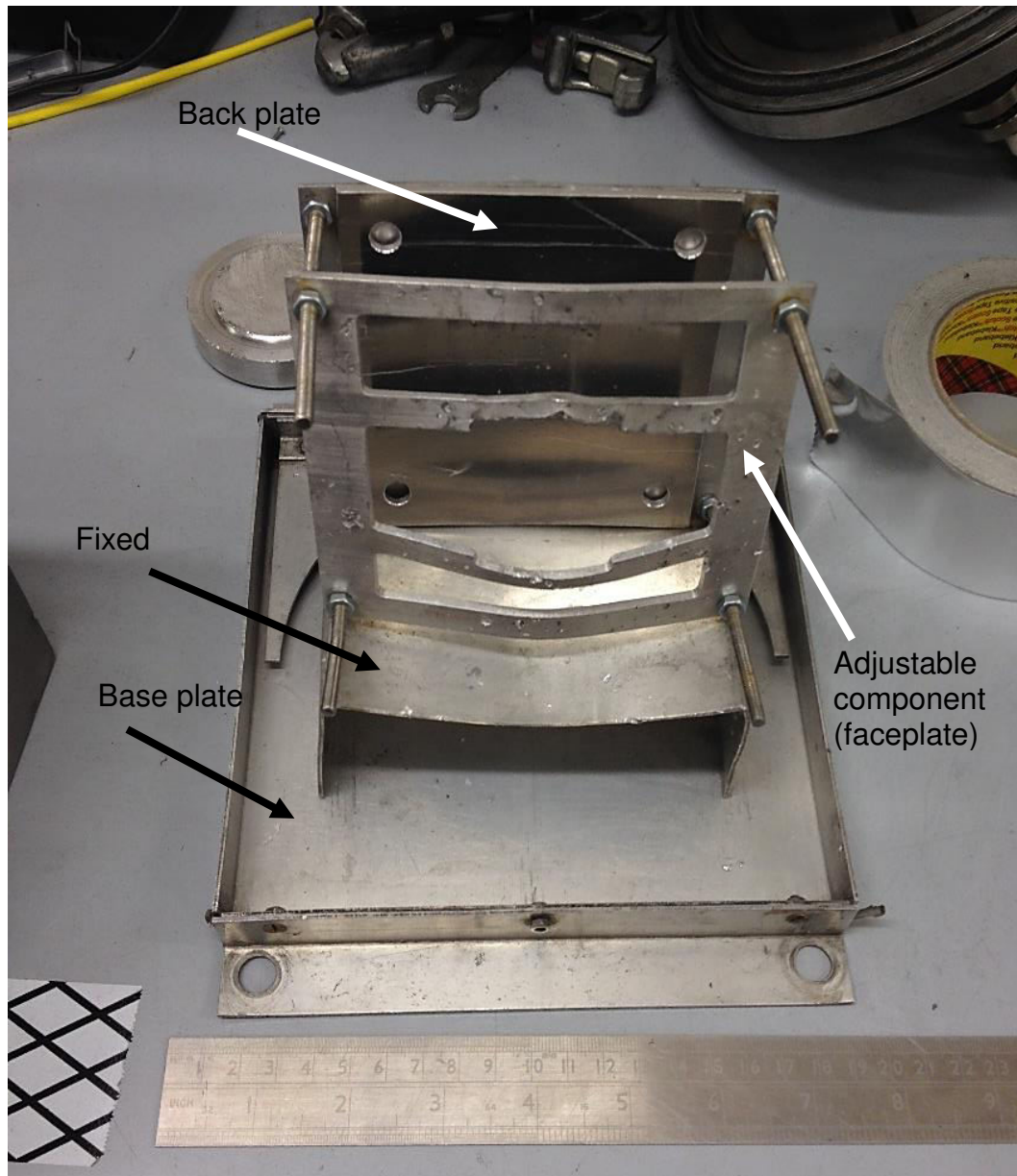 in place, have bulged outwards due to the pressure in the water following an impact. During an experiment the target holder is covered with a metal containment box (figure 18). This fits over the target holder and contains the water that has escaped from the bags during an impact. There is a small hole in the containment box (~2.5 cm in diameter) to allow entry of the projectile. For an image of the target featuring the target holder and water bags within the target chamber (see fig 19).

2.5 cm
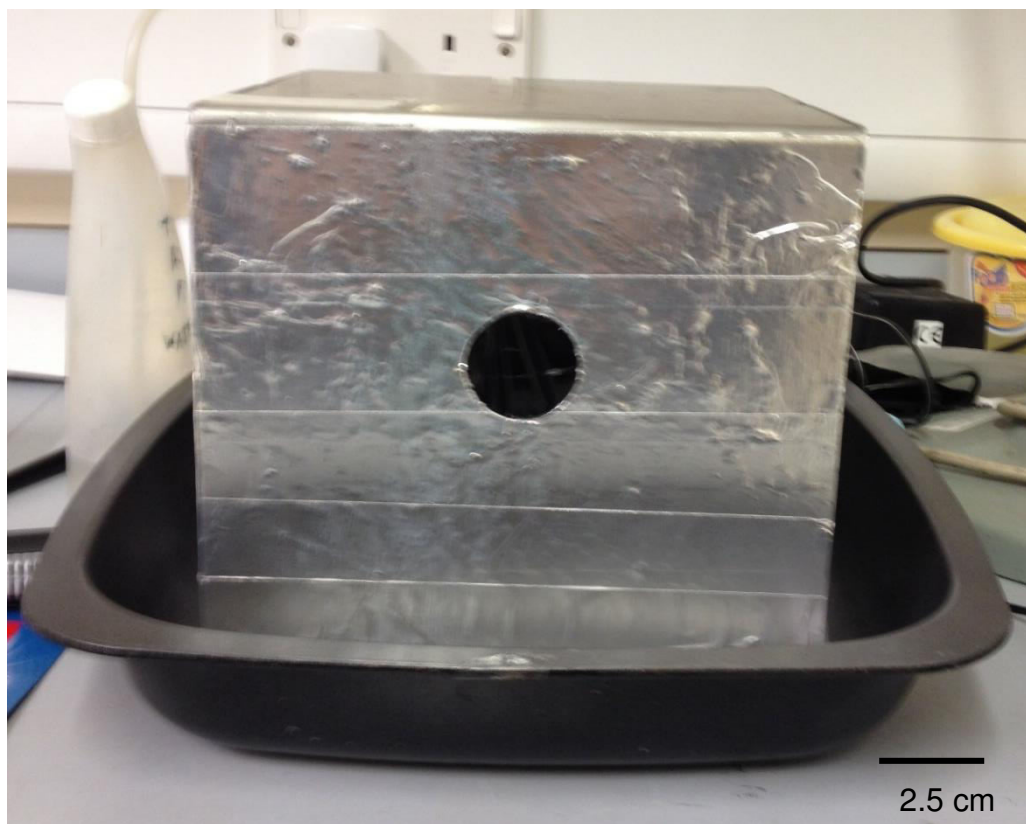
Figure 18: An image of the containment box that covers the target holder. Also pictured is the tray that the target sits within, which also acts to contain the water following an impact.
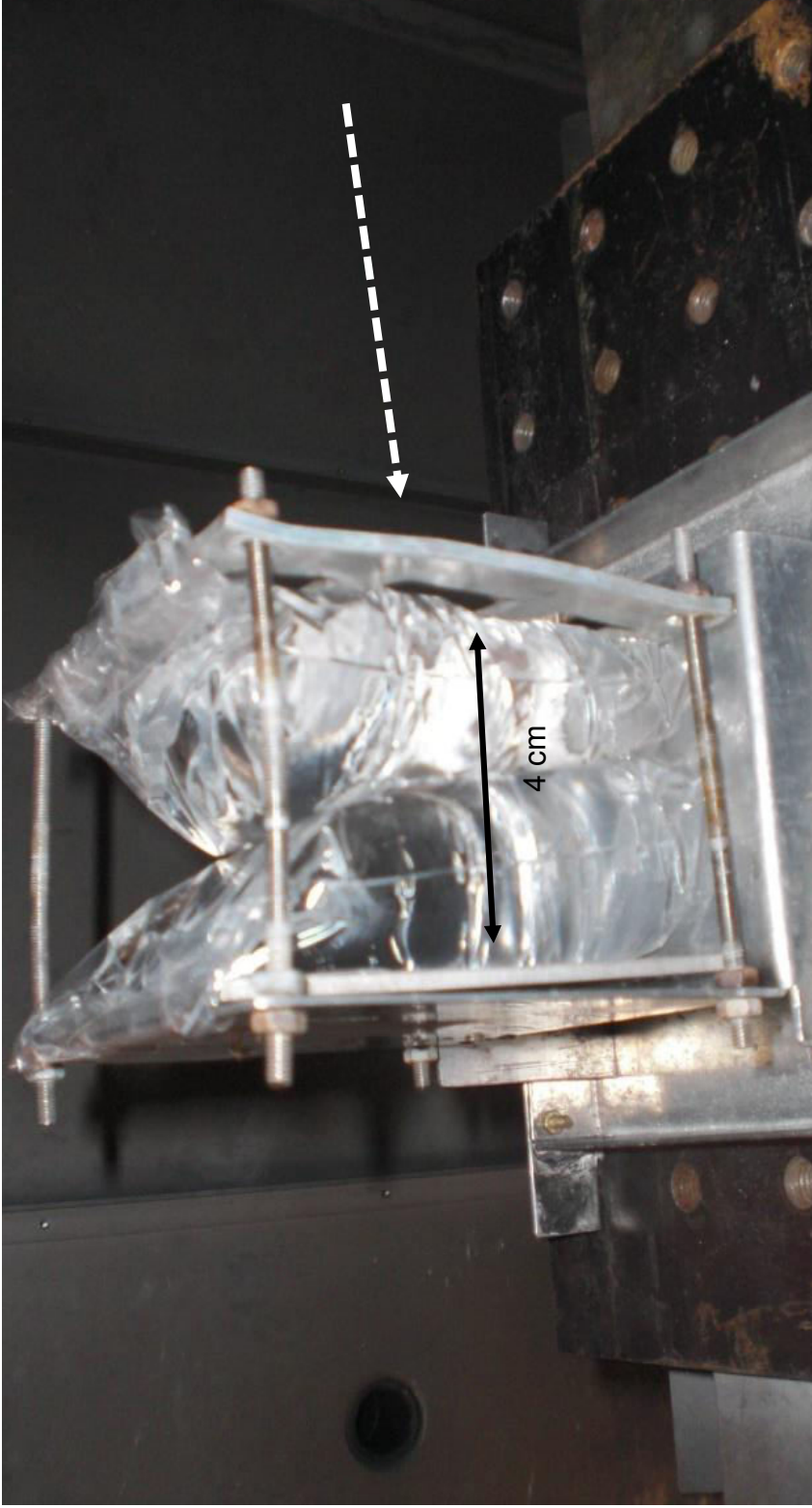
Figure 19: Image showing the target within the target chamber (side view), this would be covered with an impact-splash containing box in an actual shot. This set-up is fixed to a rigid platform that is raised using an adjustable platform to the desired height. An alternate base plate is shown. The dashed arrow represents the projectile's trajectory.

2.2.6. Projectile.

The projectile consists of a 4.3 mm long cylindrical sabot that is 4.5 mm in diameter. This features a central well that contains the substrate of interest. In the shots here, this well is 2.5 mm in diameter and 2.5mm in depth. Within this well 3 µg of diatomaceous soil is added. Water was then allowed to disperse through the substrate and this was then frozen. Figure 20 is a top down view of a solid sabot containing frozen diatomaceous soil.

Figure 20: Top down view of the nylon sabot showing the well containing the diatomaceous soil. This well is 2.55 mm in diameter and 2.5 mm in depth.

2.2.7. Post-impact.

Following impacts at the desired speeds (1-5 km s^{-1} as well as a low speed shot at <1 km s^{-1}) the water from the target was filtered through Whatman filter paper (figure 21).

This filtering process collects any particulate matter that may be present following the impact. To ensure for a rigorous collection of material after a shot the target, target holder, splash box and splash tray were all rinsed thoroughly with reverse osmosis water which was then also poured through the filter paper. The paper was then dried and the filtrate ready for imaging.

As a test of the efficacy of the filtering process, a volume of diatomaceous soil comparable with the amount added to a projectile was suspended in reverse osmosis water. This was then filtered, the paper dried and then imaged. Figure 22 shows fossil fragments filtered from the un-shot control. The filtering system had thus been shown as an effective method of retaining diatom fossils.
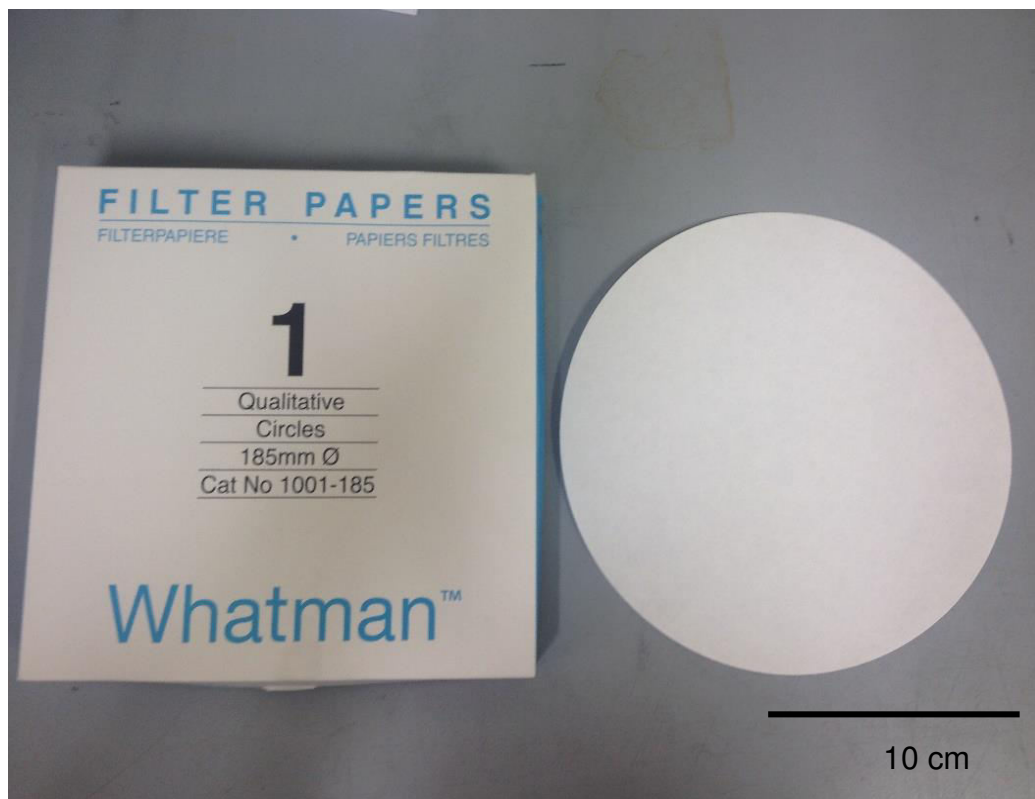

Figure 21: Image showing the filter paper used for the collection of particulate matter.
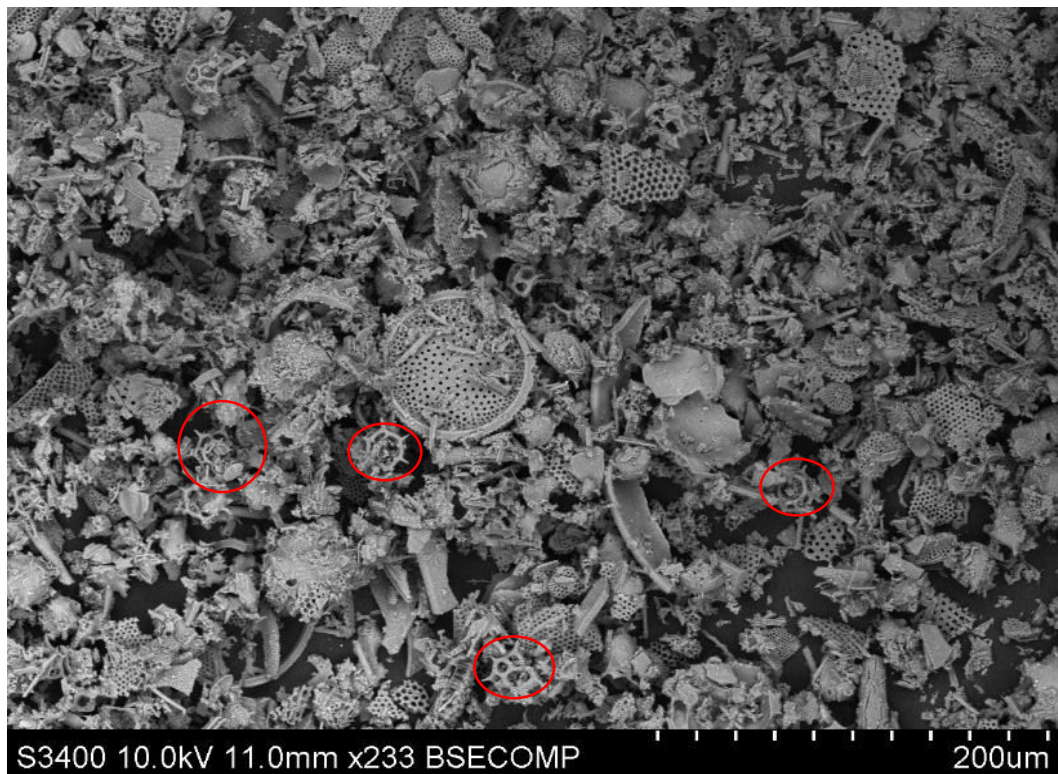
Figure 22: Image showing successful filtration of the diatomaceous soil from a volume of water, taken on a Hitachi S3400N scanning electron microscope. Also present are examples of non-diatomic organisms known as a sillicoflagellates. Some examples of the sillicoflagellate *Dictyocha speculum* are circled in red. These organisms also produce a silica skeleton.

2.2.7.1. Imaging.

The hardware used for this component of the study was a Hitachi S3400N scanning electron microscope (SEM) (figure 23). The SEM produces images by focussing a beam of electrons onto a sample, these electron-sample interactions are detected as they generate readable signals. Two modes (secondary electron and back scatter electron) were primarily used. Secondary electron mode relies on electrons that are emitted by atoms in the sample following interaction with the electron beam, an example of inelastic scattering. Back scatter electron mode relies on electrons that are reflected as a result of electron-sample interactions, an example of elastic scattering. In the analysis here, the filtrate is transferred from the filter paper onto Agar Scientific 25 mm adhesive carbon tabs, by pressing the adhesive tabs onto

the filter paper. The adhesive tabs are attached to an aluminium SEM stub. The specimen mount's height is checked against a standard gauge before being entered into the loading platform of the SEM. Because of the material being examined it wasn't necessary to coat the samples through carbon deposition.

Morphological distinctness was one tool used to identify the presence of diatom fossils. Another tool that was used was the elemental mapping function on the SEM; due to their silica construction a silica peak would be seen. This elemental analysis was provided by an energy dispersive X-ray spectroscopy system (an Oxford Instruments Xmax-80 silicon drift detector and Inca software). This system was calibrated using a cobalt standard. For this study the accelerating voltage was 20.0 kV with a typical emission current of 84 µA. The working distance was set to 10 mm, this is the distance between the specimen and the objective lens.
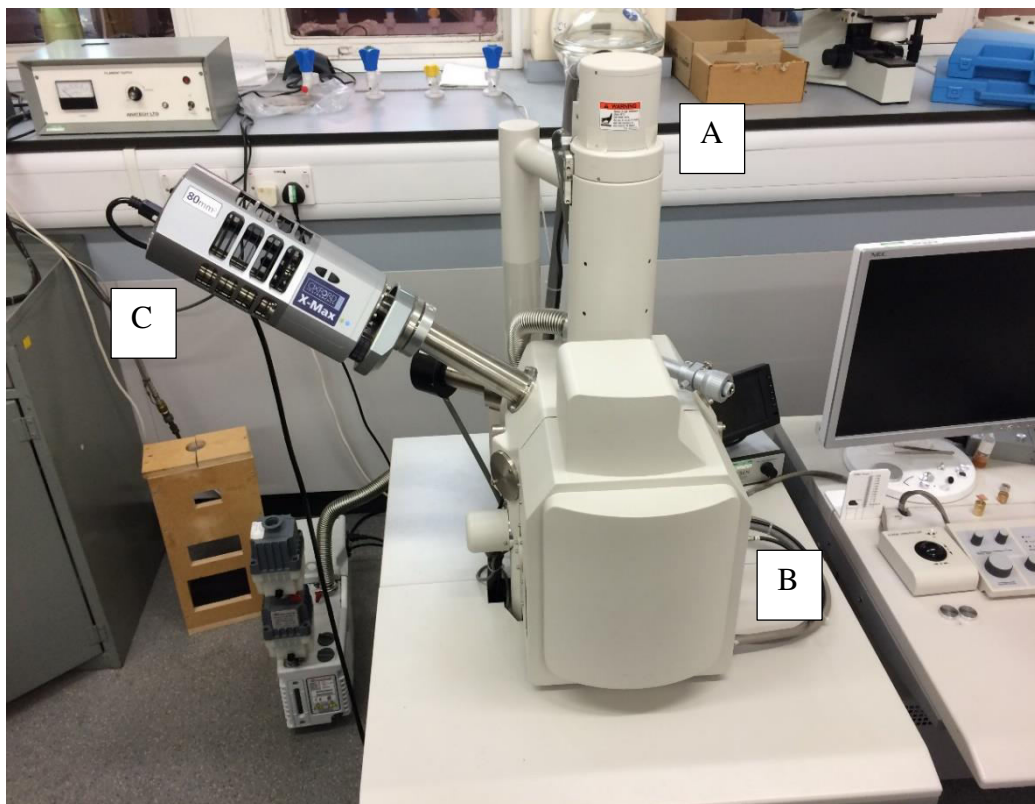

Figure 23: Image of the Scanning Electron Microscope used in this study. (A) highlights the location of the tungsten hairpin electron gun. (B) is the vacuum chamber containing the specimen stage. While (C) is the silicon drift detector for elemental analysis.

Overnight scanning maps were set up, for examination of the filtered samples on the specimen mounts. These maps were designed to scan a quadrant of the specimen at high resolution which would then be manually investigated for fossil fragments and the fragment count logged. Digital callipers would measure the size of the individual fragments.

2.2.8. Control sample.

This was a more robust control than the filtration test discussed earlier. This featured a sabot that included the previously described addition of 3 μg of diatomaceous soil and water. This was then frozen. The frozen projectile containing the diatoms was, instead of being loaded into the gun, placed into a volume of reverse osmosis water analogous to the volume of water used in the target. This water was then filtered using the previously described method. Fossils were recovered in this test and the SEM analysis of the control sample can be found in chapter three.

2.3. Project two: Prospective liquid core sabot designs.

In a second shot programme the protocol required a sabot containing liquid instead of ice. This liquid was held in place with a lid on the sabot. However as described in the description of the light-gas gun, components of the gun are evacuated to prevent drag on the projectile that would lead to a decreased projectile velocity. Issues were observed to arise when using a sabot with a liquid (specifically water) core. Initially at 50 mbar of pressure, the lid was found to detach when using a sabot with a simple acetate lid, glued in place. This allowed for the contents to evaporate. As a result new sabot designs were configured.

The brief was to suggest designs that allowed for:

- The sabot lids to be held securely enough to preclude a failure in the seal and thus an escape of the contents due to evaporation.
- The provision of ready access to the liquid core of the sabot post-shot. Transmission of items from the sabot into the target for retrieval can also be included here.

The sabots would be tested at low pressures in order to investigate which ones were robust enough to retain their liquid core while also fulfilling the other items in the brief. The sabots in the test experiments would be held in the target chamber, this would then be evacuated to 100 mbar at first and this pressure would be held for 5 minutes, following this a subsequent 50 mbar test would be carried out on any sabots that stood up to the 100 mbar test. This time frame was chosen as a typical minimum time span that a sabot loaded in to the gun would experience. The sabots could be monitored using the windows of the target chamber and food colouring was added to the liquid to make visualisation more apparent. Once this is completed the sabots were removed and examined for water retention.

There were three potential designs tested, all three used the Loctite 495 adhesive from Henkel (see figure 24). This is a quick setting low viscosity adhesive that can be used on a number of substrates (rubber, plastics and metals); ideal for this project.

Figure 24: An image of the adhesive used on the various sabot designs to secure the lids.

1. Sabot with an acetate cap:

The first design implemented an unmodified sabot (see previous description) with a disc of acetate that was placed on top of the sabot once the liquid core has been set up. The acetate lid was secured into place with an adhesive beading around the outer rim. When the adhesive had dried any excess was filed back. See figure 25 for an example of a sabot with an acetate lid.
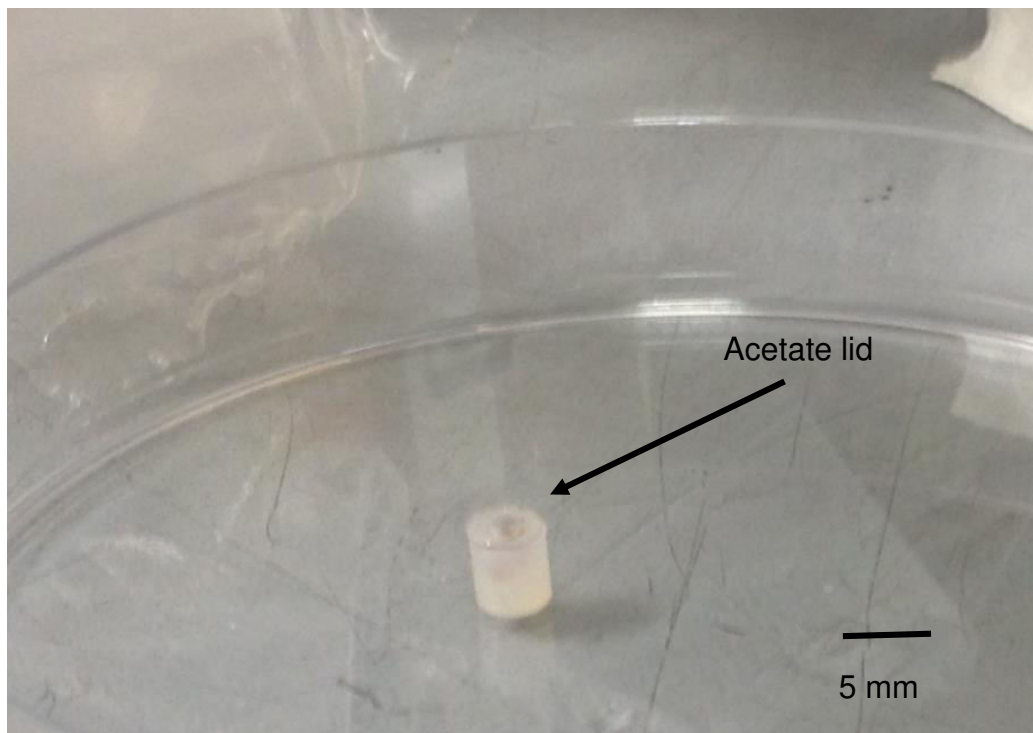
Figure 25: This sabot contains a liquid water core and an external acetate lid.

2. Sabot with a rubber seal:

The second design used an unmodified sabot (see previous description) with a disc of ~1 mm thick rubber that was glued on top of the sabot. This configuration allows for injection of the liquid through the rubber cap. First an adhesive beading was run around the rim of the sabot. In the case of the injected liquid variant, the design could be placed bottom side up on a loosely cut rubber cap (figure 26). This cap was then cut around the circumference of the sabot.

This injection variant will be compared with a sabot that has been filled and then sealed, in the results section. See figure 27 for an image of the rubber sealed sabot design, once filled with coloured liquid.

5 mm

Figure 26: Image showing the upturned sabot on the loose cut rubber sheet. The excess rubber is then trimmed to fit.

5 mm
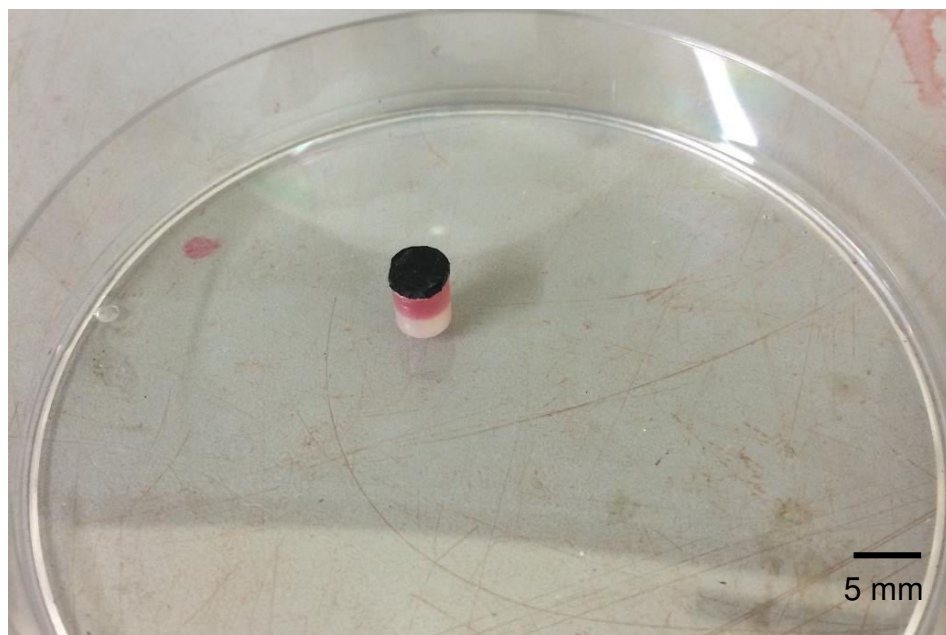
Figure 27: Image showing the sabot featured the rubber seal / lid. This particular example was filled with coloured water with a pipette.
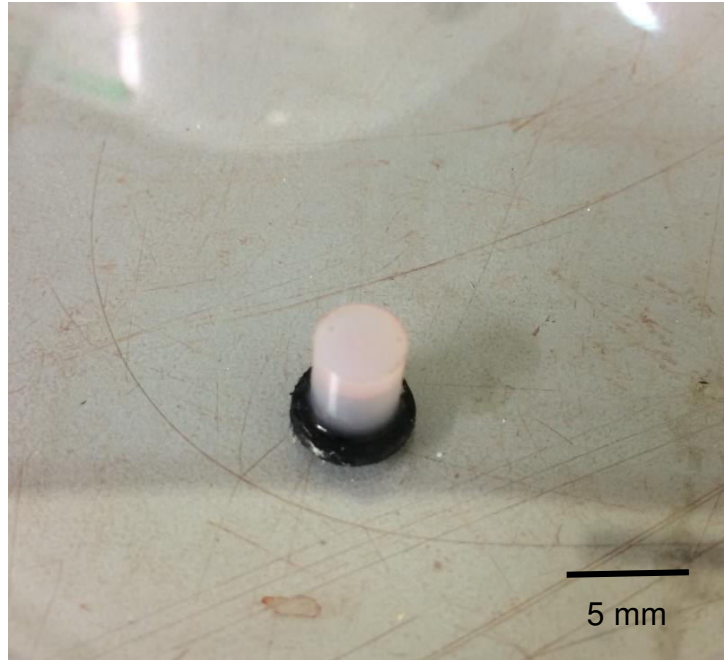
3. Sabot with an inset acetate lid:

This design required modification of the sabot through counter-boring. This involved the formation of a larger flat bottomed hole that is constructed from the upper portion of the sabot well to form two coaxial holes. The floor of the enlarged hole was where the acetate lid resides, while the lower hole contains the liquid. A drop of adhesive was added onto the lid which was allowed to disperse forming a fine film that held the lid securely into the well. For a cross-sectional schematic of the sabot before and after counter-boring see figure 28. For images of the counter-bored sabot with liquid see figure 29.

Figure 28: (A) Cross-sectional illustration of an unmodified nylon sabot with the central well featured (2.5 mm in depth). (B) Cross-sectional illustration of the counter-bored sabot featuring the acetate lid sitting on shoulders of the lower well. The lower well will contain the liquid (now 2 mm in depth). A drop of adhesive is added and allowed to disperse as a thin film across the lid.

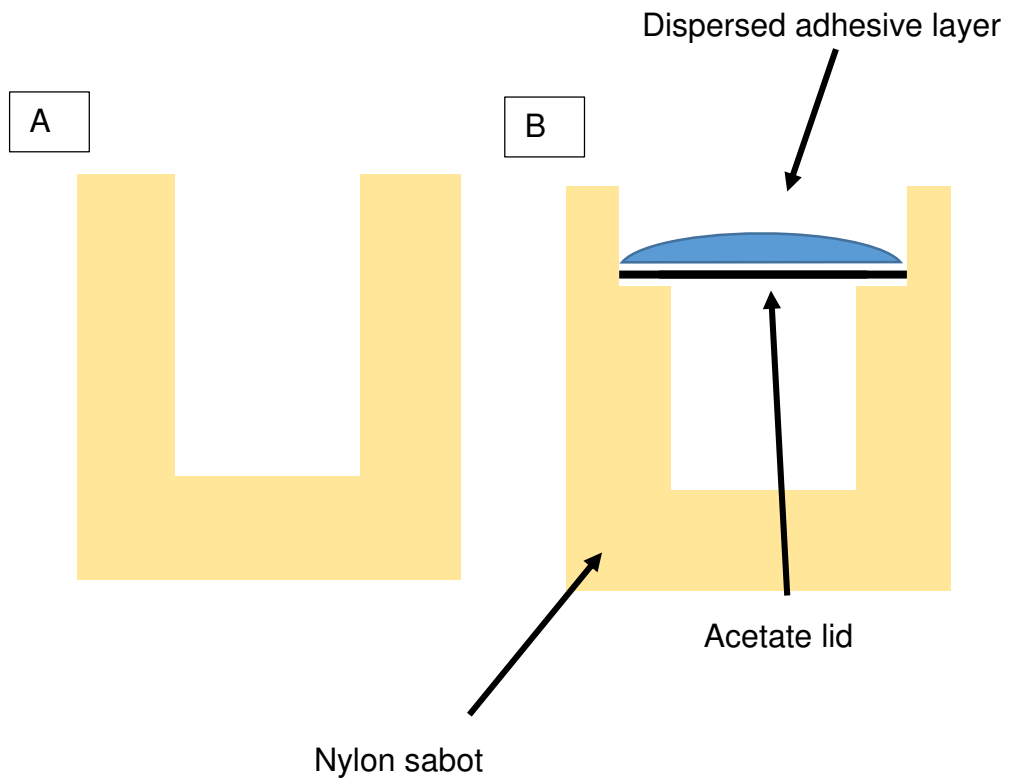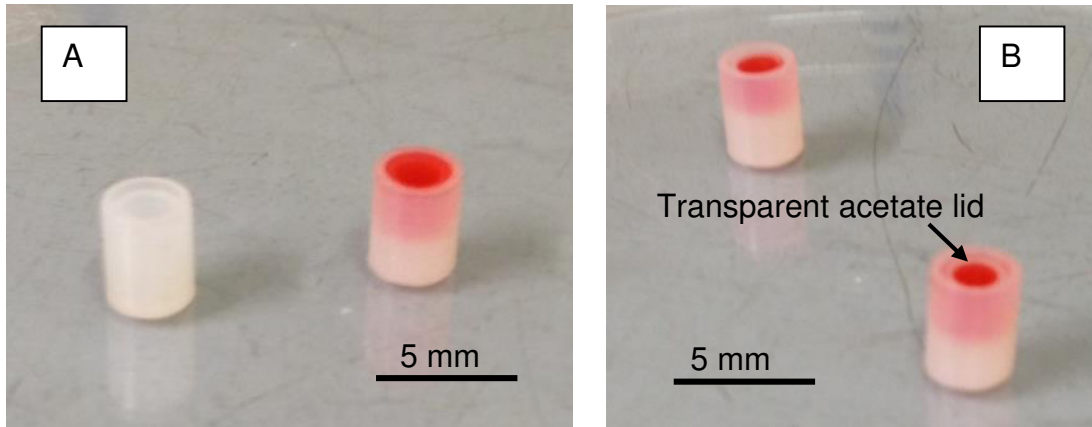Figure 29: Image A illustrates the modified counter-bored sabot empty and liquid-filled (with added red colouring). Image B shows how the transparent acetate lid sits on the counter-bored shoulder.

2.3.1. Light-gas gun tests with new sabot design.

If the pressure tests yielded successful results, the successful transmission of sabot contents into the target could then be investigated. This was achieved by simply adding a coloured glass bead (2 mm in diameter) into the well of a sabot (figure 30) after the sabot had been filled with water. The sabot was processed in the manner described in the prospective designs. Survival of the glass bead was used as a proxy for successful transfer of the sabot contents into the target. This was then further developed by using a liquid core projectile doped with diatomaceous soil, a material discussed previously here. This substrate is easily dispersible in water and would take this from a developmental project to an operational that should be used in future experiments. Detection of fragments would follow the description in 2.2.7.

The tests of this modified sabot were to form the final part of this thesis. A modified target was also used. This target was comprised of the splash containment box used in the diatom fossil impact project which was filled with water. This is an alternative to the plastic bag method seen previously. The entry hole to the target was sealed with a plastic bag. A waterproof plastic lining was laid out within the target chamber to retain any water from the impact, this also served as a platform for the adjustable rig to sit. See figure 31 for how this was constructed within the target chamber.
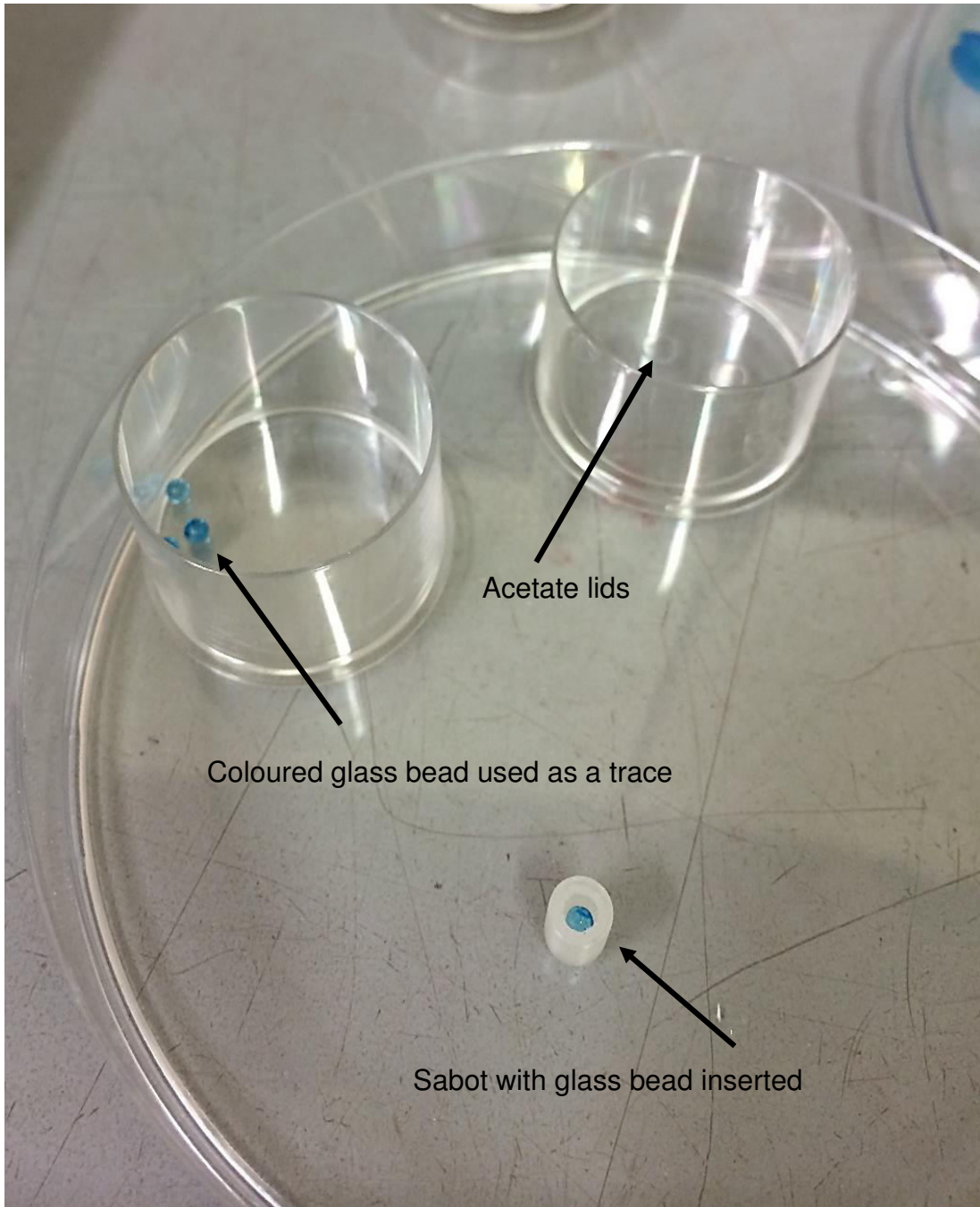
Figure 30: An image a sabot containing the coloured glass bead (2mm in diameter) that will be used a tracer; confirming the transmission of the sabot's contents into the target.
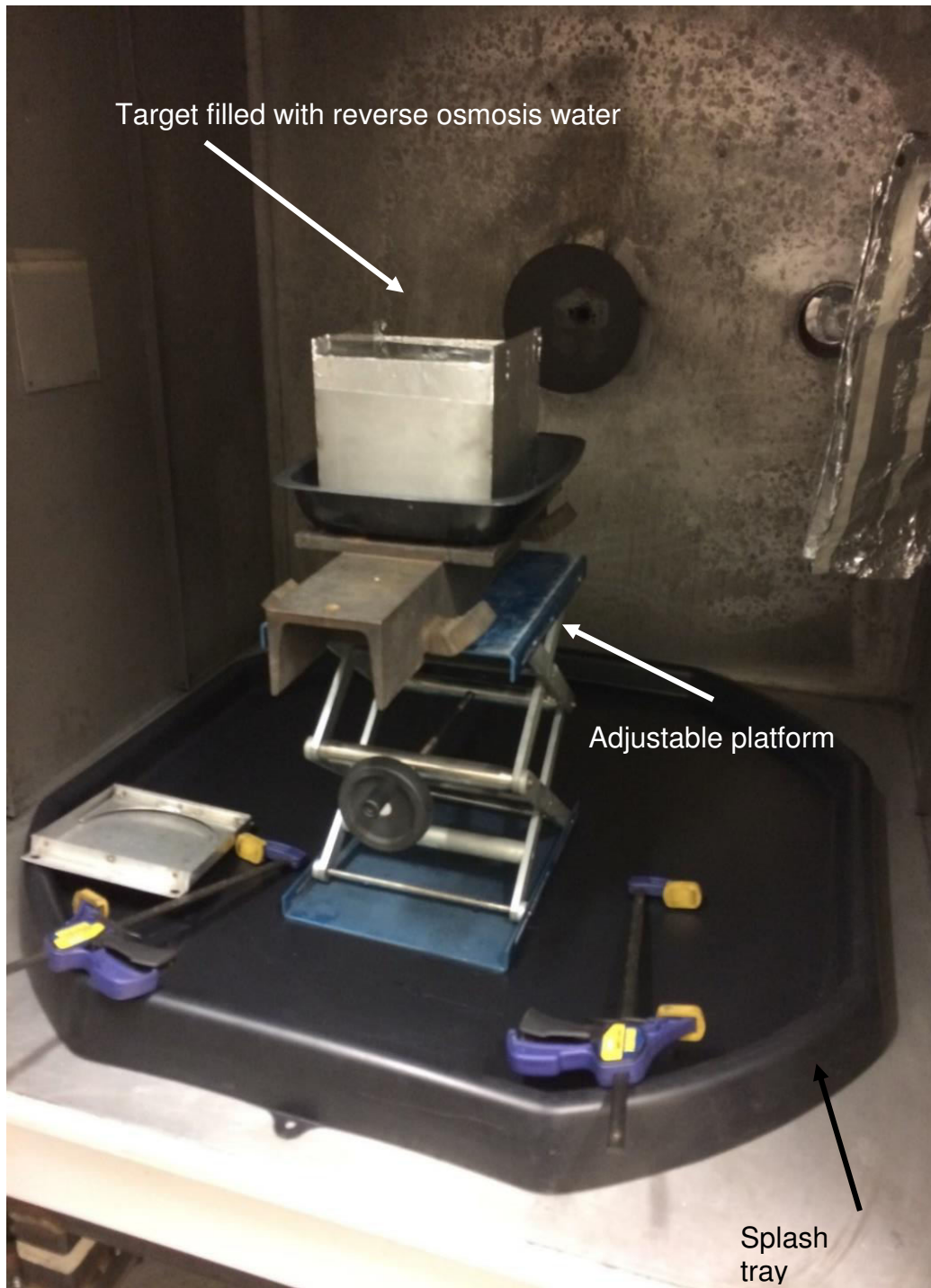
Figure 31: An image showing the target to be used in the glass bead recovery shot with major components labelled.

2.4 Modelling shock pressure using the Planar Impact Approximation.

Investigating the relationship between impact speeds and shock pressure is of great interest in meteorite impact simulations and has aided in elucidating the solar system's impact history. Figure 32 illustrates how a shock moves through a substrate. This can be achieved by applying the Planar Impact Approximation (PIA) [55]. While the propagation of shock waves occur through the impactor and the target, the PIA finds peak shock pressure just behind the contact plane of two infinitely-wide plates of representative material, impacting face-on. This is thus a one dimensional approximation of shock, ignoring the topography of the impactor and target but also the microscale composition of these two substrates.
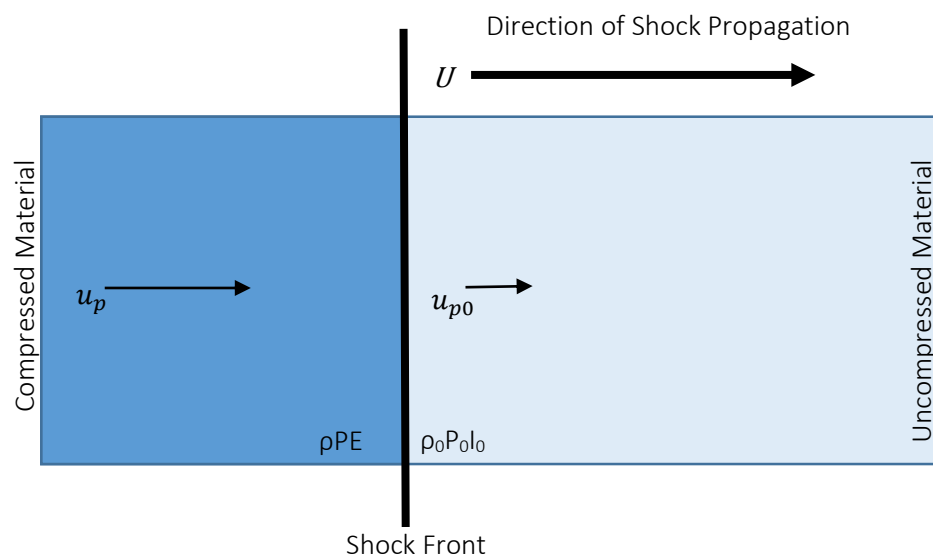
Figure 32: Schematic diagram, illustrating the propagation of shock through a material. The quantities of density (ρ), pressure (P) and internal energy (I) are seen in their compressed state (left/dark blue) and at rest (right/light blue with subscript 0). With U, the shockwave speed, and u_p, the particle velocity. The material compression ceases once the propagating shock wave reaches the free-surface boundary. Adapted from [55].

The PIA allows for the calculation of the pressure behind the shock front providing a solution to equations (3) and (4). These three equations are the Hugoniot equations for the conservation of mass (3.1), momentum (3.2) and energy (3.3). Where, P and P_0 are the pressures behind and in front of the shock respectively. I, the internal energy, U is the shockwave speed, and u_p (m s^{-1}) is the particle velocity. ρ_0 is the uncompressed density (kg m^{-3}) of the substrate.

$$\rho(U - u_p) = \rho_0 U, \tag{3.1}$$

$$P - P_0 = \rho_0 u_p U, \tag{3.2}$$

$$I - I_0 = 0.5(P + P_0)(1/\rho_0 - 1/\rho), \tag{3.3}$$

The Hugoniot equations with their five unknowns can be completed by the linear shock wave relationship (4); a linear relationship between shock and particle velocity.

The linear shock wave equation is:

$$U = C + S u_p, \tag{4}$$

where C (m s^{-1}) and S are empirically defined material-specific constants (established through dedicated flyer plate experiments). Equation (4) does not account for any other thermodynamic parameters (e.g. entropy or temperature) so as a result is not considered a full equation of state. However it is applicable to many materials that display, empirically, a linear relationship between shock and particle velocity.

The particle velocity of the target u_t (subscripts t and i reference target and impactor respectively), can be expressed in terms of the quadratic formula:

$$u_t = \frac{-b \pm \sqrt{b^2 - 4ac}}{2a}. \tag{5}$$

The terms of the quadratic formula are defined thus:

$$a = (\rho_{0t}S_t) - (\rho_{0i}S_i), \tag{5.1}$$

$$b = (\rho_{0t}C_t) + (\rho_{0i}C_i) + (2\rho_{0i}S_i v_i), \tag{5.2}$$

$$c = -(\rho_{0i}v_i)(C_i + S_i v_i), \tag{5.3}$$

where v_i is the impactor velocity respectively.

The pressure behind the shock can now be expressed as (6) if we consider P_0 to be negligible:

$$P = \rho_{0i}u_i(C_i + S_i u_i). \tag{6}$$

Thus, as long as the C and S values are known we can find estimates of the peak shock pressure, in a material, in an impact event. The pressure in the target and the impactor is the same.

A special case should be noted for instances where the projectile and target are comprised of the same material. This is as a result of the zero in the denominator (4.1) in the quadratic expression of particle velocity (4) leading to an undefined result. This special case can be solved through implementation of equation (7):

$$P = \left(\frac{\rho_t v_i}{2}\right)\left(C_i + \left[\frac{S_t v_i}{2}\right]\right). \tag{7}$$

2.5. Summary.

This chapter has acted as a means to describe the experimental and analytical methods to be utilised within this project. The core component of this section is the light-gas gun which is the focal point of the proposed studies. Other apparatus have also been described in order to provide an accessible overview of this particular project. Two projects have been described within this chapter. Project one the experimental examination of fossils under extreme shocks induced by hypervelocity impacts. While project two

demonstrates the development and operationalising of a new sabot design, that should be used by future experimenters requiring the firing of liquid in the light gas gun.

CHAPTER THREE:

RESULTS OF PROJECT ONE.

This chapter will provide the data accumulated through the process of the experimental methods outlined in the previous chapter. The significance of these results will also be discussed herein.

3.1. An overview of diatomaceous soil shots into water.

Table 2 describes all of the shots performed with the light-gas gun using diatomaceous soil filled sabots and a target comprised of water bags for recovery of any sediment. The attempted velocities were chosen with reference to the calculated lunar impact velocities seen in Armstrong (2010) [27]. This places the velocity ranges between 1 and 5 km s^{-1}. To further investigate the effect of impact induced shocks on these items a low speed shot, <1 km s^{-1}, and higher speed shots were attempted at 6 and 7 km s^{-1}. Table 2 lists all shots all attempted, including ones which failed for reasons to be discussed. Note that when the project velocity is marked as N/A this refers to the unsuccessful attainment of a shot velocity (i.e. no velocity available from the oscilloscope signal). This usually arose from a failure of the oscilloscope to trigger at the right time. On top of this where possible the malfunctions were investigated and have been described. Shot events that involved experimental malfunctions in some way have been flagged red in table 2.

Table 2: A summary of all light-gas gun shots of frozen diatomaceous soil filled sabots into water. See main text for a discussion of the failed shots. Please note the numbers in the malfunctions / faults column do not represent the quantity of malfunctions in the given shot. These faults are labelled numerically to make it clear what fault is being referenced in the main text.

Velocity Attempted (km s^{-1})	Projectile Contents	Gas	Impact Velocity Achieved (km s^{-1})	Malfunctions / Faults
<1.00	Frozen diatoms	N$_2$	0.388	
1	"	Kr	1.26	
2	"	N$_2$	2.05	
3	"	He	3.14	
4	"	He	4.1	
5	"	H$_2$	5.01	1
5	"	H$_2$	5.11	
6	"	H$_2$	N/A	2
7	"	H$_2$	6.47	3
7	"	H$_2$	6.97	4

Fault 1 in table 2 represents a storage error following filtration. The sample had been stored prior to SEM map analysis with a small vial containing an un-shot sample of diatoms. This resulted in contamination of the shot sample. This meant that another shot attempt for 5 km s^{-1} was estimated as the best course of action and thus 5.11 km s^{-1} will be the velocity featured in the results to be analysed.

Fault 2 occurred during an attempt at a higher speed, 6 km s^{-1}. This was unsuccessful as a result of moisture underneath the burst disc. The moisture was a consequence of the frozen barrel configuration. As a result the burst disc slipped and gas from the pump tube forced the sabot along the gun into the target at low speed (the light gate had not been configured as this occurred early in the set up so no speed was recorded).

Fault 3 references a malfunction that arose while attempting a velocity of 7 km s^{-1}. This was pushing the boundaries of both the gun in a cold configuration but also of the frozen sabot used in this experimental series. Upon investigation it was apparent that the sabot had deflected somewhere in the blast tank before reaching target. This may have been a result of abnormalities in the freezing process that led to in-flight instability. This would promote an aberrant flight path. A speed was recorded for this shot (6.47 km s^{-1}) however the sabot did hit the target containment box post-deflection and this can be seen in figure 33. Due to the deflection after the light curtain, no meaningful data can be inferred with regards to impact induced shocks as the velocity may have differed substantially post deflection.

The malfunction underlying Fault 4 was deemed to be a result of the sabot breaking up or distorting during flight. This was established through analysis of the oscilloscope reading that did not feature the indicative single sabot signal but a noisy signal suggesting multiple fragments travelling through the lasers. While a velocity may have been recorded (6.97 km s^{-1}) and the target impacted, it would be imprudent to make any predictions regarding the status of the sabot at impact and the delivery of its contents into the target and as such this shot was discounted. Further evidence of a sabot collapse mid-flight was found upon inspection of the splash containment box. Foil tape can be

applied to the face of impact-splash containment boxes (figure 34), which upon a failed shot can show evidence of a fragmentary impact. Figure 35 shows the effect that the sabot breaking up in flight had on the target during this shot.
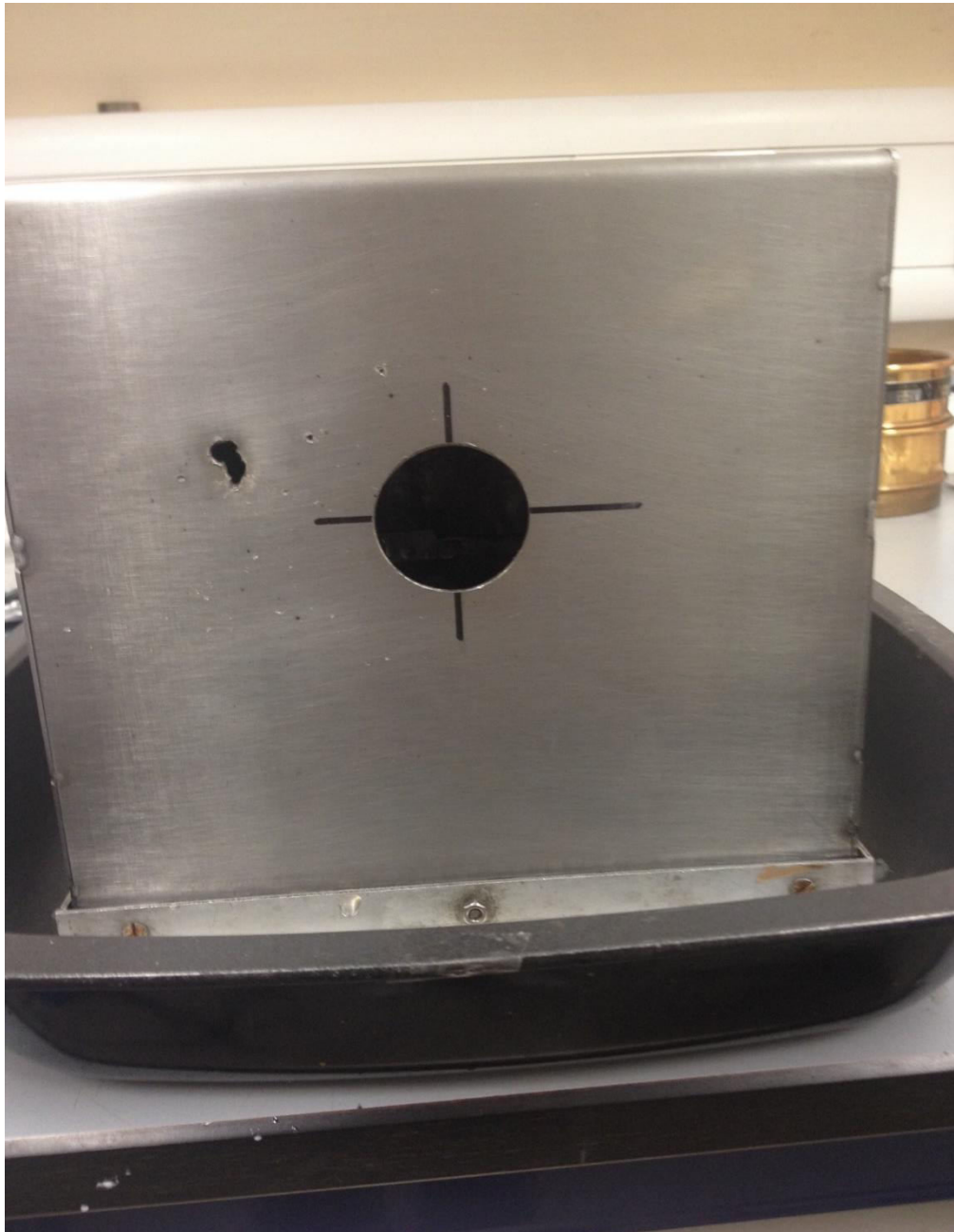
Figure 33: Face on view of the target containment box following an impact with the projectile as a result of fault 3.
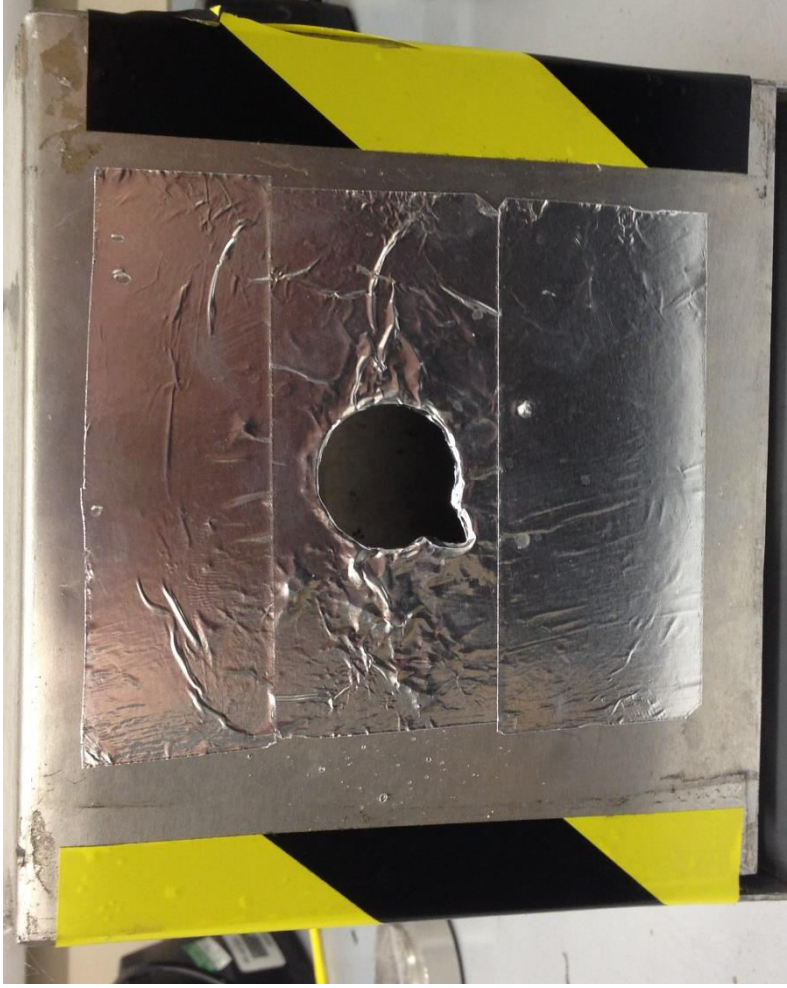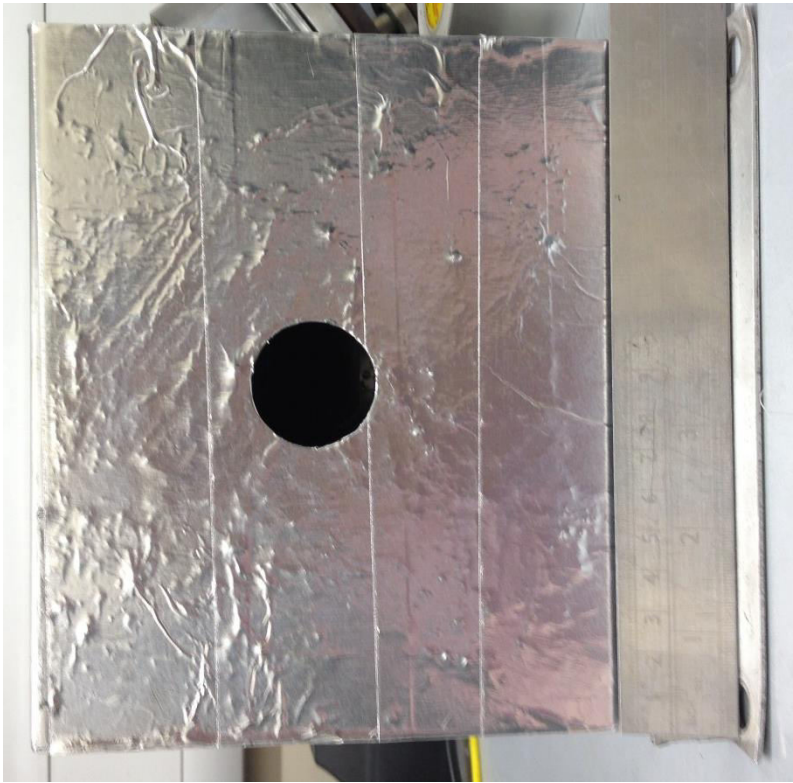
Figure 34: Face on view of two splash containment boxes with foil tape applied. This will provide evidence of any unintentional fragmentary impacts. If the tape is damaged (torn or cratered) post-shot it means that a spray of material has travelled down the gun.
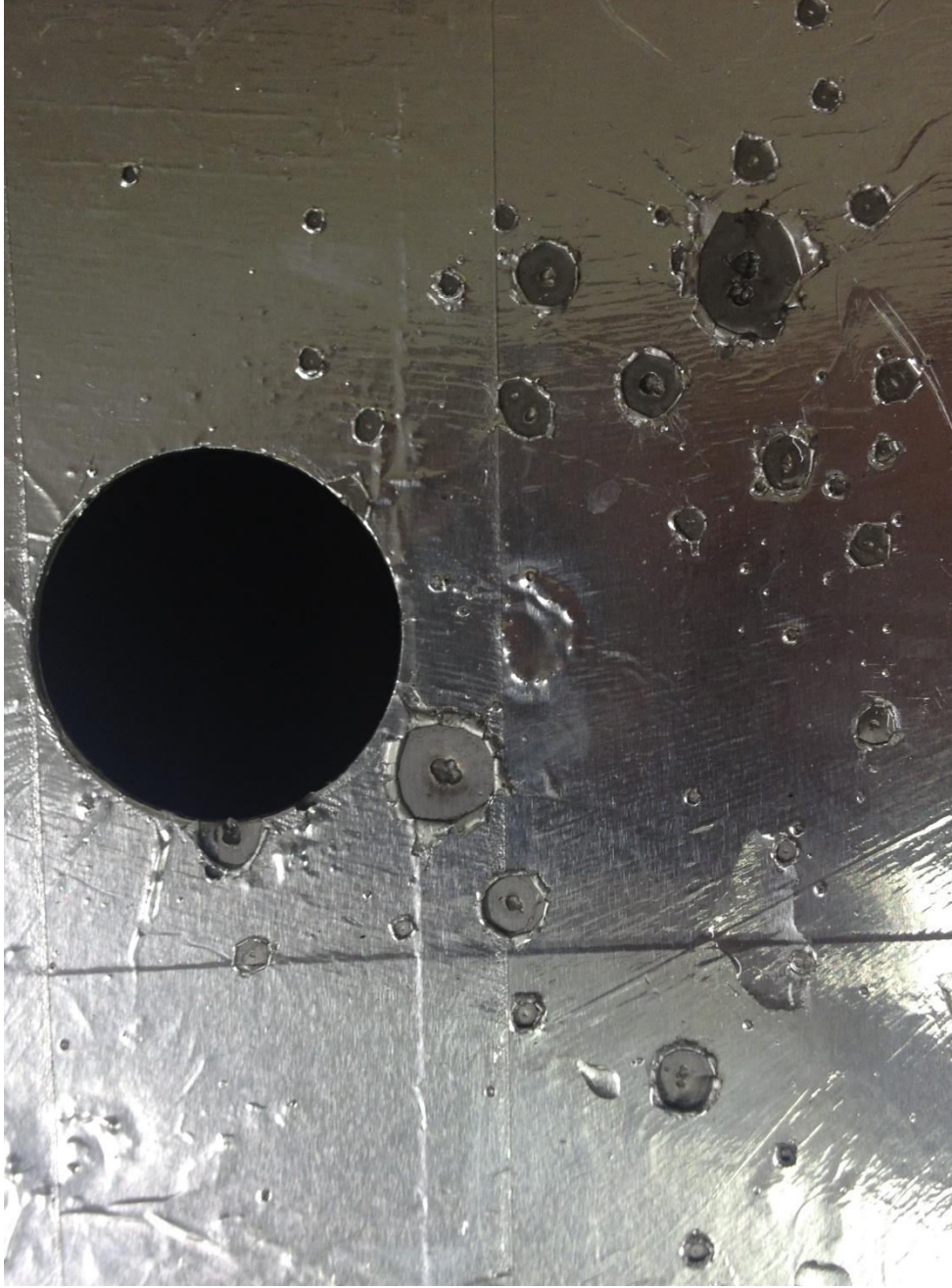
Figure 35: Face on view of the splash containment box with metallic tape applied. Impacts are clearly visible inferior to the entry hole. These could have been caused by ice from the sabot that has been liberated during flight

3.2. Analysis of Each Successful Shot (0.388 to 5.11 km s^{-1}).

The control sample was the first to be analysed once the experimental method had been devised. This featured a sabot prepared in the manner described in chapter 2. It was then placed within reverse osmosis water within the same plastic bags that would be used in the shot samples and allowed to thaw. This water was then filtered using Whatman filter paper and the filtrate imaged using an SEM. INCA software used alongside the microscope allowed for measurement of diatom fragment size, using digital callipers. Figure 36 shows an image of the fragments seen using the SEM. Note this image was created during a general scan of the SEM stub containing the sample and was not sourced from an SEM map.

S3400 10.0kV 11.0mm x233 BSECOMP   200um

Figure 36: This image also seen in chapter 2 shows an SEM image of a field of diatomaceous fossils sourced from the un-shot control. Here the diatoms were frozen within a sabot and then included in the water bag target. This was then filtered and imaged. This particular image was produced using the back scatter function on the SEM with the magnification set at x233.

Qualitative inspection of the SEM maps is supplemented by utilising energy-dispersive X-ray spectroscopy (EDX). The EDX unit allows for elemental mapping which is especially useful due to the distinctive chemical composition of diatom frustules (SiO_2). This facility is able to identify and characterise a sample's composition by the interaction of a beam of high energy electrons and the specimen under investigation. This beam can excite electrons that are bound to the nucleus within the inner electron shells. This results in the excited electron ejecting form its shell, leaving a hole. This is filled by an electron from a higher energy shell. It is the difference in energy between the shells that results in the release of an X-ray whose energy is characteristic of the specimen. Figure 37 shows the EDX-spectra of a fossil fragment identified within a sample of un-shot diatomaceous soil.
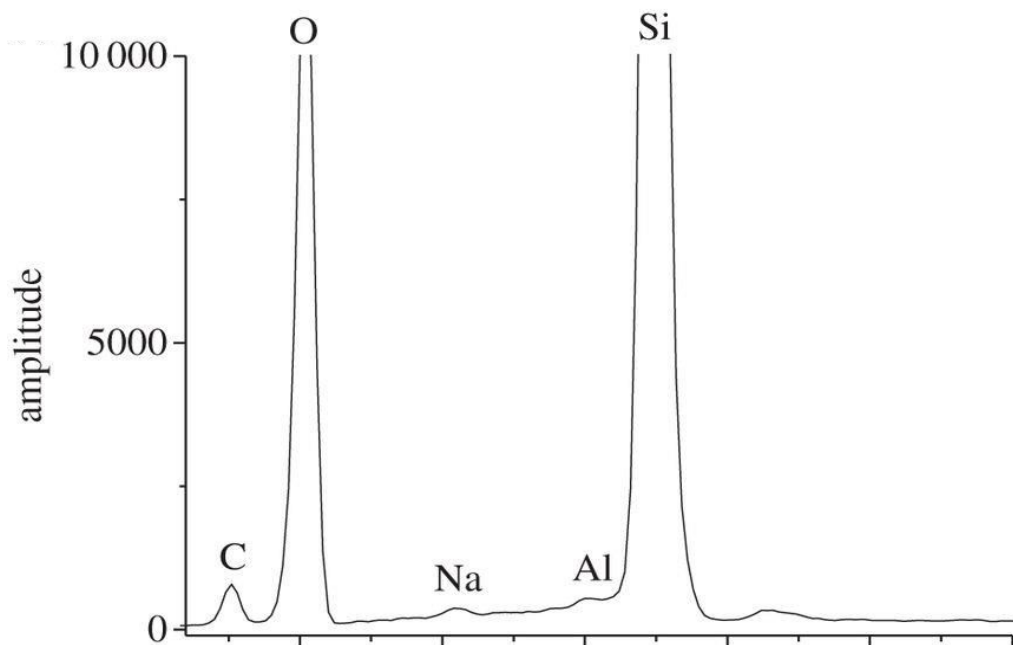

Figure 37: EDX-spectra of a diatom fossil fragment found within an unshot sample. Image credit: Dr Kathryn McDermott.

Table 3 shows the SEM analysis of the fragments yielding fossil fragment data. Fragment size statistics were taken from the first 500 fragments found following an SEM imaging map. Note that a mean size is given, with the uncertainty representing the uncertainty on the mean itself (and is not a measure of the width of the distribution). Here it is seen that the average size is (28.8 ± 0.8) μm while the largest fragment size is 180 μm. 180 μm is the largest possible fragment available due to the original sieving process of the diatomaceous soil. The second largest fragment was also given. This statistic will become important during the shot sample analysis due to the potential for anomaly hunting on the extremes of the sample distribution.

Table 3: Fossil fragment data as recorded from an SEM map of the un-shot control sample.

Impact Velocity (km s^{-1})	Total Fragments	Average Size (μm)	Largest Fragment (μm)	Second Largest Fragment (μm)
Unshot control	500	28.8 ± 0.8	180	136

The lowest velocity shot completed was at 0.388 km s^{-1} and table 4 Illustrates the fragment size statistics from this velocity. Table 4 shows diatomaceous fragment statistics that were taken from the first 500 fragments found following an SEM imaging map. In table 4 it is seen that the average size, (32.6 ± 0.8) μm, is slightly larger than that seen in the unshot control. However both the largest fragment size (119 μm) and second largest fragment size (105 μm) are significantly reduced. There were 14 intact diatoms also found in this study. See figures 38 and 39 for an SEM image of fossil fragments filtered after impact at 0.388 km s^{-1}.

Table 4: Fossil fragment data as recorded from an SEM map carried out on the filtrate following the shot at 0.388 km s^{-1}.

Impact Velocity (km s^{-1})	Total Fragments	Average Size (µm)	Largest Fragment (µm)	Second Largest Fragment (µm)
0.388	500	32.6 ± 0.8	119	105
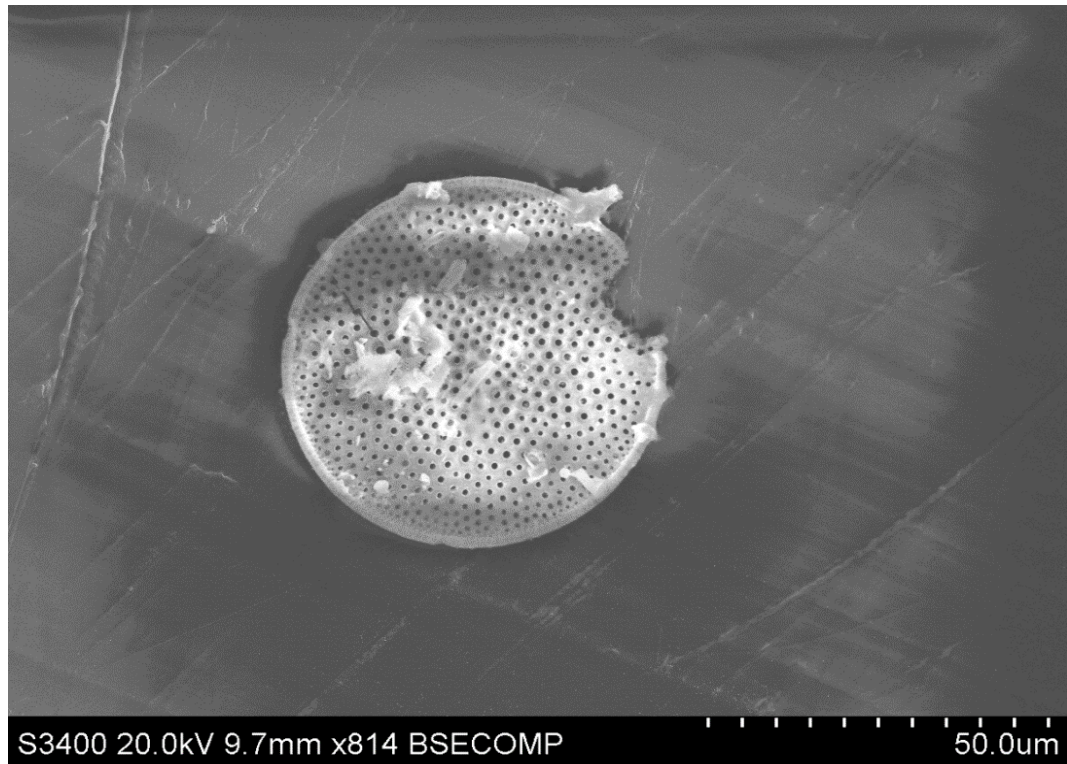
Figure 38: This image shows an example of diatom found in the SEM analysis of the 0.388 km s^{-1}.
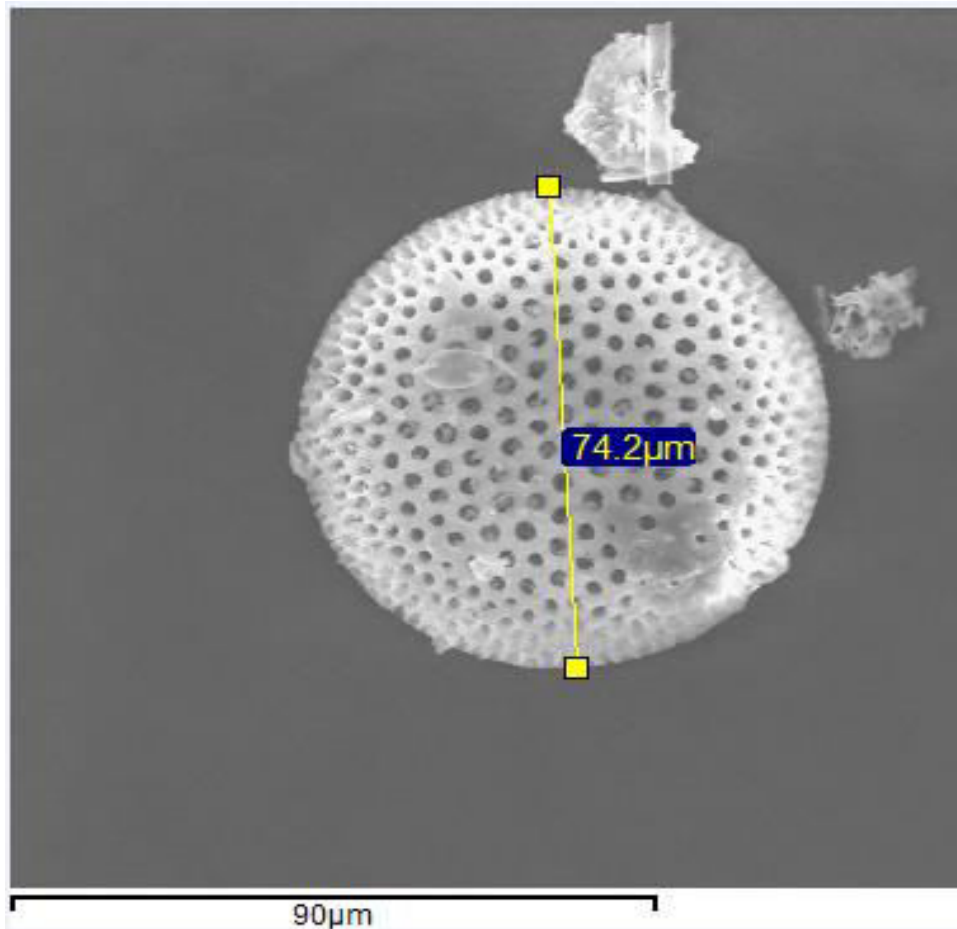
Figure 39: This image shows an example of diatom found in the SEM analysis of the 0.388 km s^{-1}. Also included is the calliper system used on fragments to determine the fragment sizes; this fragment is 74.2 µm

The next impact velocity in the series to be examined was at 1.26 km s^{-1}. Table 5 provides information on the fragment findings. This includes diatomaceous fragment statistics that were taken from the total fragments found following an SEM imaging map. Here the average size is (20 ± 1.1) µm, a marked decrease against the control and the shot at 0.388 m s^{-1}. The largest fragment size (80.7 µm) and second largest fragment size (62.8 µm) are also reduced. No intact diatoms were found in the initial SEM map however a general inspection of the SEM stub yielded a number of intact fragments in the sample. See figure 40 for an SEM image of fossil fragments filtered after impact at 1.26 km s^{-1}. These results indicate that intact fossils were becoming rarer. Also only 126 fragments were measured, compared to 500 previously due to decreasing sample population size in this higher velocity shot. This sample population size

decrease may have been due to a number of factors. This would include the fragments that are too small to be recognised. There was also an increase in debris from the bags of water as the shot speeds increased. This would act to obscure some fragments which may have been present on the filter paper.

Table 5: Fossil fragment data as recorded from an SEM map of the filtrate following the shot at 1.26 km s^{-1}.

Impact Velocity (km s^{-1})	Total Fragments	Average Size (µm)	Largest Fragment (µm)	Second Largest Fragment (µm)
1.26	126	20.0 ± 1.1	80.7	62.8

S3400 20.0kV 10.0mm x700 BSE3D   50.0um

Figure 40: This image shows an intact diatom found in the SEM analysis of the filtrate of the 1.26 km s^{-1} shot. The strand of material crossing the image is a fibre stripped from the filter paper.

Also seen during analysis of this sample was an SEM artefact known as charging and sample shifting as a consequence. Charging is an event where the number of incident electrons hitting a sample exceeds those ejected. This leads to a build-up of negative charge at the site. As such, aberrant effects such as contrast shifting, bright flashes from sudden discharge and even sample material shifting can occur. Figure 41 show fragments shifting due to charging. Charging occurred during SEM analysis of other shots as well, and usually manifested as areas of extreme brightness (also seen in figure 39). This phenomenon can be minimised by an application of a conductive film over the sample.
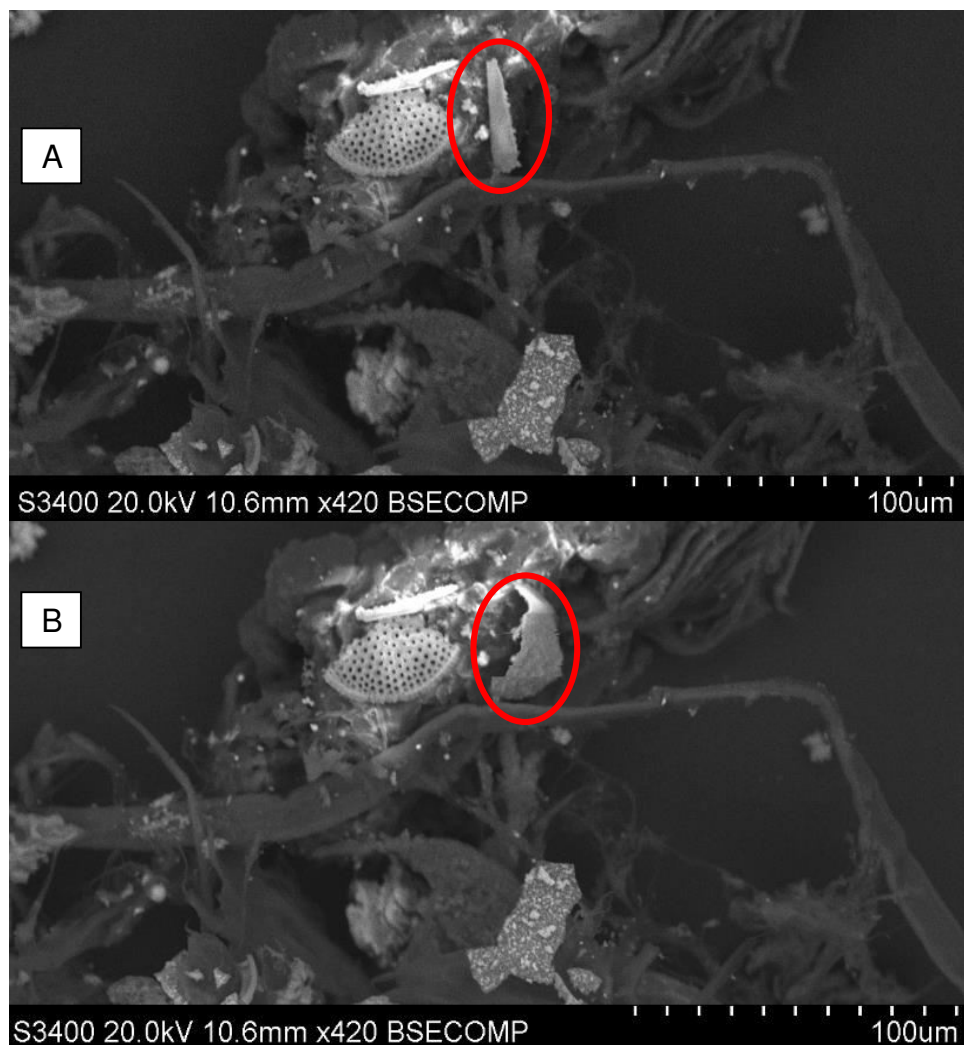
Figure 41: These images highlight a fragment shifting (circled) as a result of charging, during an observation of the sample from the 1.26 km s^{-1} shot. To the left of the circled fragment is an area of increased brightness, another manifestation of sample charging.

Table 6 shows diatomaceous fragment statistics that were taken from the total fragments found following an SEM imaging map of the fragments in the shot at 2.05 km s^{-1}. Here the average size is (19 ± 1.1) μm. The largest fragment size (58.9 μm) and second largest fragment size (45.8 μm) were also reduced. See figure 42 for an SEM image of a fossil fragment filtered following the impact at 2.05 km s^{-1}. Again no intact diatoms were seen during analysis of the SEM map but a general inspection of the SEM stub did yield intact fossils (figure 43).

Table 6: Fossil fragment data as recorded from an SEM map of the filtrate following the shot at 2.05 km s^{-1}.

Impact Velocity (km s^{-1})	Total Fragments	Average Size (μm)	Largest Fragment (μm)	Second Largest Fragment (μm)
2.05	81	19.1 ± 1.1	58.9	45.8
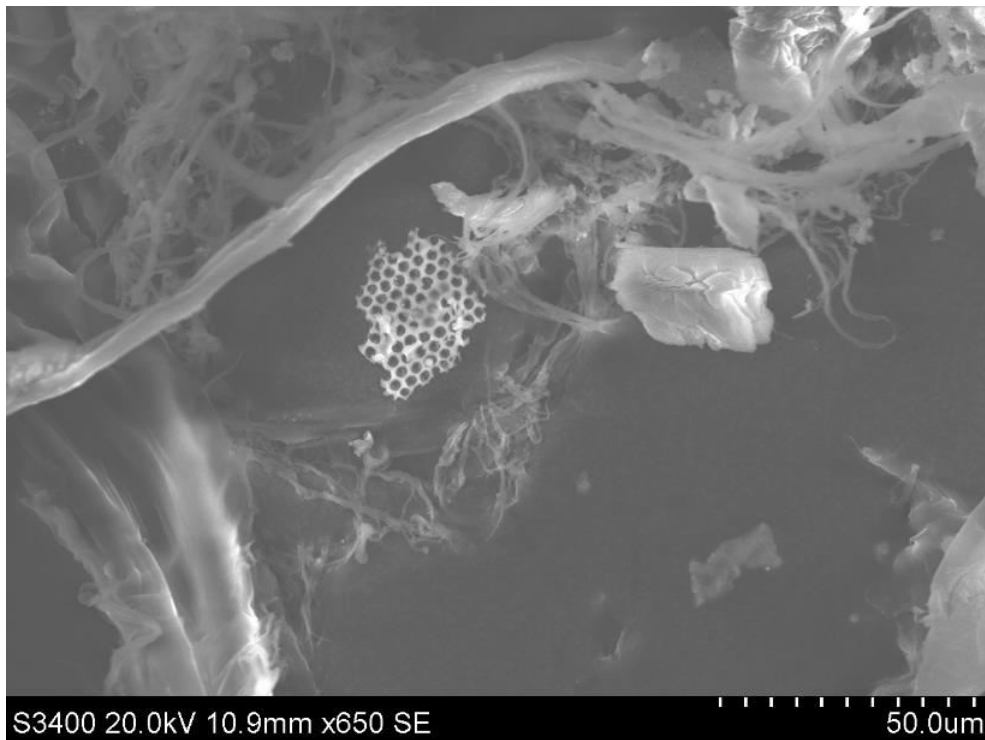
Figure 42: This image shows a diatom fragment found in the SEM analysis of the filtrate following the shot at 2.05 km s^{-1}.

S3400 20.0kV 11.0mm x951 BSECOMP   50.0um

Figure 43: This image shows an intact microfossil in during a general inspection of the SEM stub, containing filtrate following the shot at 2.05 km s^{-1}. No intact fragments were found during an SEM map.

Table 7 shows diatomaceous fragment statistics of the 3.14 km s^{-1} shot that were taken from the total fragments found following an SEM imaging map. Here the average size was (15.9 ± 1.5) μm. The largest fragment size (40.2 μm) and second largest fragment size (39.7 μm) were also reduced. See figure 44 for an SEM image of a fossil fragment filtered following the impact at 3.14 km s^{-1}.

Table 7: Fossil fragment data as recorded from an SEM map of the filtrate following the shot at 3.14 km s^{-1}.

Impact Velocity (km s^{-1})	Total Fragments	Average size (μm)	Largest Fragment (μm)	Second Largest Fragment (μm)
3.14	33	15.9 ± 1.5	40.2	39.7
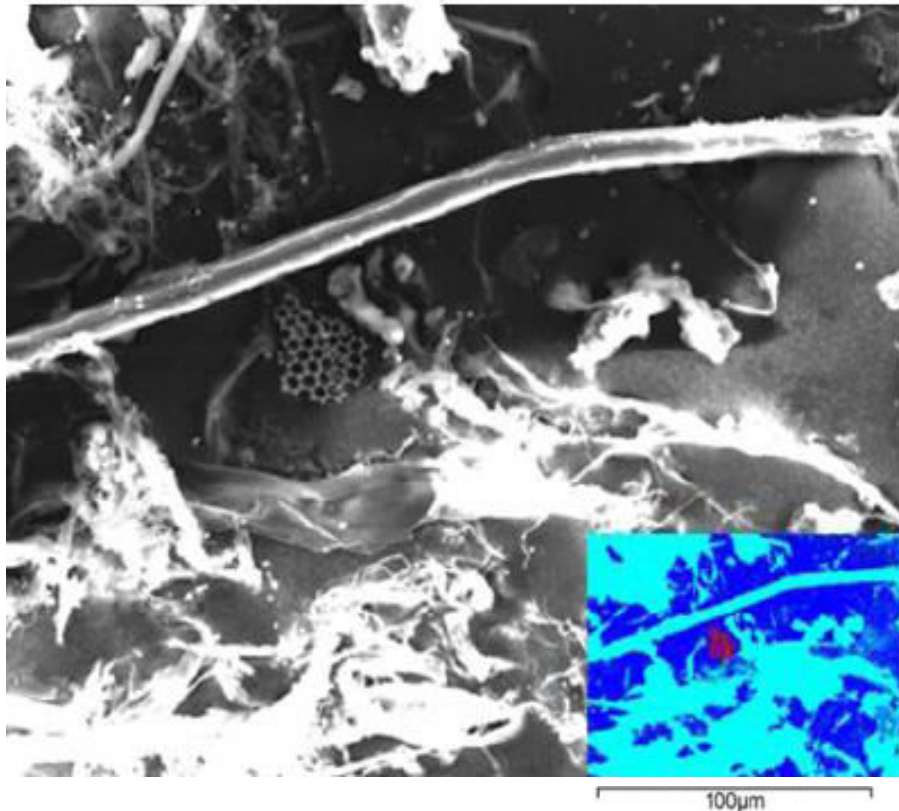
Figure 44: This image shows a diatom fragment found in the SEM analysis during the 3.14 km s^{-1}. The panel in the lower left has been coloured so that the desired item is highlighted (the diatom fragment is in red). Image credit: Dr Kathryn McDermott.

Table 8 shows diatomaceous fragment statistics that were taken from the total fragments found following an SEM imaging map of the 4.1 km s^{-1} shot. Here the average size was (17.3 ± 1.6) μm. The largest fragment size (39.6 μm) and second largest fragment size (36.8 μm) are also reduced. See figure 45 for an SEM image of a fossil fragment filtered following the impact at 4.1 km s^{-1}.

Table 8: Fossil fragment data as recorded from an SEM map of the filtrate following the shot at 4.1 km s^{-1}.

Impact Velocity (km s^{-1})	Total Fragments	Average size (μm)	Largest Fragment (μm)	Second Largest Fragment (μm)
4.1	31	17.3 ± 1.6	39.6	36.8
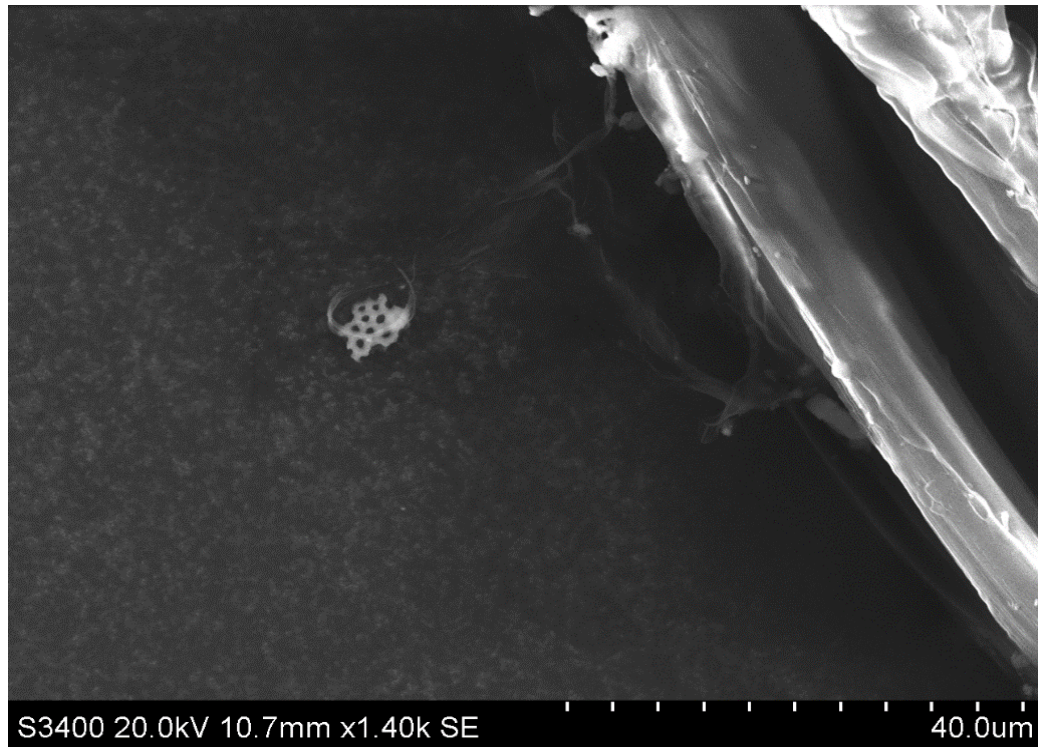
Figure 45: This image shows a diatom fragment found in the SEM analysis during the 4.1 km s^{-1}.

Table 9 shows diatomaceous fragment statistics that were taken from the total fragments found following an SEM imaging map of the 5.11 km s^{-1} shot. Here the average size was (16.9 ± 3.7) μm. The largest fragment size was surprisingly high at 61.8 μm, as was the second largest fragment size 46.9 μm, See figure 46 for an SEM image of a fossil fragment filtered following the impact at 5.11 km s^{-1}.

Table 9: Fossil fragment data as recorded from an SEM map of the filtrate following the shot at 5.11 km s^{-1}.

Impact Velocity (km s^{-1})	Total Fragments	Average size (μm)	Largest Fragment (μm)	Second Largest Fragment (μm)
5.11	17	16.9 ± 3.7	61.8	46.9
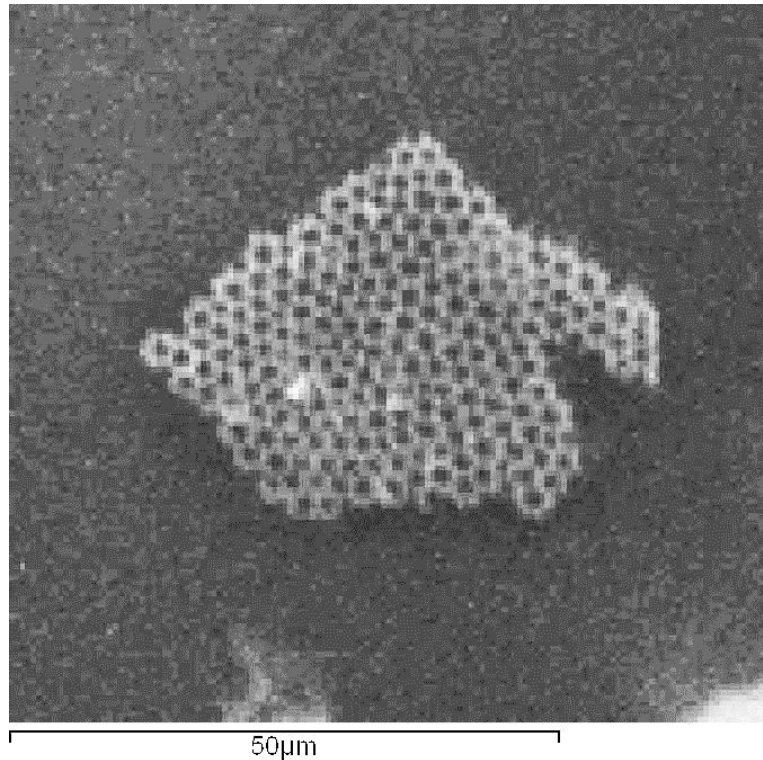
Figure 46: Image of a recovered fragment following an impact at 5.11 km s^{-1}. This image has had its brightness and contrast adjusted so as to make the image clearer.

Table 10 shows, in one place, all of the fossil fragment data collected upon analysis of each SEM map. The trends in the mean size, largest, and second largest fragment size against impact velocity are apparent. This relationship between the size metrics and the impact velocity can also be seen graphically in figure 47. In figure 47 there is an initial drop in each statistical measure. From ~3 km s^{-1} upwards there is a flattening of the size values. It is not clear why the largest fragment in the 5.11 km s^{-1} shot is quite so large. One speculative reason may be that the fragment was occupying an area of low pressure within the sabot upon impact. However further investigation utilising the hydrocode AUTODYN (carried out by Dr Mark Price), yielded minimum pressure values still much higher than the peak pressure seen in the lower speed shots at 17 GPa [56]. The peak pressure values calculated using the PIA will be discussed later in the next sub-section of this chapter.

Table 10: Overall fragment data.

Impact Velocity (km s^{-1})	Total	Mean (µm)	Largest Fragment (µm)	Second Largest Fragment (µm)
0	500	28.8 ± 0.8	180	136
0.388	500	32.6 ± 0.8	119	105
1.26	126	20 ± 1.1	80.7	62.8
2.05	81	19.1 ± 1.1	58.9	45.8
3.14	33	15.9 ± 1.5	40.2	39.7
4.1	31	17.3 ± 1.6	39.6	36.8
5.11	17	16.9 ± 3.7	61.8	46.9
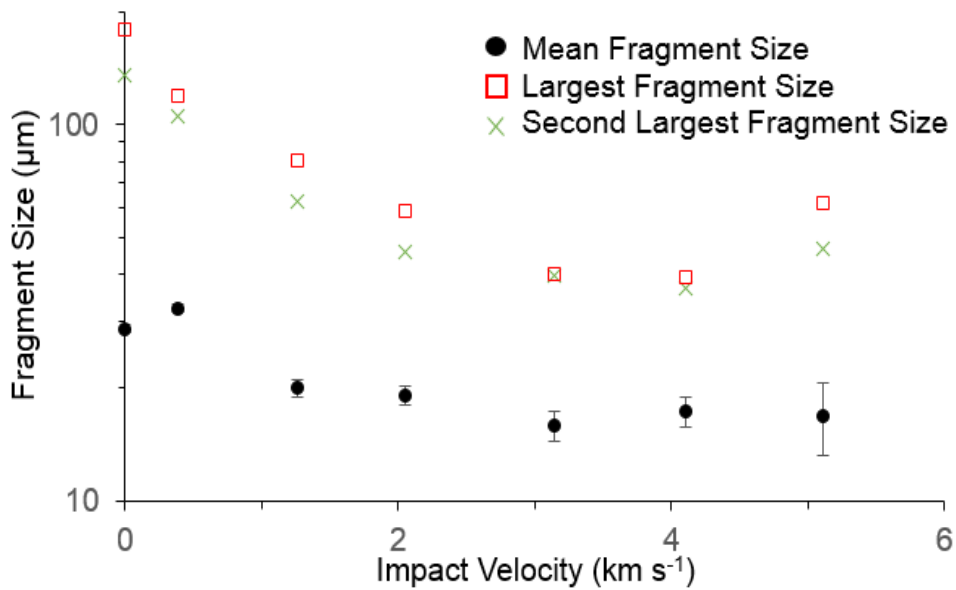
Figure 47: Size distribution of recovered fragments versus impact speed. Please note the sample at 0 km s^{-1} refers to the unshot control. The mean size as well as largest and second largest fragment values are included across the achieved velocities.

3.3. Applying the Planar Impact Approximation to the Fossil Shot Data.

As has previously been discussed, the Planar Impact Approximation (PIA) provides an estimate of the peak shock pressure behind the impact front. Table 11 illustrates the calculated peak shock pressure experienced by the projectile in these shots according to the PIA. The ρ_i, C and S values for water ice are given as 915 kg m^{-3}, 1317 m s^{-1} and 1.526 respectively [57].

This method (PIA) is disadvantaged somewhat by its inability to allow for a projectile with mixed contents. This is more important for modelling the peak pressure of the diatomaceous soil shots as this involved suspending silicate microfossils in water and freezing them. This then assumes that the continuous media through which the shock propagates is the ice. As a result in the following section the material-specific constants will be derived from water ice and these will be used in the PIA. Note that the role of the sabot material (nylon) is also neglected in this approximation.

Table 11: Peak Pressure calculated using the PIA.

Impact Velocity (km s^{-1})	PIA Peak Pressure (GPa)
0.388	0.4
1.26	1.6
2.05	3.2
3.14	6.1
4.05	9.3
5.11	13.3

Refer to figure 48 for a graphical representation of the relationship between impact velocity (km s^{-1}) and peak pressure (GPa) in this shot. As can be seen here the peak shock pressures at these speeds can rise to over 10 GPa. The close relationship between shot velocity and peak pressure is clear, but is not linear.
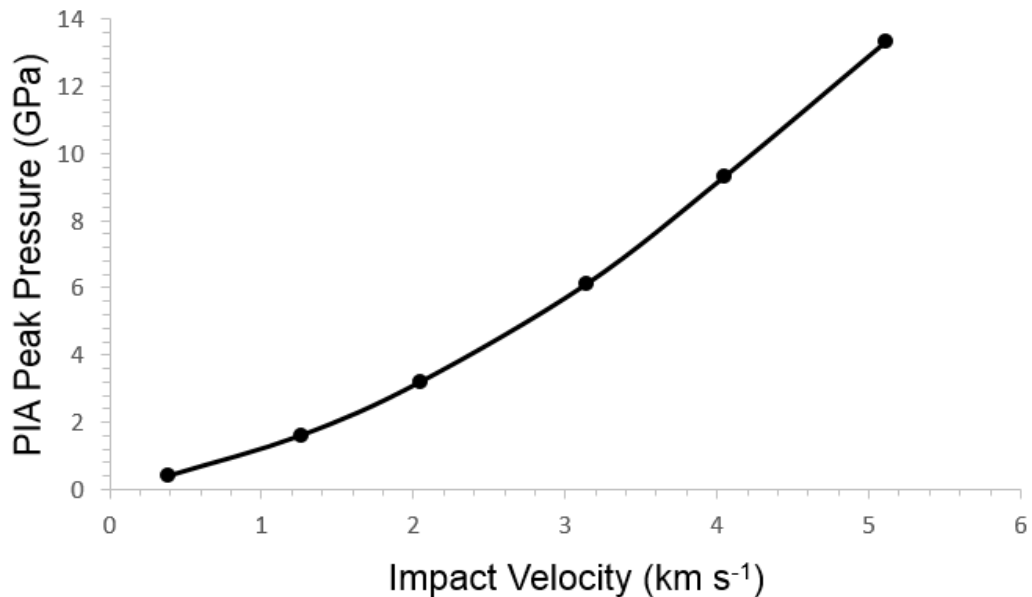
Figure 48: A plot of peak shock pressure (GPa) calculated for the impact velocities (km s^{-1}) seen in table 10.

We have examined the peak shock pressures that diatom fossils can endure, and be recoverable at in our specific experimental case; that is, an impact into water of a frozen diatomaceous soil loaded nylon sabot. The shot speeds were determined, based on previous theoretical study [27]. While recoverability of fragments at the given impact velocities was a key motivation for impacting into water, the question does arise as to whether this is a useful analogue to a real impact case series i.e. a meteorite originating from earth impacting the Lunar surface. Calculations into peak pressure and impact velocity of typical Earth and Lunar materials should also be included to clarify the relevance here.

We feature here the calculations of the PIA of two Earth materials. Granite, a core constituent of the Earth's crust and Coconino sandstone, a sedimentary rock that the Barringer Crater in Arizona was formed in. These materials would, in these calculations be impacting basalt, representing the Lunar Mare. Table 1 provides the respective values that are required for the linear wave speed equation (3) and the PIA.

Table 12: Linear wave speed and PIA input values for specific materials.

Rock	C (m s^{-1})	S	Density (kg m^{-3})
Basalt	2600	1.62	2860
Granite	3680	1.24	2630
Coconino Sandstone	1500	1.43	2000

The peak shock pressure of an impact between granite and basalt was calculated. The impact speed values are shown from 0.5 km s^{-1} to 5 km s^{-1}. The results can be seen in table 13.

Table 13: Peak Pressure calculated using PIA: Granite into basalt.

Impact speed (km s^{-1})	Peak Pressure (GPa)
0.5	2.37
1	5.36
1.5	8.64
2	12.5
2.5	16.8
3	21.7
3.5	27.1
4	32.9
4.5	39.1
5	46

Figure 49 shows the close relationship between impact speed and peak pressure in an impact between a granite impactor and a basaltic target.
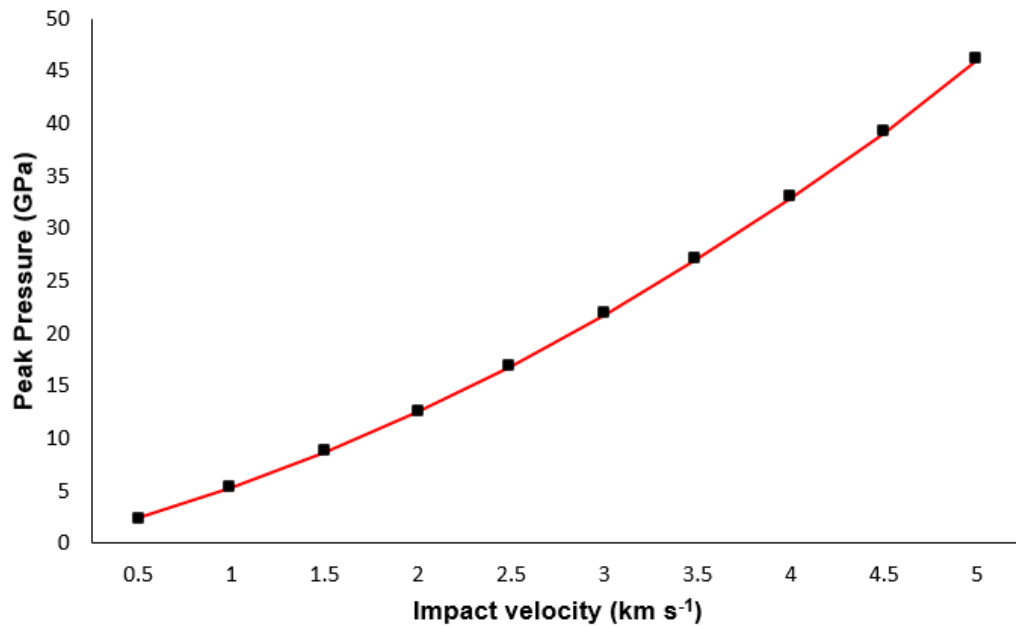
Figure 49: PIA for granite impacting basalt.

Following the calculation of the PIA of granite and basalt, Coconino sandstone was also investigated. Using the values seen in table 12, the PIA was calculated for an impact between a Coconino sandstone impactor and a basaltic target.

Table 14: Peak Pressure calculated using PIA: Coconino sandstone into basalt

Impact speed (km s^{-1})	Peak Pressure (GPa)
0.5	1.34
1	3.16
1.5	5.46
2	8.2
2.5	11.4
3	15.1
3.5	19.2
4	23.7
4.5	28.7
5	34.2
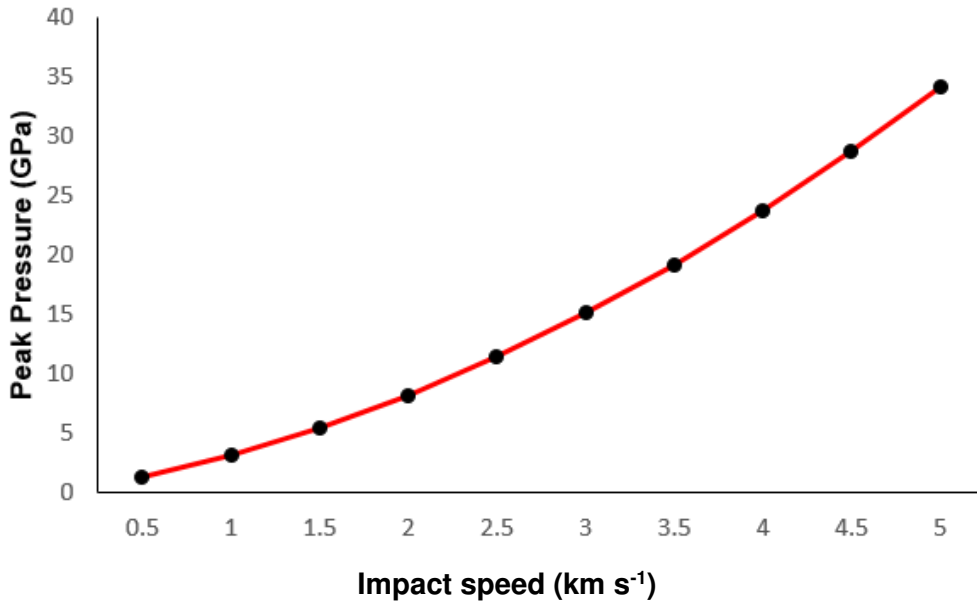
Figure 50: PIA for Coconino sandstone impacting basalt.

The sandstone impact into basalt illustrates overall a lower peak pressure than the granite impacts. Comparing the peak pressure of the rock calculations (granite or Coconino sandstone impacting into basalt) to the frozen diatomaceous soil of the described experimental series featured here, is informative. The highest impact velocity ~5 km s^{-1} achieved by our experiments resulted in a peak pressure value of 13.3 GPa. This was far exceeded by the pressure values at similar calculated impact velocities, the 5 km s^{-1} impact of granite resulted in 46 GPa and the Coconino sandstone was determined to be 34.2 GPa upon impact into basalt. This highlights an inability of this experimental series to access the high levels of peak shock pressure seen in rock on rock impacts. However we were able to achieve the peak pressures between of the granite and Coconino sandstone into basalt when these impacts occur at velocities of 2 - 3 km s^{-1}, after this point the rock on rock peak pressures swiftly exceed that which we were able to achieve. This is important to note as not only do we still see recoverable fragments at this peak pressure level but as seen in Armstrong 2010 [27] the probability of these lunar impacts is heightened (table 15). In order to match the rock on rock impact pressures at increasing velocities, the experimental method illustrated here should be developed to satisfy this need.

Table 15: Probability of lunar impact velocities

Vertical Velocity (km s^{-1})	Probability	Impact Pressure (GPa)
0.5	0.29	0.5
1	0.43	2
2	0.6	8
2.5	0.71	12

Table 15: Adapted from [27] impact probabilities and associated impact pressures. These

shock pressures re accessible to us in our system.

A graphical representation, comparing the size metrics (mean size, largest and second largest fragment) used in this study versus shock pressure (GPa) can be seen in figure 51. Here the mean fragment size decreases readily with each increase in shot velocity and the resultant shock pressure. This inverse relationship is also seen in the analysis of the largest fragments found and the second largest fragments. The sample size also decreases in a similar manner. However above about 6 GPa (~3 km s^{-1}) this decrease ceases. Above 1.26 km s^{-1} no intact microfossils were found using the SEM mapping process. This led to general inspections of the SEM stub that resulted in intact microfossils being detected in the filtrate from impact velocities up to 2.05 km s^{-1}.
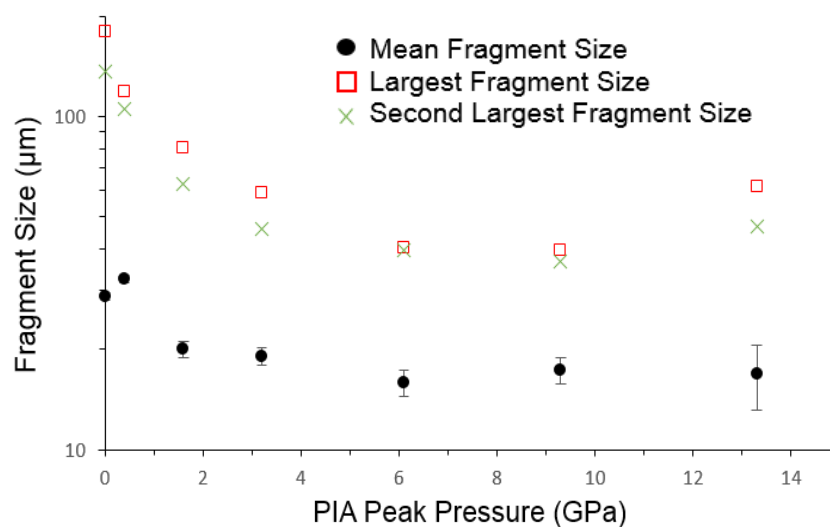

Figure 51: Plot of recovered fragment sizes (mean, largest and second largest fragment) versus peak shock pressure (GPa) calculated using the PIA.

CHAPTER FOUR:

RESULTS OF PROJECT TWO.

4.1. Pressure testing liquid core sabots.

Originally it was planned to also conduct a series of experiments with various samples placed in water. However when the first test was done a problem emerged with the sabot. With this issue observed the experimental programme was change, becoming a programme to develop a method of firing a sabot with liquid contents.

The initial observation was made that sabots containing liquid water sealed with a simple acetate lid (when held at vacuum pressure of 50 and 100 mbar), were not robust enough and were losing their water contents to evaporation. Three prospective sabot designs that might preclude the loss of liquid were thus investigated. The 3 types are described in detail in chapter 2 and briefly summarised here.

Design 1: A sabot with an acetate lid sealed with adhesive.

Design 2: A sabot with a 1mm rubber lid also secured with an adhesive.

Design 3: A sabot modified via counter-boring with an inset lid, this would have a thin film of adhesive on top of lid.

In each sample, pressure tests started at 100 mbar and were carried out within the gun's target chamber. The sabots were placed on a petri dish within the recess of the target chamber window. Food colouring was also added to the water to aid visualisation. During chamber evacuation it was noted that the acetate lid (of design 1) had lifted slightly. This occurred on all three of the unmodified sabots with acetate lids which were tested in this fashion. This confirms and explains the initial problem with this design. Following this and the final and most important observation that the contents had evaporated, the determination was made that this design should be eliminated.

The rubber sealed sabot (design 2) fared better (Figure 48) with regards to lid retention and thus seal rigidity. However both examples used in this test, that had had their liquid contents injected into them, were unable to store their liquid core. The injection hole proved to be a weak spot. This was highlighted by red colouring residue sitting on top of the sabot over the injection hole. The two examples that had been filled prior to sealing had retained liquid but the level was noticeably diminished. One core problem unrelated to liquid retention was the difficulty in removing the rubber lid. This had to be cut away (see figure 52). Given all of these problems, this design was also considered unviable.
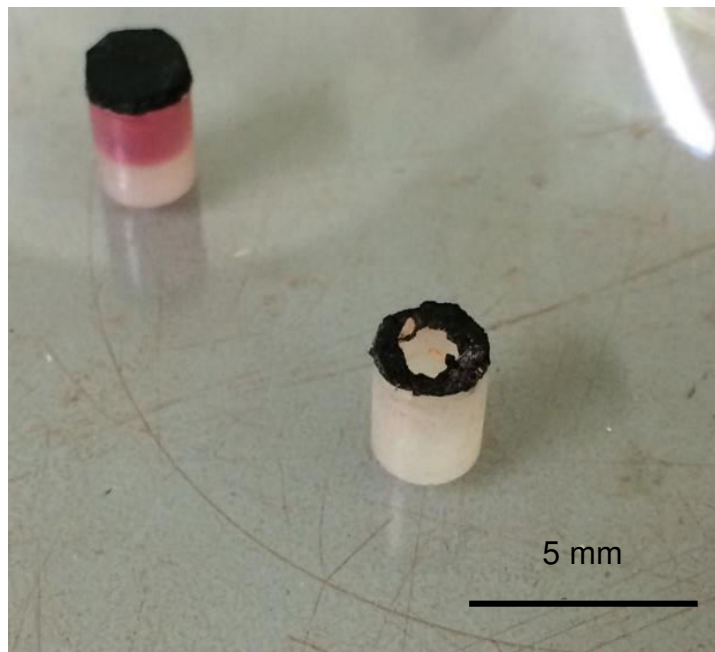
Figure 52: An image of two sabots with the rubber lid. The top-left sabot did not undergo pressurisation and the coloured liquid is clearly visible. The bottom-right sabot has had its contents fully evaporated, and required cutting of the lid to access

The third and final design was then tested. This configuration was a counter-bored sabot with an inset acetate lid which sat 0.5 mm from the sabot's surface. Two of these sabots were used in each pressure test. This was the most robust of all the designs with regards to liquid retention, retaining its volume at 100 mbar for 5 minutes. This design was also exposed to 50 mbar

for 5 minutes which it also withstood (see figure 53 for the counter-bored sabot in the evacuated chamber).

It also provided greater access to its contents post-seal. A simple scalpel score around the inner well wall was required and then the lid could be pried away. This sabot design was then taken into the shot phase.
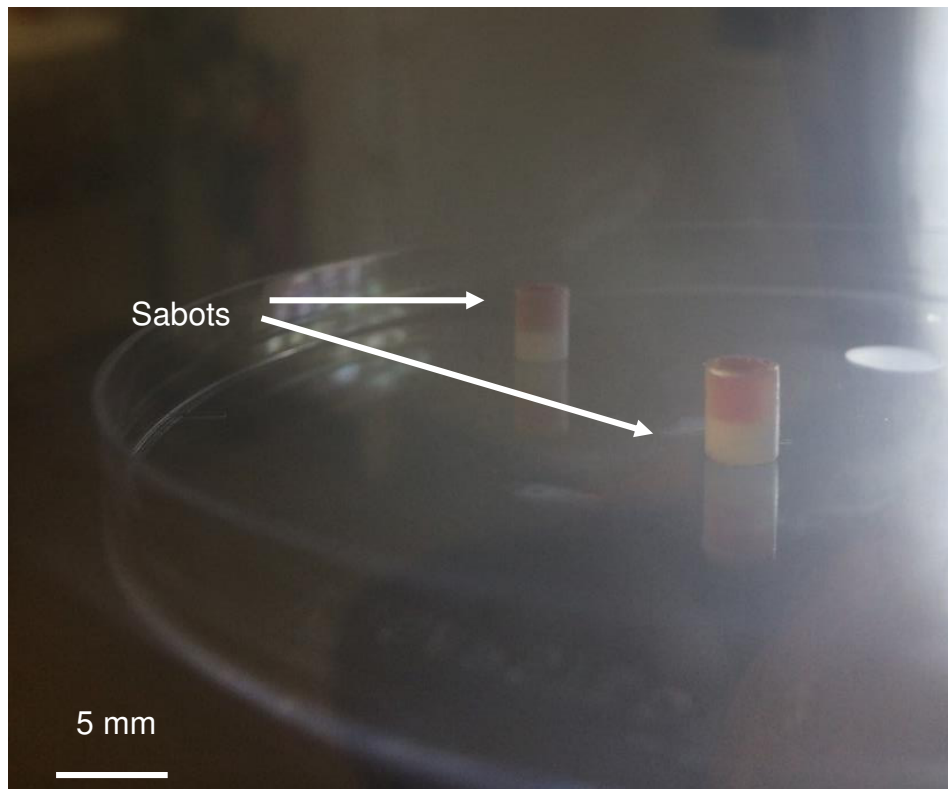
Figure 53: An image of two sabots within the target chamber (looking in through the portal window). The pressure within the chamber was 50 mbar and this was held for 5 minutes, a typical time that a sabot would be exposed to low pressure when loaded into the gun. The counter-bored sabots withstood this pressure and retained their contents.

4.2. Shots with the new liquid core sabot design.

In order to clarify how the counter-bored sabot would perform during an impact, a shot investigation with the light-gas gun was carried out. This involved a shot programme featuring the counter-bored sabot design with a

glass bead to confirm the transmission of contents from sabot to target. The glass bead was placed in the sabot that also contained liquid water.

Two shots were carried out, at 0.417 and 0.897 km s^{-1}. In both shots, the glass bead was transmitted to the target and subsequently recovered intact. This provides evidence that the methods can be used in future experiments requiring sabots filled with water (e.g. biological material that does not respond well to freezing). Figure 54 and 55 show the transmitted debris (projectile and contents) recovered from the target box following the 0.415 and 0.897 km s^{-1} shot respectively (table 12).
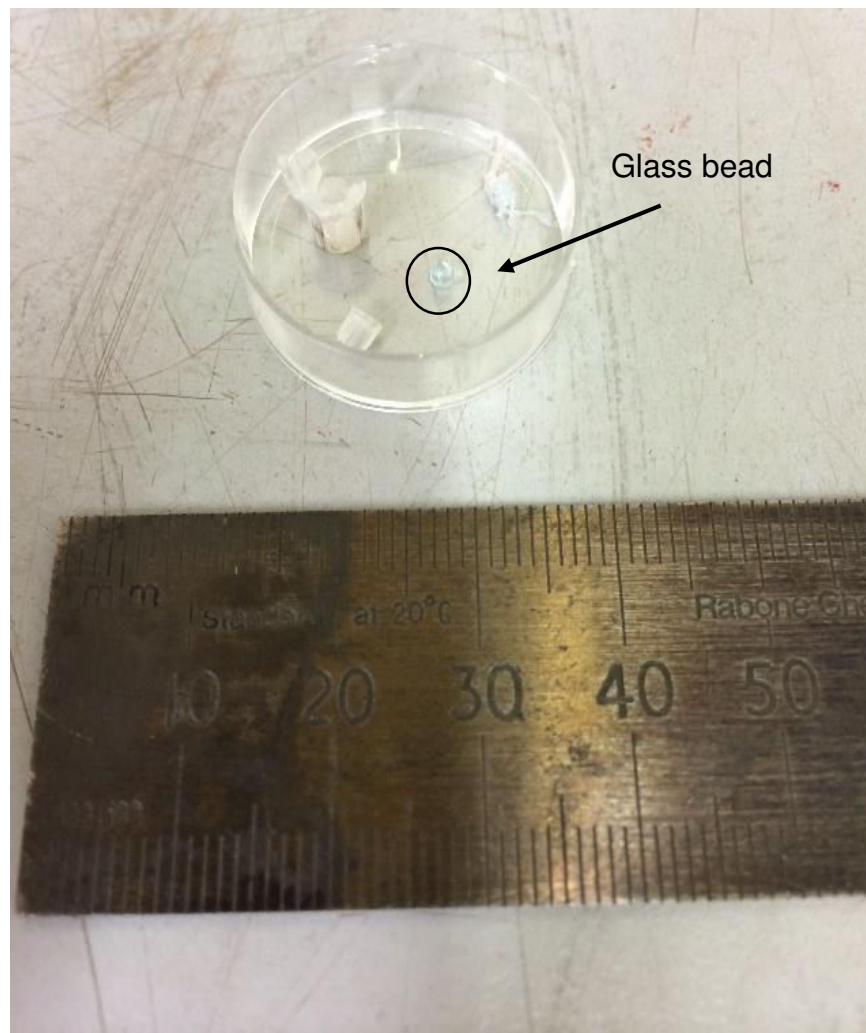
Figure 54: Image of the recovered debris from the target following an impact at 0.415 km s^{-1}. The glass bead (2mm in diameter) is highlighted. The sabot remained largely intact post-impact at this speed.
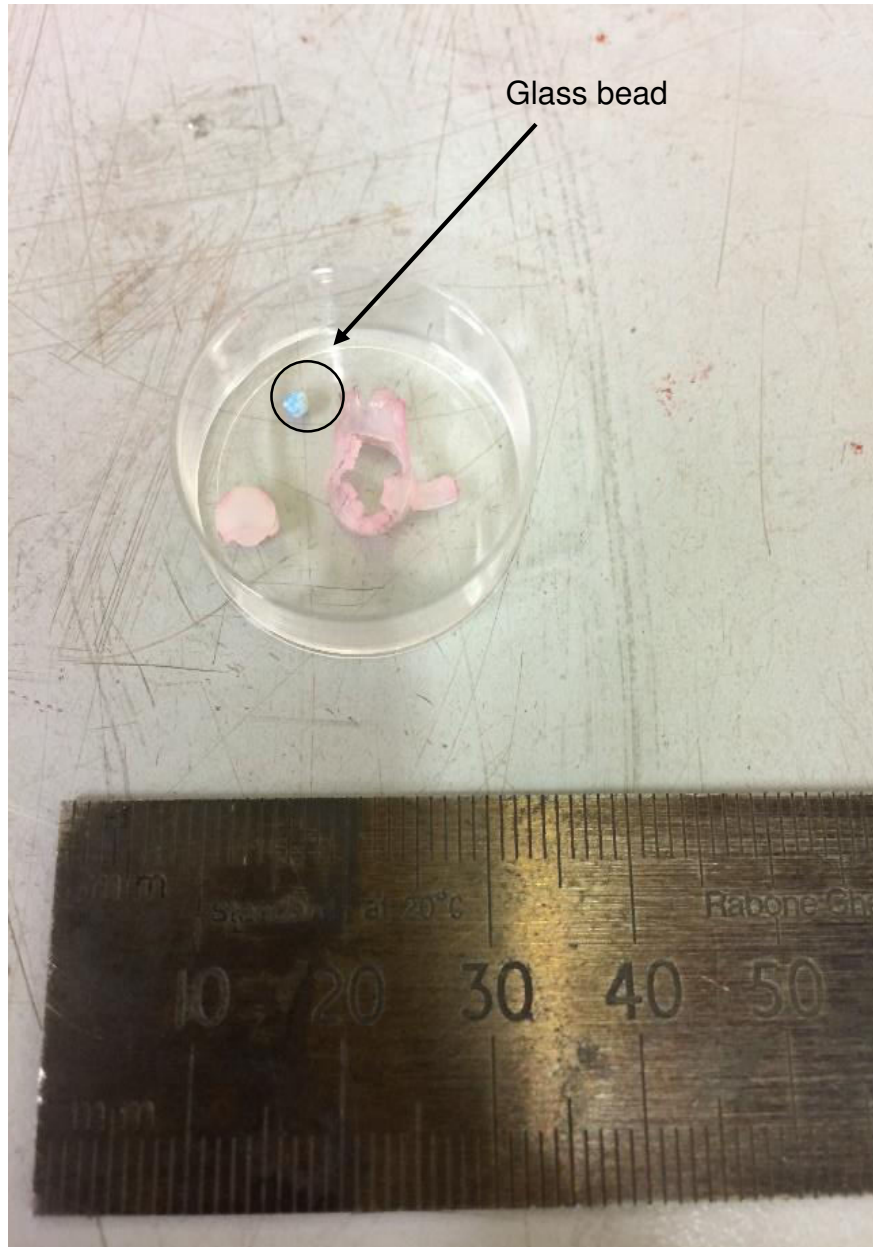
Figure 55: Image of the recovered debris from the target following an impact at 0.897 km s^{-1}. The glass bead (2 mm in diameter) is highlighted. The sabot while damaged is still recoverable at this speed, in this instance in two parts.

Table 12: An overview of the shot programme featured the modified liquid core sabot with reference to glass bead transmission into the water target.

Shot Velocity (km s^{-1})	Gas	Projectile contents	Glass Bead Detected in Target?
0.415	He	2 mm glass bead and water	Yes
0.897	H$_2$	2 mm glass bead and water	Yes

The glass beads following both impact velocities (0.415 and 0.897 km s^{-1}) were recovered. While empirical verification of the transmission of a sabot's contents was the main focus here, the condition of the glass beads was also investigated. The reasoning for this was that glass beads have a tendency towards breaking apart during impacts and so have limited utility. Further inspection under a light microscope showed that the glass bead used during the lower impact velocity shot, 0.415 km s^{-1} showed signs of superficial grazing. The glass bead used in the higher impact velocity shot 0.897 km s^{-1}, had greater surface damage. This may suggest that investigating the suitability constraints of the liquid core sabot at higher impact velocities, may require a different tracer to the glass bead.

Figure 56 shows a sequence of images of the impact at 0.897 km s^{-1} while figures 57 and 58 show the target box following impacts at 0.415 and 0.897 km s^{-1} respectively. The target was modified from that seen in chapter 2 within the description of the fossil project. Here, the splash containment box itself, not plastic bags secured within the box was filled with water. The box was inverted and filled with water and the previously described baseplate was now the lid for the box. This modification to the target allowed for the recovery of the glass bead in a more efficient manner by minimising impact debris; using the plastic bags in the fossil project resulted in debris from the bags.

The water within the target was coloured red. This colouration was chosen as the impact was to be imaged. This highlights what occurs during the impact and also provides confirmation externally that the impact itself had occurred.

Figure 56: A sequence of 3 images showing the impact of the second shot featuring the counter-bored sabot with an inset lid at a velocity of 0.897 km s^{-1}. The sabot enters the target box via an aperture which is covered by a thin plastic lining. The box had been pre-filled with red dyed water which can be seen emerging in the second and third frame in this sequence.
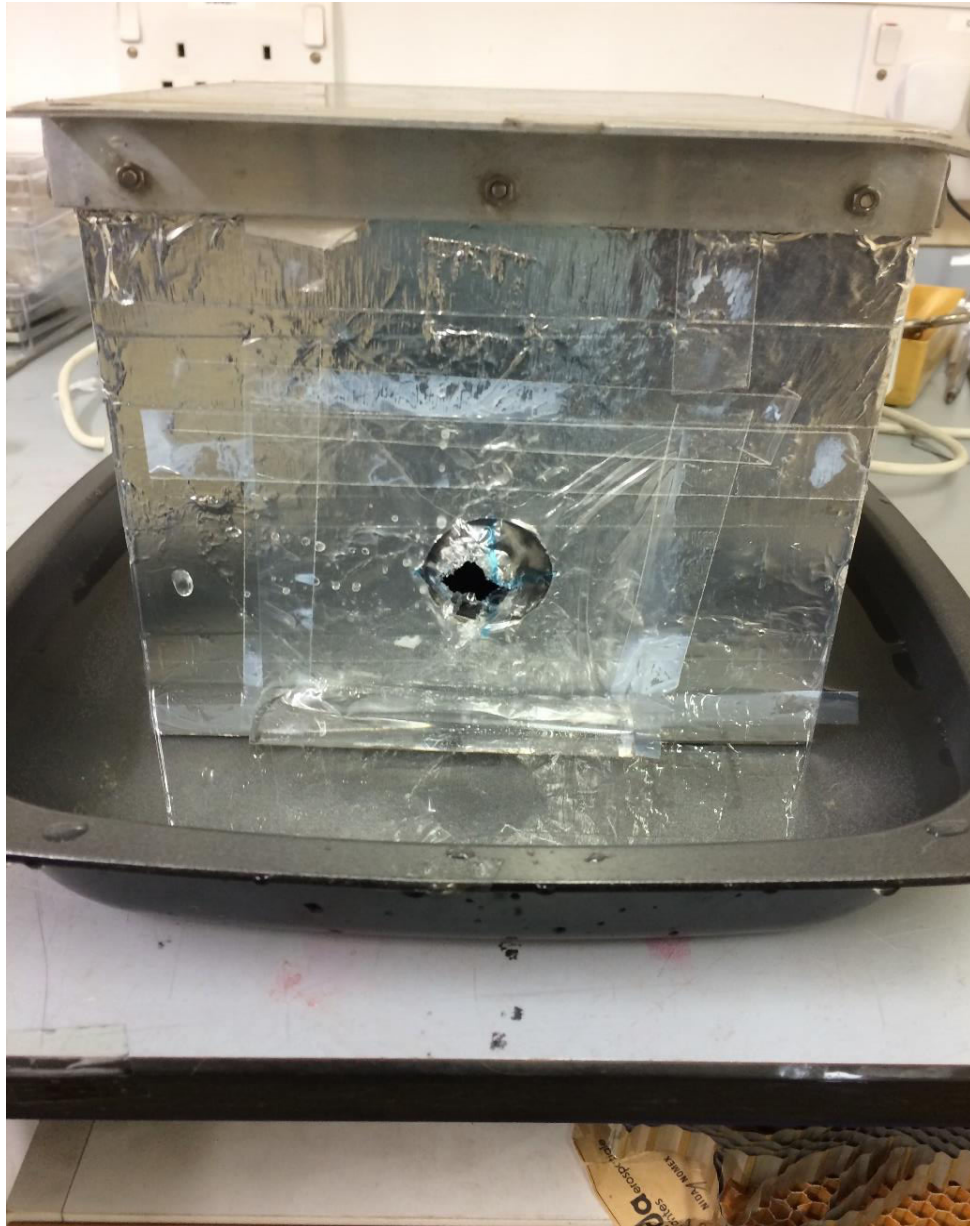
Figure 57: An image showing the front of the target box following impact of the counter-bored sabot with an inset lid at a velocity of 0.415 km s⁻¹. The sabot enters the target box via an aperture (pictured) which is covered by a thin plastic lining (consisting of a plastic bag). The plastic lining was punctured by entry of the sabot.

Figure 58: An image showing the front of the target box following impact of the counter-bored sabot with an inset lid at a velocity of 0.897 km s^{-1}. The sabot enters the target box via an aperture (pictured) which is covered by a thin plastic lining. The red liquid seen in the lower section of the image had previously filled the target box and as seen in the prior figure 48 was ejected out following the impact. The liquid was coloured red during this particular shot to make video recording of the impact easier to visualise.

4.3 Applying the Planar Impact Approximation to the liquid core sabot data.

For completeness we also calculated the peak shock pressure in the impacts by liquid core sabots again applying the PIA. In order to calculate the peak shock pressure experienced by the contents of the liquid core sabot, the special case equation (7) for similar projectile and target materials must be used. In this instance the target and projectile materials being liquid water.

The results of applying this can be seen in Table 13. It illustrates the calculated peak shock pressure experienced by the projectile according to the PIA. The ρ_0, C and S values for liquid water are given as 997 kg m^{-3}, 2393 m s^{-1} and 1.333 respectively [57]. Once again the sabot material (nylon) will be neglected.

Table 13: Peak Pressure calculated using the PIA.

Impact Velocity (km s^{-1})	PIA Peak Pressure (GPa)
0.415	0.5
0.897	1.3

4.4. Operationalising the liquid core sabot.

In this section we will take the new liquid core sabot design developed here and test its capacity to successfully transfer material other than simple glass tracer beads.

The material to be used in this case was the diatomaceous soil investigated in previously. This substrate has been shown to be recoverable at shock pressures on the order of 13 GPa following impact velocities of > 5 km s^{-1} and due to its particulate nature, it is easily dispersible in liquid. Figure 59 highlights what was recovered post impact at 2.04 km s^{-1}. What was noticeable upon

SEM examination was the reduced amount of debris when compared to the plastic bag capture method used in the frozen diatomaceous soil programme. There is a typical amount of paper fibres from the Whatman filter paper that the diatoms were extracted from, this could be improved in further programmes of study by altering the filtration process to a vacuum based system. SEM examination for these two shots, was conducted over the course of one day, No overnight map was run as utilised in the frozen diatom shots, but a manual scan to find fragments as confirmation of material transfer was carried out.
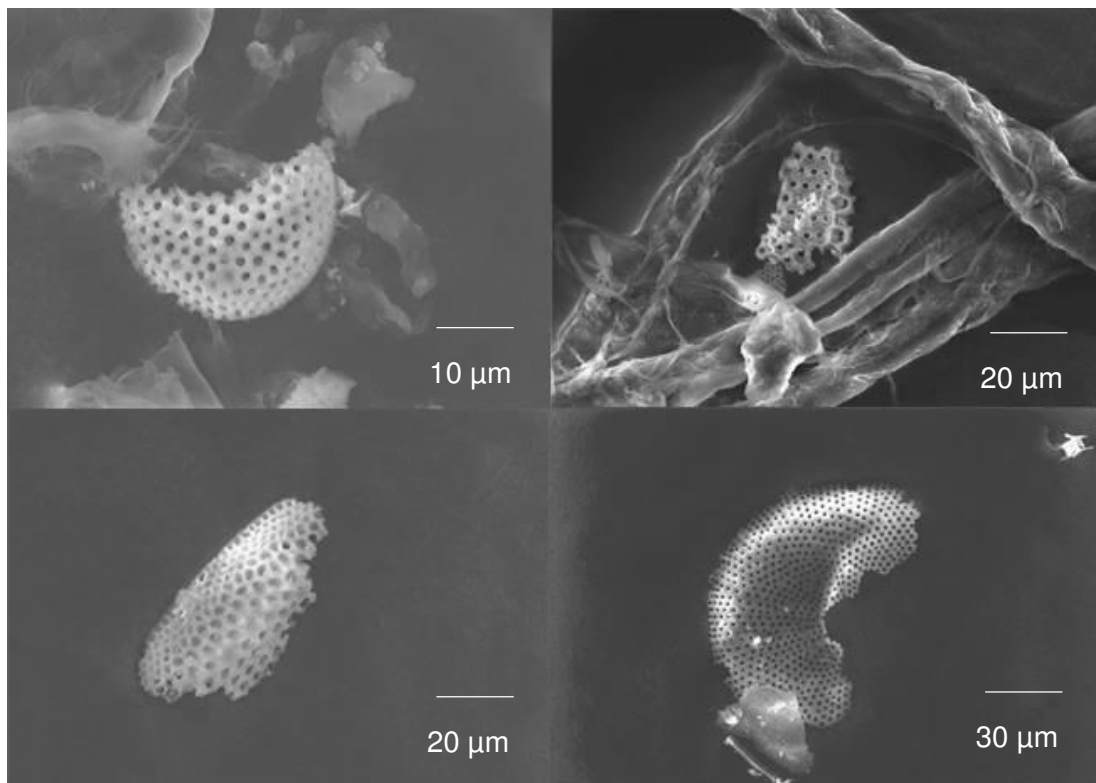
Figure 59: A montage of four images highlighting identifiable diatom fragments.

Figure 60 should be noted because, as before, we have found sillicoflagellate fossils surviving post-impact. This is interesting because they display a more ornamental structure, with projections that could shear off in impact events.
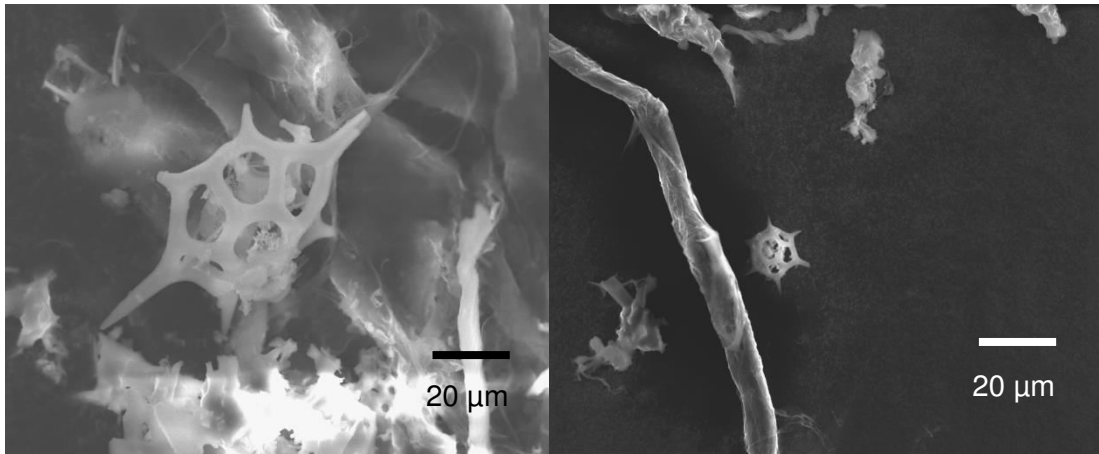
Figure 60: Identifiable sillicoflagellate fragments. These were recovered from filtered material recovered from the 2.04 km s^{-1}. They had been exposed to 3.74 GPa.

While the goal of this shot series and fragment search was to establish whether the sabot design is able to transfer actual experimental material, it should be noted that these shots were carried out on the order of ~ 2 km s^{-1} (2.04 and 2.17 km s^{-1}) and thus also acted to set a velocity benchmark for this sabot design. As seen in table 14 and figure 61 this design is capable of withstanding and transmitting material up to 3.77 GPa. It would thus be prudent to attain upper bounds for this design, with regards to shot velocity in the near future.

Table 14: Peak Pressure calculated using the PIA.

Impact Velocity (km s^{-1})	PIA Peak Pressure (GPa)
2.04	3.74
2.17	3.77

Figure 61: Intact sabot containing diatomaceous soil in suspension (right) before a shot. (Left) the new sabot design following the 2.17 km s^{-1}, the sabot has significantly deformed but was capable of transmitting its contents into the target.

The results in table 13 suggest that the glass beads start to show minor damage at around 0.5 GPa and more severe surface damage at 1.3 GPa. The glass beads were still mostly intact and spherical even in impacts at a magnitude of ~ 1 GPa.

The key result here is that the problem of liquid content evaporation when the sabot is under pressure has been solved. The design implementing a counter bored sabot and inset lid fixed to the sabot's interior with adhesive was successful on two counts. Primarily this design was able to withstand pressures to 50 mbar, this is a common pressure that sabots must endure within the gun and so its utility has been established here. It was also robust enough to endure shots with the light-gas gun, which provides us with confidence that despite the modifications to the standard single well sabots the structural integrity is not diminished either during flight or impact. This programme confirms that materials buffered in water could be introduced into the suite of substrates amenable to use within the light-gas gun at Kent.

We were also able to move this project from one that was strictly developmental into showing that it is an operational design. It is able to contain actual experimental samples in suspension and is capable of withstanding

shock pressures up to 3.77 GPa. This was achieved by exposing the sabot to an impact velocity of 2.17 km s^{-1}.

CHAPTER FIVE:

CONCLUSIONS.

5.1. Initial conclusions.

This chapter will provide conclusions that can be drawn from the observations arising from this project and subsequently outlined in the results section.

The purpose of the experimental design in project one was to investigate the viability of the impact shock phase of lithopanspermia, in the context of shock loading of microfossils. As such, the series of shots undertaken, are relevant to the transmission of microfossils (diatom frustules). It has been suggested in prior studies that terrene material may litter the lunar surface; some of this material being of biological origin [28] [58]. This project does not concern itself with the survival of living organisms but of the 'survival' of recoverable and recognisable fragments of microfossils.

The other topic of interest seen in project two, arose out of a desire to use a particular type of projectile (i.e. one that contained liquids). This would be of use when investigating the reactions to shock pressures of biological matter, when the matter itself is unsuitable for freezing into a sabot.

The initial conclusions that can be made from this study featured in project one, is that algal microfossils can withstand shock pressures up to 13.3 GPa; retaining morphological recognisability. Fragments were found at all velocities achieved (0.388 – 5.11 km s^{-1}) while the mean size, as well as the largest and second largest fragment decreased with respect to increasing impact velocity; and thus increasing shock pressures. It is important to remember that the lunar impact velocities are much lower than those of Mars and other larger solar

system bodies. As such, while survivability of fragments at lower velocities were recovered it is improbable that anything recoverable would be found at higher velocities. The idea of Armstrong [27] that Earth fossils might be recoverable from the lunar surface is supported with data collected in this experimental programme. The results have been published in the journal, Philosophical Transactions of The Royal Society A [56].

Also established (via project two) is a viable new sabot design that can hold a liquid core, suitable for high velocity impact experiments in the light-gas gun. This is important as it increases the diversity of substrates that can be investigated. This will permit the use of projectile materials that can be suspended in water, something previously not possible with the Kent gun.

5.2. Further possible research.

The shot programme investigating microfossil recoverability could be improved or elaborated upon by introducing a number of potential modifications:

One potential modification would allow for the ability to use a particular diatom species and therefore fossils that can be loaded in a particular size range. For instance *Thalassiosira weissflogii* has a length range between 10 – 20 µm. Diatom species can be sourced from the field or simply by a phytoplankton supplier. Isolation can be attained by chemical digestion (boiling in hydrogen peroxide); this will strip the organic material leaving the silicate fossils. Another advantage of this modification is the capacity to ensure the inclusion of intact diatoms into the sabot.

The shot programme described in the methods chapter outlined an experimental application of prior impact modelling; where terrene meteorites impact the lunar surface. While it would be impractical to attempt a shot programme that mapped to the mean Martian impact speeds; increasing the shot velocities and thus increasing the shock pressure experienced by the projectile could still be carried out. This would provide an opportunity to investigate the upper limit of recoverability of the microfossil fragments in the context of high shock pressures (>13.3 GPa has not been induced here).

Diatoms are not the only organisms that produce distinct microfossils; the protozoan radiolaria, synthesise silica skeletons that are arguably more complex and so the effects of shock experiments could be valuable with regards to fossil fragment survivability. Calcareous nanofossils, include the coccolithophores (another unicellular eukaryotic phytoplankton) such as the prevalent *Emiliana huxleyi*. These have the capacity to produce calcium carbonate plates (coccoliths) and are the main constituent of chalk. As such they are quite ubiquitous and the difference in make-up compared to the diatoms with their silicate skeletons could produce a different fragmentary profile when exposed to high shock pressures.

The target itself could be improved upon in further microfossil recovery experiments. The target used in the liquid core sabot shots reduced the amount of plastic bag debris. The bag in that instance was utilised as a seal to cover the aperture of the target box, preventing leaks. The target box was then filled with water and the impactor could be recovered therein, following the shot. This would allow for a more accurate reading of microfossil counts under the SEM. This is because with an increase in impact velocity there is a commensurate increase in plastic debris that may act to obscure any microfossil remnants. This is troubling because an increasing velocity also results in less identifiable fragments to be recovered and so an amelioration of the debris issue would allow for smaller fragments that may have been hidden in prior tests to be found.

The results of higher velocity impacts would also be of interest in the context of the liquid core sabot design. So far the design remains untested at impact velocities exceeding 3 km s^{-1}. Further research and development would be very important as typically velocities do surpass 3 km s^{-1}. A short topic of research that could be attempted (largely for completeness), would be to investigate further the pressure at which the liquid core sabots fail. We have moved this sabot from a developmental project into an operational design that can be added to the suite of sabot designs, appropriate for experiments in the light gas gun. We have established that at the typical 50 mbar that the gun is evacuated to, the counter-bored sabots are suitable. However how does this design fare at lower pressures?

Finally the impact velocities from both project one and two were analysed in order to derive the peak shock pressure for each shot. Only the Planar Impact Approximation (PIA) was used for this component of the study. One way to elaborate on the shock pressure values is to use the hydrocode AUTODYN. This has been applied to the microfossil impact velocity data by other members of the research group and the results of that analysis can be found in Burchell et al. (2014) [56]. The benefit of using AUTODYN includes an ability to feature multiple materials within the target and projectile. Not only this, but computer modelling has the capacity to identify areas of high and low pressure, providing upper and lower pressure bounds that a particular impact velocity induces.

5.3. Closing remarks.

For the first time it has been experimentally shown that fossils could indeed act as viable biomarkers on the lunar surface, by analysing the effect that high shocks have upon them. This adds weight to the suggestions of previous researchers that the Earth's 'attic' could indeed hold fossilised remnants of ancient life. However the sceptical adage of extraordinary claims requiring extraordinary evidence should be reflected upon when discussing the consequences of this project. The discovery and analysis of a potential terrestrial meteorite found on the lunar surface is a task that is now for space scientists. This process is no small task and would require a return to the lunar surface in the form of either robotic or manned missions. If such a rock was found and returned to Earth, its contents should be carefully examined. With an eye not just for mineral content and structural composition but also for relic biomarkers such as terrestrial microfossils. If dating of such a rock via isotopic ratios was also available then a capsule of Earth's past would have been found.

REFERENCES.

[1]   Arrhenius S. (1908) *Worlds in the Making: The Evolution of the Universe*. New York: Harper and Row.

[2]   Burchell M. J. (2004) *Panspermia Today*. International Journal of Astrobiology **3**: 73-80.

[3]   Gollihar, J., Levy, M., and Ellington, A. D. (2014) *Many Paths to the Origin of Life.* Science **343**: 259-260.

[4]   McKay, C. P. (2014) *Requirements and Limits for Life in the Context of Exoplanets.* PNAS **111**: 12628-12633.

[5]   Burchell, M. J., Galloway, J. A., Bunch, A. W. and Brandao, P. F. B. (2003) *Survivability of Bacteria Ejected From Icy Surfaces After Hypervelocity Impact*. Origins of Life and Evolution of the Biosphere **33**: 53-74.

[6]   Thompson (Lord Kelvin), W. (1871) *The British Association Meeting at Edinburgh*. Nature **4**: 261-278.

[7]   Dartnell, L. R., Hunter, S. H., Lovell, K. V., Coates, A. J. and Ward, J. M. (2010) *Low-Temperature Ionizing Radiation Resistance of Deinococcus radiodurans and Antarctic Dry Valley Bacteria*. Astrobiology **10**: 717-732.

[8]   Atri, D. and Melott, A. L. (2014) *Cosmic Rays and Terrestrial Life: A Brief Review*. Astroparticle Physics **53**: 186-190.

[9]   Nicholson, W. L., Schuerger, A. C. and Setlow P. (2005) *The Solar UV Environment and Bacterial Spore UV Resistance: Considerations for Earth-to-Mars Transport by Natural Processes and Human Spaceflight.* Mutation Research **571**: 249-264.

[10]   Mileikowsky, C., Cucinotta, F. A., Wilson, J. W., Gladman, B., Horneck, G., Lindegren, L., Melosh, H. J., Rickman, H., Valtonen, M., and Zheng, J. Q. (2000) *Risks Threatening Viable Transfer of Microbes Between Bodies in our Solar System.* Planetary and Space Science **48**: 1107-1115.

[11]   Melosh, H. J. (1993) *Blasting Rocks off Planets.* Nature **363**: 498-499.

[12]   Fairen, A. G. and Schulze-Makuch D. (2013) *The Overprotection of Mars*. Nature Geoscience **6:** 510-511.

[13]   Clark, B. C. (2001) *Planetary Interchange of Bioactive Material: Probability Factors and Implications.* Origins of Life and Evolution of the Biosphere   **31**: 185-197

[14]   Jerling, A., Burchell, M. J. and Tepfer, D. (2008) *Survival of Seeds in Hypervelocity Impacts*. International Journal of Astrobiology **7**: 217-222.

[15]   Burchell, M. J., Parnell, J., Bowden, S. A., and Crawford, I. A. (2010) *Hypervelocity Impact Experiments in the Laboratory Relating to Lunar Astrobiology*. Earth, Moon, and Planets **107**: 55-64.

[16]   Korotev, R. L. (2005) *Lunar Geochemistry as Told by Lunar Meteorites*. Chemie der Erde - Geochemistry **65**: 297-346.

[17]   Korotev, R. L., Joliff, B. L., Zeigler, R. A., Gillis, J. J., and Haskin, L. A.,
        (2003) *Feldspathic Lunar Meteorites and Their Implications for
        Compositional Remote Sensing of the Lunar Surface and the
        Composition of the Lunar Surface.* Geochimica et Cosmochimica Acta
        67: 4895-4923.

[18]   The Meteoritical Society. *Meteoritical Bulletin Database*, [Online].
        Available: http://www.lpi.usra.edu/meteor/metbull.php. [Accessed 28
        July 2014].

[19]   Basilevsky, A. T., Neukum, G., and Nyquist, L. (2010) *The Spatial and
        Temporal Distribution of Lunar Mare Basalts as Deduced From
        Analysis of Data for Lunar Meteorites.* Planetary and Space Science
        58: 1900-1905.

[20]   Rochette, P., Gattacceca, J., Ivanov, A. V., Nazarov, M. A. and
        Bezaeva, N. S. (2010) *Magnetic Samples of Lunar Materials:
        Meteorites, Luna and Apollo Returned Samples.* Earth and Planetary
        Science Letters **292**: 383-391.

[21]   Nagaoka, H., Karouji, Y., Arai, T., Ebihara, M., and Hasebe. N. (2013)
        *Geochemistry and Mineralogy of a Feldspathic Lunar Meteorite
        (Regolith Breccia), Northwest Africa 2200* Polar Science **7**: 241-259.

[22]   Hill, D. H., Boynton, W. V., and Haag R. A. (1991) *A Lunar Meteorite
        Found Outside the Antarctic.* Nature **352**: 614-617.

[23]   Werner, S. C., Ody, A., and Poulet, F. (2014) *The Source Crater of
        Martian Shergottite Meteorites.* Science **343**: 1343-1346.

[24]   McSween, H. Y. (1994) *What we Have Learned About Mars From SNC Meteorites*. Meteoritics **29**: 757-779.

[25]   Treiman, A. H., Gleason, J. D., and Bogard, D. D. (2000) *The SNC Meteorites are From Mars*. Planetary and Space Science **48**: 1213-1230.

[26]   Melosh, H. J. (1988) *The Rocky Road to Panspermia*. Nature **332**: 687-688.

[27]   Armstrong, J. C. (2010) *Distribution of Impact Locations and Velocities of Earth Meteorites on the Moon*. Earth, Moon, and Planets **107**:43-54.

[28]   Armstrong, J. C., Wells, L. E., and Gonzalez, G. (2002) *Rummaging Through Earth's Attic for Remains of Ancient Life*. Icarus **160**: 183-196.

[29]   Spudis, P. D. (1999) *The Case for Renewed Human Exploration of the Moon*. Earth, Moon, and Planets **87**: 159-171.

[30]   Crawford, I. A., Baldwin, E. C., Taylor, E. A., Bailey, J. A. and Tsembelis, K. (2008) *On the Survivability and Detectability of Terrestrial Meteorites on the Moon*. Astrobiology **8**: 242-252.

[31]   Reyes-Ruiz, M., Chavez, C. E., Aceves, C. E., Hernandez, M. S., Vazquez R., and Nunez, P. G. (2012) *Dynamics of Escaping Earth Ejecta and Their Collision Probabilities With Different Solar System Bodies*. Icarus **220**: 777-786.

[32]   Worth, R. J., Sigurdsson, S., and House, C. H. *Seeding Life on the Moons of the Outer Planets via Lithopanspermia*. Astrobiology, vol. 13, pp. 1155-1165, 2013.

[33]   Vickery, A. M., and Melosh, H. J. (1987) *The Large Crater Origin of SNC Meteorites*. Science **237**: 738-743.

[34]   de la Torre, R., Sancho, L. G., Horneck, G., de los Rios, A., Wierzchos, J., Olsson-Francis, K., Cockell, C. S., Rettberg, P., Berger, T., de Vera, J. P., Ott S., Frias, J. M., Melendi, P. G., Lucas, M. M., Reina, M., Pintado, A., and Demets, R. (2010) *Survival of Lichens and Bacteria Exposed to Outer Space Conditions - Results of the Lithopanspermia Experiments*. Icarus **208**: 735-748.

[35]   Olsson-Francis, K., and Cockell, C. S. (2010) *Experimental Methods for Studying Microbial Survival in Extra-Terrestrial Environments*. Journal of Microbial Methods **80**: 1-13.

[36]   de la Torre Noetzel, R., Sancho, L. G., Pintado, A., Rettberg, P., Rabbow, E., Panitz, C., Deutschmann, U., Reina, M., and Horneck, G. (2007) *BIOPAN Experiment LICHENS on the Foton M2 Mission Pre-Flight Verification Tests of the Rhizocarpon geographicum - Granite Ecosystem*. Advances in Space Research **40**: 1665-1671.

[37]   Brandstatter, F., Brack, A., Baglioni, P., Cockell, C. S., Demets, R., Edwards, H. G. M., Kurat, G., Osinski, G. R., Pillinger, J. M., Roten, C. A., and Sancisi-Frey, S. (2008) *Mineralogical Alteration of Artificial Meteorites During Atmospheric Entry. The STONE-5 Experiment*. Planetary and Space Science **56**: 976-984.

[38] Essary, B. D., and Marshall, P. A. (2009) *Assessment of FUN-1 Vital dye Staining: Yeast With a Block in the Vacuolar Sorting Pathway Have Impaired Ability to Form CIVS When Stained With FUN-1 Fluorescent dye*. Journal of Microbiological Methods **78**: 208-212.

[39] de Vera, J. P., Schulze-Makuch, D., Khan, A., Lorek, A., Koncz, A., Mohlmann, D., and Spohn, T. (2013) *Adaptation of an Antarctic Lichen to Martian Niche Conditions can Occur Within 34 days*. Planetary and Space Science **98**: 182-190.

[40] National Center for Biotechnology Information (NCBI): NCBI Taxonomy, [Online]. Available: http://www.gbif.org/species/106068915 [Accessed 04 December 2013].

[41] Stöffler, D., Horneck, G., Ott, S., Hornemann, U., Cockell, C. S., Moeller, R., Meyer, C., de Vera, J. P., Fritz, J., and Artemevia, N. A. (2007) *Experimental Evidence for the Potential Impact Ejection of Viable Microorganisms From Mars and Mars-like* planets. Icarus **186**: 585-588.

[42] Leighs, J. A., Hazell, P. J., and Appleby-Thomas, G. J. (2012) *The Effect of Shock Loading on the Survival of Plant Seeds*. Icarus **220**: 23-28.

[43] Pierazzo, E., and Chyba, C. F. (1999) *Amino Acid Survival in Large Cometary Impacts*. Meteoritics & Planetary Science **34**: 909-918.

[44] Burchell, M. J., Cole, M. J., McDonnell, J. A. M., and Zarnecki, J. C. (1999) *Hypervelocity Impact Studies Using the 2 MV Van de Graaff Accelerator and Two-Stage Light Gas Gun of the University of Kent at Canterbury*. Measurement Science and Technology **10**: 41-50.

[45] Mastrapa, R. M. E., Glanzberg, H., Head, J. N., Melosh, H. J., and Nicholson, W. L. (2001) *Survival of Bacteria Exposed to Extreme Acceleration: Implications for Panspermia*. Earth and Planetary Science Letters **189**: 1-8.

[46] Horneck, G., Stoffler, D., Eschweiler, U., and Hornemann, U. (2001) *Bacterial Spores Survive Simulated Meteorite Impact*. Icarus **149**: 285-290.

[47] de Vera, J. P., Horneck, G., Rettberg, P., and Ott, S. (2004) *The Potential of the Lichen Symbiosis to Cope With the Extreme Conditions of Outer Space II: Germination Capacity of Lichen Ascospores in Response to Simulated Space Conditions*. Advances in Space Research **33**: 236-43.

[48] Burchell, M. J., Mann, J., Bunch, A. W., Brandao. (2001) *Survivability of Bacteria in Hypervelocity Impacts*. Icarus **154**: 545-547.

[49] Price, M. C., Solscheid, C., Burchell, M. J., Josse, L., Adamek, N., and Cole, M. J. (2013) *Survival of Yeast Spores in Hypervelocity Impact Events up to Velocities of 7.4 km s^{-1}*. Icarus **222**: 263-272.

[50] Fajardo-Cavazos, P., Langenhorst, F., Melosh, H. J., and Nicholson, W. L. (2009) *Bacterial Spores in Granite Survive Hypervelocity Launch by Spallation: Implications for Lithopanspermia*. Astrobiology **9**: 647-657.

[51] Mock, T., Samanta, M. P., Iverson, V., Berthiaume, C., Robison, M., Holtermann, K., Durkin, C., BonDurant, S. S., Richmond, K., Rodesch, M., Kallas, T., and Huttlin, E. L. (2007) *Whole-Genome Expression Profiling of the Marine Diatom Thalassiosira pseudonana Identifies Genes Involved in Silicon Bioprocesses*. PNAS **105**: 1579-1584.

[52] Amato, A., Orsini, L., D'Alelio, D., and Montresor, M. (2005) *Life Cycle, Size Reduction Patterns and Ultrastructure of the Pennate Planktonic Diatom Pseudo-nitzschia delicatissima (Bacillariophyceae)*. Journal of Phycology **41**: 542-56.

[53] Bowler, C., Allen, A. E., Badger, J. H., Grimwood, J., Jabbari, K., Kuo A., Maheswari, U., Martens, C., and Maumus F. (2008) *The Phaeodactylum Genome Reveals the Evolutionary History of Diatom Genomes*. Nature **456**: 239-244.

[54] Sims, P. A., Mann, D. G., and Medlin, L. K. (2006) *Evolution of the Diatoms: Insights From Fossil, Biological and Molecular* Data. Phycologia **45**: 361-402.

[55] Melosh, H. J. (1996) *Impact Cratering: A Geologic Process*. Oxford University Press.

[56]   Burchell, M. J., McDermott, K. H., Price, M. C., and Yolland, L. J. (2014) *Survival of Fossils Under Extreme Shocks Induced by Hypervelocity Impacts*. Philosophical Transactions of the Royal Society: A. **372**. doi:10.1098/ rsta.2013.0190

[57]   Melosh, H. J. (2013) *Contact and Compression Stage of Impact Cratering in Impact Cratering Processes and Products*. Wiley-Blackwell.

[58]   Crawford, I. A., Anand, M., Cockell, C. S., Falcke, H., Green, D. A., Jaumann, R., and Wieczorek, M. A. (2012) *Back to the Moon: The Scientific Rationale for Resuming Lunar Surface Exploration*. Planetary and Space Science **74**: 3-14.